IMPLANTABLE NEURAL PROBES FOR ELECTRICAL RECORDING AND OPTICAL STIMULATION OF CELLULAR LEVEL NEURAL CIRCUITRY IN BEHAVING ANIMALS

by

Fan Wu

A Dissertation submitted in partial fulfillment
of the requirements for the degree of
Doctor of Philosophy
(Electrical Engineering)
in the University of Michigan
2015

Doctoral Committee:
Professor Euisik Yoon, Chair
Associate Professor Joshua Berke
Associate Professor Pei-Cheng Ku
Professor Emeritus Kensall D. Wise

ACKNOWLEDGEMENTS

It has been an extremely challenging and rewarding journey working towards my Ph.D. degree in Electrical Engineering at the University of Michigan. Just steps away from crossing the finish line, I want to give thanks to all who have been supportive for their advice and friendship that are essential for my accomplishments over the past five and half years.

First and foremost, it has been a great pleasure to work with my adviser, Professor Euisik Yoon. He reached out to me when I was still a senior Biomedical Engineering undergraduate student at the University of Wisconsin, and effectively persuaded me to continue my education in Electrical Engineering as a Ph.D. student. I was very honored to join his research group, as the next person in line to carry the torch in continuation of the effort to develop the prestigious “Michigan probe.” Over the years, Prof. Yoon has encouraged me to engage research with a proactive attitude and a creative mindset, always looking for new opportunities and never settling at a comfort zone. Together, we sought after and built several multidisciplinary collaborations with other neuroscience research groups to bring transformative innovations for the next generation neural probe technologies. Prof. Yoon has repeatedly emphasized the importance of communication skills. With his guidance and support, I presented my research achievement at four international conferences, and have earned the “Best Oral Presentation Award” at the 17th International Conference on Solid-State Sensors,

Actuators and Microsystems in Barcelona, Spain.

I would like to appreciate the advisory from all other committee members. Professor Joshua Berke has been a great teacher of neuroscience. He has also helped me understand some of the practical requirements of neural probe engineering from a neuroscientist's perspective. Professor Pei-Cheng Ku has given me the fundamental lessons in the principle of semiconductor light emitting devices, which are the building blocks for the heart of this thesis as will be presented in Chapter 4. Lastly but not the least, professor Ken Wise, who is the pioneer of "Michigan probes", has always been a role model and has generously shared decades worth of experience in this field with me to push the boundary limit.

The works presented in this thesis could not have been possible without the synergistic collaborations with several research groups outside of the University of Michigan. Professor Gyorgy Buzsaki and Dr. Eran Stark from New York University have contributed significantly from the design stage of the optogenetic probes to the validation experiments in animal models. I sincerely wish Dr. Stark to be successful in his upcoming faculty career. Professor David Kaplan and his student Dr. Lee Tien from Tufts University were the experts in silk fibroin, which was incorporated into the fabrication process for the first time to facilitate the insertion of flexible, miniaturized polymer probes as will be described in Chapter 2. Professor Colin Humphreys and Dr. Dandan Zhu from Cambridge University have given invaluable advice for LED fabrication and characterization techniques.

During the early stages of my study, I was blessed with the guidance from many mentors, from whom I have inherited many useful fabrication techniques and design

strategies. Dr. Il-Joo Cho and Dr. Maesoon Im were my mentors in the cleanroom. I still vividly remember every lesson they have taught me when I was a novice cleanroom user. In recent years, I have given my efforts to pass on the knowledge to junior students. Many other experts including Dr. Sister Mary Elizabeth Merriam, Dr. Onnop Srivannavit, Ning Gulari, Dr. Razi Haque, Dr. John Seymour, Dr. Fujun Chen, Daniel Egert, and the Lurie Nanofabrication Facility staffs have also been extremely resourceful.

I would also like to thank all of the Yoon group members, my friends, and my family for their continuous support not only during times of celebration but also through hardship.

Lastly, I would like to acknowledge National Science Foundation for its generous support through the Graduate Research Fellowships Program.

TABLE OF CONTENTS

LIST OF FIGURES

LIST OF TABLES

ABSTRACT

IMPLANTABLE NEURAL PROBES FOR ELECTRICAL RECORDING AND OPTICAL STIMULATION OF CELLULAR LEVEL NEURAL CIRCUITRY IN BEHAVING ANIMALS

by Fan Wu

Chair: Euisik Yoon

In order to advance the understanding of brain function and behavior, it is critical to monitor how neural circuits work together and perform computational processing. For the past few decades, a wide variety of neural probes have been developed to study the electrophysiology of the brain. This work is focused on two important objectives to improve the brain-computer interface: 1) to enhance the reliability of recording electrodes by optimizing the shank structure in terms of geometry and material; 2) to incorporate optical stimulation capability in addition to electrical recording for applications involving optogenetics, which is an emerging neuroscience technology to allow optical control of cellular activities (Nature Method of the year, 2010).

For the first objective, a flexible 64-channel parylene probe was designed with unique geometries for reduced tissue reactions. In order to provide the mechanical stiffness necessary to penetrate the brain, the miniaturized, flexible probes were coated with a lithographically patterned silk fibroin, which served as a biodegradable insertion shuttle. Because the penetration strength is independent from the properties of the probe

itself, the material and geometry of the probe structure can be optimally designed without constraints. These probes were successfully implanted into the layer-V of motor cortex in 6 rats and recorded neural activities *in vivo* for 6 weeks.

For the second objective, two different methods have been investigated for optical stimulation. One is to integrate optical waveguides and the other is to integrate μLEDs on the probe shanks. Compared to other existing methods up to date, this work can only offer high spatial-temporal resolution to record and stimulate from even subcellular neural structures by monolithic integration of all optical and electrical components on the probe shanks using advanced MEMS fabrication techniques. The animal experiments were conducted at the Gyorgy Buzsaki lab in New York University to study the densely populated CA1 pyramidal layer of rodent hippocampus in both anesthetized and chronic behaving animals. The animals used were both wild type (no photo-sensitive ion channels) and ChR2 expressed (sensitive to blue light) rodents. In the wild type animals, despite optimized recording of spontaneous neural activities, the cells never responded to illumination. In contrast, for the ChR2 expressed animals, light activation of neural activities was extremely robust and local, which phase-locked to the light waveform whenever the cell was close to the light source. In particular, the probes integrated with μLEDs were capable of driving different neural circuit behaviors using two adjacent μLEDs separated only by a 60-μm-pitch. The minimum activation power to induce observable spikes during live recording was as low as 36nW, corresponding to 0.24mW/mm^2 of light intensity. With 3 μLEDs integrated at the tip of each of the 4 probe shanks, this novel optogenetic probe can provide more than 480 million (12!)

different spiking sequences at the sub-cellular resolution, which is ideal to manipulate high density neural network with versatility and precision.

CHAPTER 1

INTRODUCTION

1.1. Understanding the brain functions

The lack of a systematic theory about neural activity is complicated by the scale of the human brain, with an estimated 85 billion neurons, 100 trillion synapses, and 100 types of chemical neurotransmitters[1]. Recent publication shows that the causal network representing the large-scale connectivity of the expanding universe is strikingly similar to that of a human brain[2]. **Figure 1.1** is a conceptual illustration of a very small portion of the vast neural network. Each neuron is a highly specialized cell that communicates with other cells by sending electrical signals through its axons, causing neurotransmitters to be released at the synaptic junctions, which are then received by the dendrites of the receiving neurons. The origin and processing of these neural signals are extremely complex, encoding every action and emotion[3]. Understanding what makes any one neuron fire or not is a central question in neuroscience, and so the ideal sensing tool must span from the single neuron to its network of connections in order to learn how that particular neural circuit assimilates information[4], [5]. Various technologies have been developed to understand brain function by monitoring the signal propagation through MRI[6], chemical sensing[7], optical imaging[8], [9] and electrical recording[10]–[12].

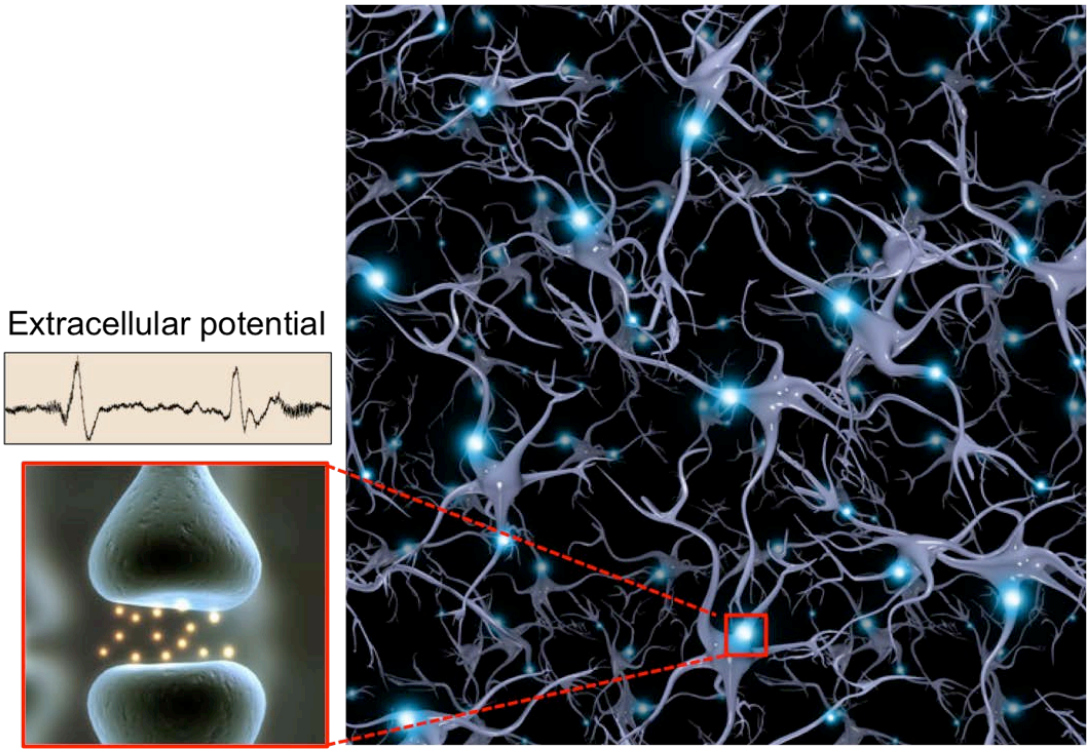

Figure 1.1: Inside look of the human brain showing massive network of interconnecting neurons through synaptic junctions (http://www.shutterstock.com/gallery-11418p1.html).

1.2. Optogenetics

In addition to recording neural activities passively, it is also useful to stimulate a particular neural circuit while monitoring the cellular level response and its correlation to animal behavior. Electrical stimulation of the nervous system can be dated to the year 1780, when Luigi Galvani observed twitching of the frog's leg muscles by passing electrical current through the attached metal electrodes (Wikipedia Commons). For the past few decades, electrical stimulation of the brain has brought tremendous insight on its functions[13], [14].

Because neural circuits are made of interacting cells of diverse types, selective activation/silencing of single neurons of specific types is required to identify the computational mechanisms of underlying functions and perturb the local circuits of a cortical system in a controlled manner[15]. For example, by activating (depolarizing) specific neurons within a region, it is possible to assess the processes that contribute to a specific behavior. Similarly, silencing (hyperpolarizing) specific neurons within a region can provide information about their roles in both network functions and behavior. This goal cannot be achieved effectively by electrical stimulation since it indiscriminately stimulates neuronal processes, including somata, dendrites and axons in a complex manner[16].

Advances in optogenetics provide a new approach to neural circuit analysis[17]. Optogenetics can introduce photo-sensitive proteins called opsins into specific cell types and achieve optical control of defined action potential patterns in specific targeted neuronal populations (**Figure 1.2**)[18]. Neurons that express these opsins can be selectively stimulated by visible light at an appropriate wavelength, and cell-type specificity can be achieved with well-controlled spatial and temporal resolution (order of milliseconds)[19]. For example, channelrhodopsin-2 (ChR2), when expressed in neurons, reacts rapidly to blue light (~473nm) with large depolarizing photocurrents to induce light-driven action potentials[19]–[22]. Halorhodopsins[23], [24] and archaerhodopsin[25], [26], when illuminated with yellow light (~590nm), mediate hyperpolarization, enabling the silencing of neural activity[25], [27], [28]. Multiple opsins can be expressed in the same cell so that it can be either depolarized or hyperpolarized by the corresponding wavelengths[24]. Likewise, different opsins can be

expressed in intermingled neuronal populations, enabling independent temporal control of those populations[29]. This specific targeting allows sophisticated manipulations of neural activity, testing spike timing during specific neural computations and behaviors at the resolution of individual subcircuits within the brain.

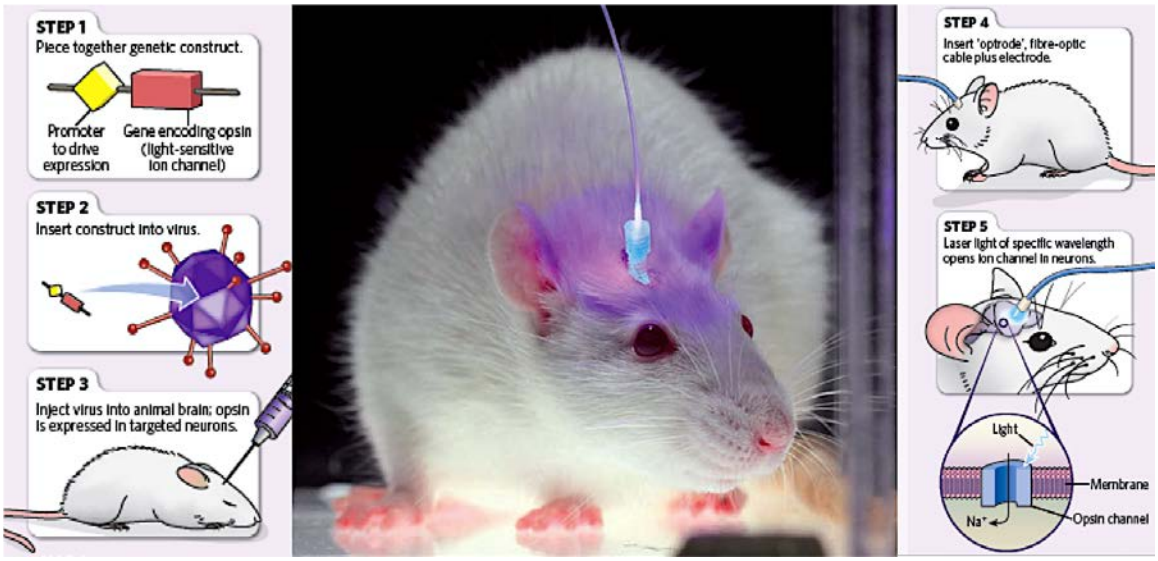

Figure 1.2: Optogenetics: genetically modifying targeted cell types for optical depolarization or hyperpolarization of the cell membrane[18].

For example, a recent study applied optogenetics to test different hypothesis underlying the ripple generation mechanisms in the hippocampus[30]. These fast oscillatory ripples (90-180Hz) are key physiological events in the hippocampus for memory consolidation[31]. Previously, competing models shown in **Figure 1.3**(a-c) have been proposed to explain the formation and timing of the oscillatory event[32]–[35]. In this study, by using different promoters, ChR2 was expressed specifically in either pyramidal cells (PYR) or interneurons (INT) or both. Blue light was delivered to the CA1 region of the hippocampus via optical fibers to stimulate the ChR2 expressed cells, and the induced effects mimicked the naturally occurring ripples and spikes.

Because of the cell-type specific optical stimulation, distinct roles of PYR (excitatory cells) and INT (inhibitory cells) were identified, which could not have been possible with electrical stimulation methods. The results indicated a new possible model as shown in **Figure 1.3**(d), where a complex PYR-INT-INT feedback network was shown to generate the ripple.

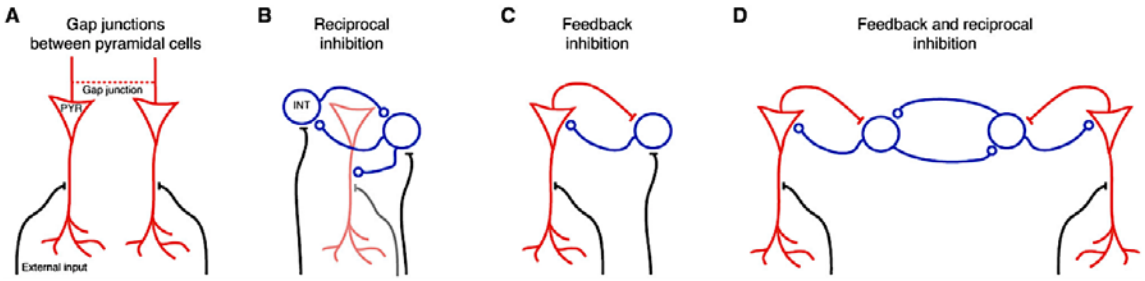

Figure 1.3: Proposed mechanisms for the generation of CA1 ripples.

1.3. Neural interfacing methods

Brain activities can be directly recorded using electrodes, by methods categorized according to the recording locations. In general, there is a tradeoff between signal fidelity and invasiveness of the recording method. For example, Electroencephalogram (EEG) is the noninvasive recording method using electrodes outside of the scalp[36]. However, each electrode can only record a spatiotemporally smoothed version of the local field potential (LFP), integrated over an area of around 10 cm^2. Individual neuronal activity cannot be discerned due to the large parasitic capacitance and resistance between the cell and the electrode, so that high frequency signals are severely distorted and attenuated[37]. In contrast, invasive electrodes are implanted underneath the brain surface to record directly from individual cells. **Figure**

1.4 shows the capability to map individual cells and identify their functions by recording the extracellular potentials from an array of electrodes implanted inside a deep brain structure[5]. While it is also possible to record intracellular potentials using patch clamps with even higher signal fidelity than extracellular recording[38], this technology is not scalable to record from a large-scale neural network as shown in **Figure 1.4**. The work described in this thesis will be focused only on the development of implantable technologies for extracellular recording of multiple, single-unit activities for advanced neuroscience applications to understand neural circuit function and behavior.

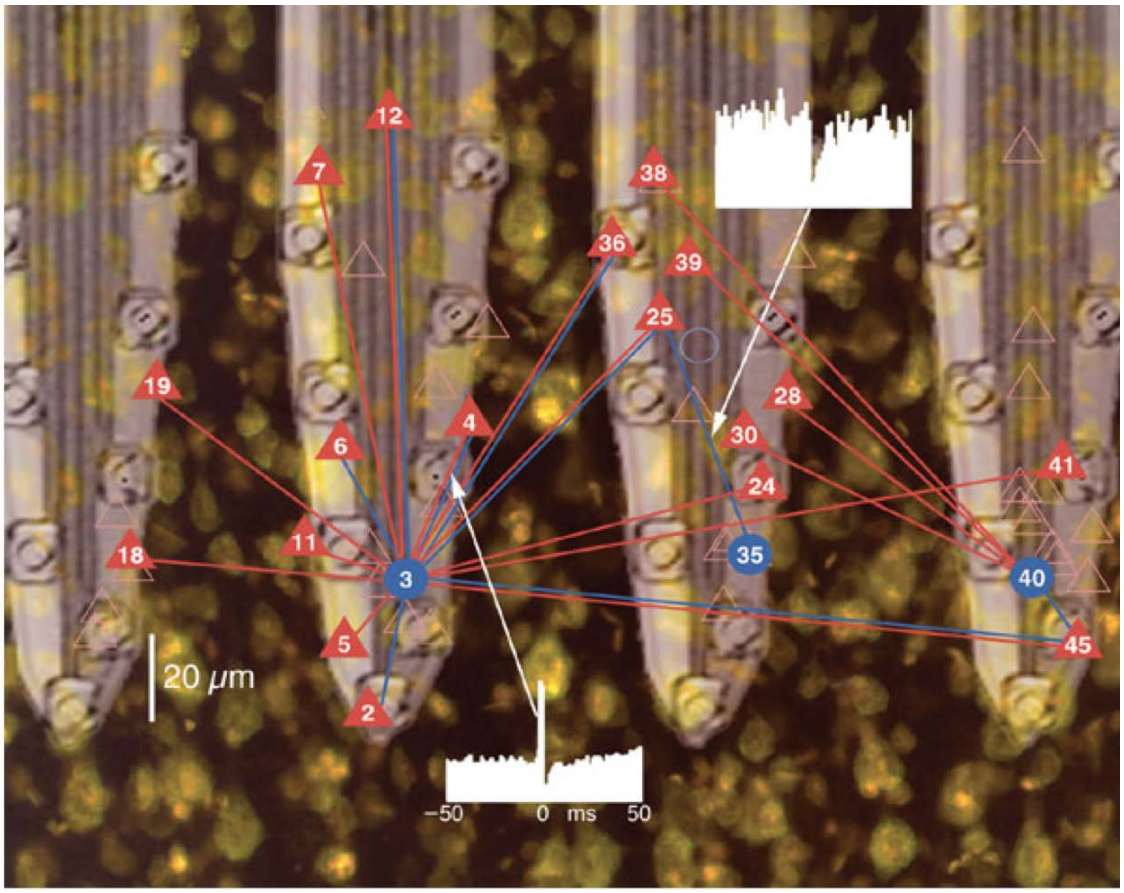

Figure 1.4: Mapping neuronal functions using implantable neural probes: the positions of pyramidal cells (PYR, red triangle) and interneurons (INT, blue circle) are calculated by triangulation of the recorded spikes from the electrodes. Red lines indicate excitatory outputs from PYR and blue lines indicate inhibitory outputs from INT[5].

1.4. Development of implantable neural probes

The earliest implantable electrode is a simple microwire developed more than 60 years ago to record from single neurons[39]. Since then, the microwire technology has evolved into tetrodes[40], [41] and polytrodes[42] configurations, which can be used to pinpoint locations of a neuron by measuring the relative signal amplitudes picked up by a group of electrodes. It was estimated that within 50μm of a tetrode, more than 100 neurons can be identified and separated after signal processing; and that within 140μm of a tetrode, more than 1,000 neurons can be detected (not yet separable) (**Figure 1.5**). These devices are readily available at low cost. However, the density of the electrodes is limited by the pitch between each tetrode, which cannot be accurately defined using manual assembly.

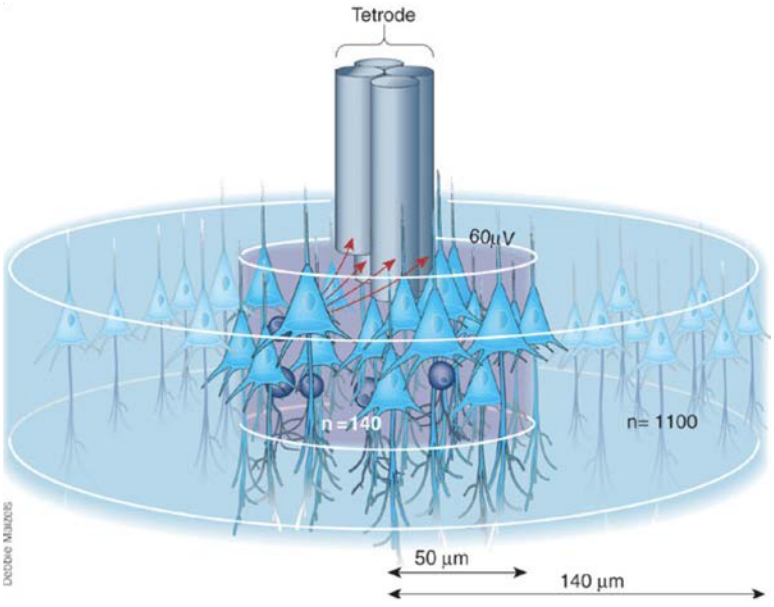

Figure 1.5: Schematic of a tetrode showing its capability to record from multiple neurons within its vicinity[5].

Advanced microelectromechanical systems (MEMS) technologies enable micron/sub-micron scale features to be accurately defined using photolithography techniques. **Figure 1.6** shows the micro-electrode array developed at the University of Utah[43]. By deep etching through silicon wafers, a matrix of “needles” is formed. The shank length is determined by the starting wafer thickness. A layer of insulation material covers the shanks, except at the tips, where metal is deposited to form the electrodes. Low power integrated circuits have been designed to interface with the Utah array for wireless data transfer[44]. Complete recording systems using the Utah array architecture have been commercialized by Blackrock Microsystems and have recently been approved by FDA for human applications[45].

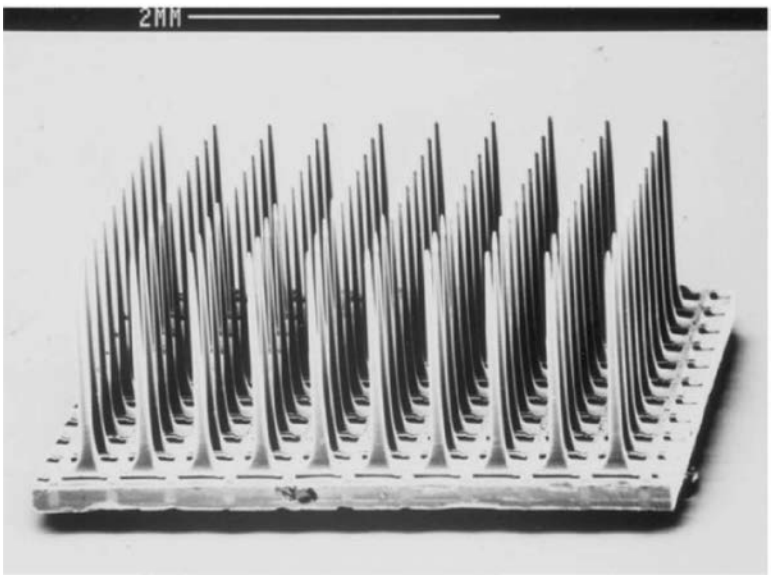

Figure 1.6: Photograph of a Utah electrode array[43].

Prior to the Utah array, Kensall Wise first pioneered the adaptation of microfabrication and micro-machining techniques to develop microprobes at Stanford University[46]. Later, the technology was being continuously developed at the

University of Michigan by Wise and his group, and has since then acquired the fame for its new name as the "Michigan Probe"[47]–[50]. In contrast to the Utah array, the Michigan probe is fabricated with its components (electrodes, interconnects) integrated on a planar substrate, followed by the bulk micromachining processes to shape the substrate into needle-shaped shanks (**Figure 1.7**). Typically, an array of stimulating/recording electrodes can be lithographically defined at the probe tip, and the interconnecting leads carry signals from/to the ribbon cable at the backend. The Michigan planar architecture offers several advantages over the Utah architecture. Firstly, any number of electrodes can be defined on a probe shank using lithography, whereas the Utah array can only carry one electrode per shank. Secondly, the probe shank length is not limited by the wafer thickness as it is in the Utah process, so that it can be easily tailored to target even the deepest regions in the brain (typically a few millimeters).

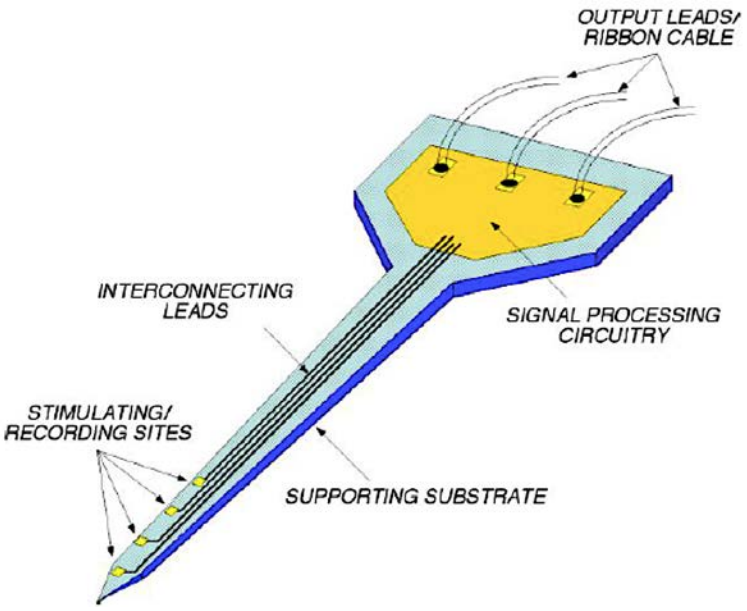

Figure 1.7: Schematic of a Michigan probe[48].

Because of the tremendous scalability and versatility of the planar probe processes, it has been the central platform for the development of high-density probes to monitor large number of neurons. Statistically, the number of integrated electrodes have been doubling every 7 years, mimicking the Moore's law; yet, advanced neuroscience studies demand more[51]. The challenges in scaling up the number of electrodes are several folds. Firstly, as the number of electrodes increases, the shank width should be kept at a minimum to avoid excessive insertion damage. Secondly, IC integration for multiplexing the large number of channels is necessary to avoid oversized assembly and tethering problems. Thirdly, to expand the recording coverage from the limitation of the planar probe structure, it is desirable to stack multiple 2-D probes into a 3-D array. **Figure 1.8**(a) shows a technique to integrate 64 electrodes in a high density manner on a 60-μm-wide probe shank by e-beam patterning of interconnect traces with 290nm width and spacing[52]. **Figure 1.8**(b) shows a monolithically integrated IC on probe shank to reduce the number of interconnection lines and external cables[53]. **Figure 1.8**(c) shows the most recent Michigan probe design prior to this thesis work that demonstrated a 128-channel, 3-D stacked array from multiple 2-D probes[54].

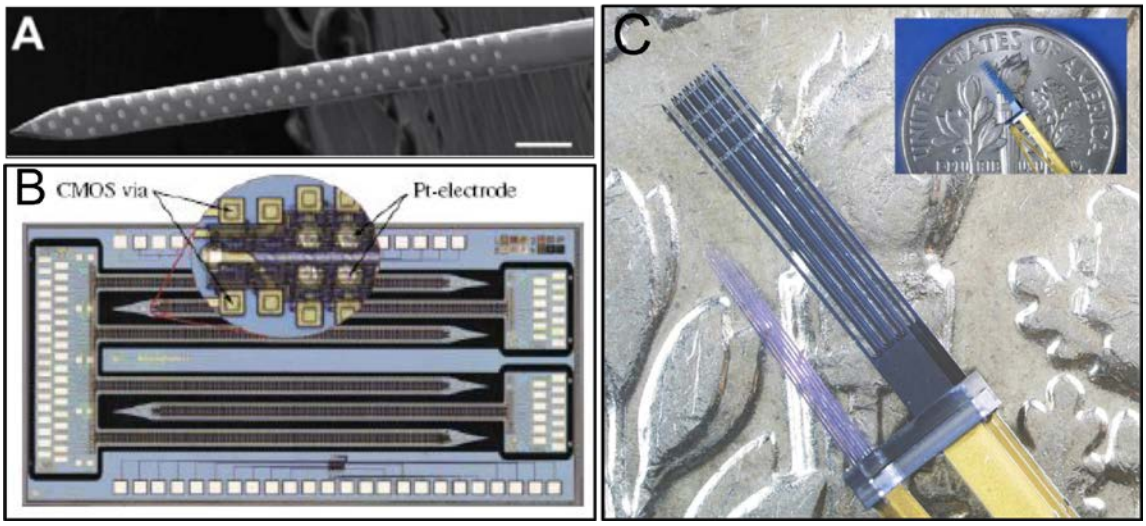

Figure 1.8: Recent process towards scaling the number of recording sites: (a) 64-channel probe using e-beam patterning[52]; (b) monolithically integrated circuits on probe shank[53]; (c) 3-D stacking of planar probes[54].

Another major motivation for the development of implantable neural probes is to prolong the lifetime of the electrodes. Foreign body reactions are inevitable and the neural recording quality typically degrades over time[55]. Creating lattice structures within the probe shank as shown in **Figure 1.9**(a) helps to reduce surface area to minimize protein adsorption, which can lead to downstream immunoreactions[56]. The comparison between a solid shank and a lattice shank having the same overall dimensions show significantly less adverse reaction near the lattice shank (Ph.D. dissertations by Gayatri and Merriam; **Figure 1.9**(b)). Another recent work by Seymour showed the importance of size reduction of the probe shanks and quantified the tissue reaction intensity as a function of the distance from the probe shank (**Figure 1.9**(c))[57]. The results suggested ideal placements of the recording electrodes relative to the probe shanks in order to minimize the local tissue reactions (**Figure 1.9**(d)).

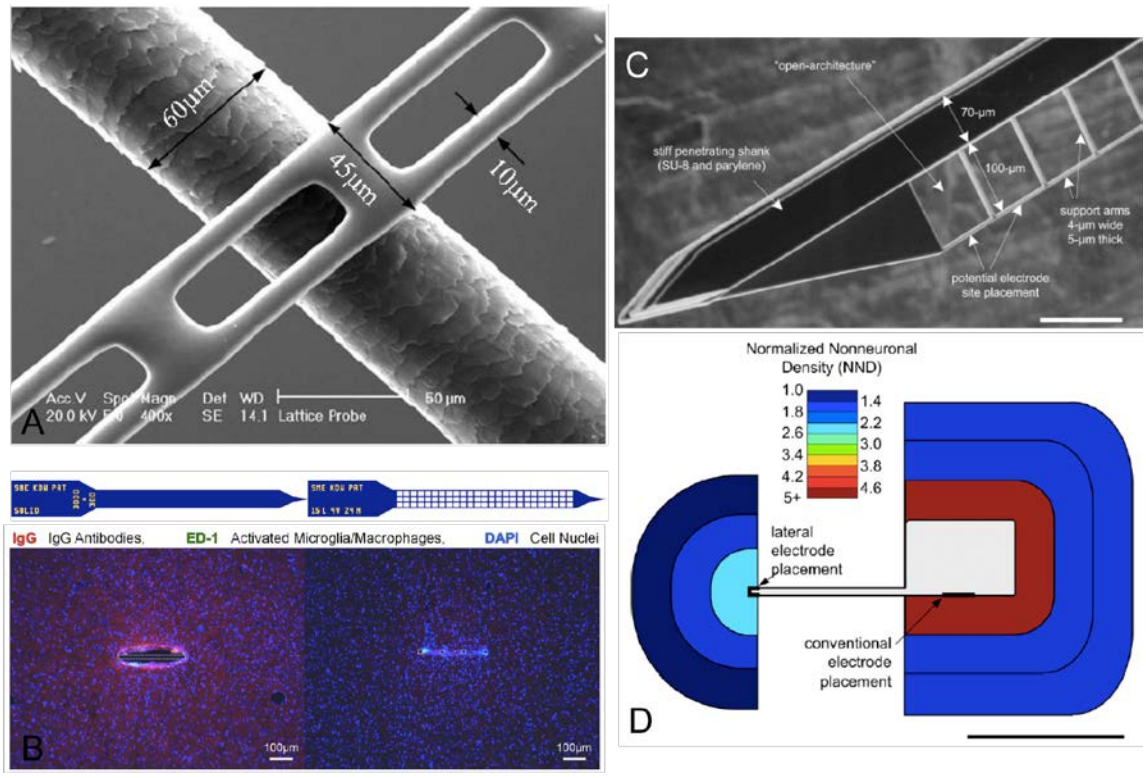

Figure 1.9: Recent developments in Michigan to reduce tissue reactions near the recording electrodes for chronic applications: Ph.D. dissertations from (a) Gayatri[58], (b) Merriam[59] and (c, d) Seymour[60].

The work described in this thesis continues the Michigan probe lineage with two primary objectives: 1) to prolong the recording lifetime of passive recording probes following strategies devised from previous contributions; 2) to open up a completely new direction for future Michigan probes by incorporating optical stimulation capability onto the existing platform, in order to fulfill the growing demand from the optogenetic community. For the second objective, two different approaches have been investigated, monolithically integrating either optical waveguides or µLEDs on the probe shank for cellular level manipulation of the neural circuitry.

CHAPTER 2

SILK-COATED POLYMER PROBES FOR CHRONIC RECORDING

2.1. Introduction

Implantable neural probes can monitor the activity of individual neurons with unmatched spatial and temporal resolution[61]. These devices provide the technological backbone to support the most advanced neuroscience research towards functional mapping of the neural circuitry and hold promises for clinical treatment of various neurological diseases in human[62]. Although many different designs have been realized[42], [48], [63]–[65], recording quality typically degrades over time due to complex foreign body reactions associated with breaching the blood-brain barrier, glial scar formation, neuronal degradation, etc., that can ultimately degrade the electrode interface with healthy neurons[66]–[68]. This bottleneck severely limits the application of neural probes from chronic animal experiments and reliable clinical human use.

Many previous studies have made progress towards understanding the foreign body reactions and have developed several strategies to minimize them. It has been shown that flexible probes helped to reduce tissue damage caused by the relative micro-motion between brain and implanted devices[69], [70]. Other studies have demonstrated that the local tissue reaction intensities are proportional to the implanted device size, showing significantly reduced astrocyte and microglia density near device structures

with sub-cellular dimensions[57], [71]. However, designing probes to accommodate these ideal conditions presents significant challenges. For example, it has been impractical to scale down probe size to the micro-fabrication technology limit. Even for silicon-based designs, there are minimum dimensions required to provide enough mechanical stiffness for proper insertion into the brain tissue without buckling against pia[72]. To design probes with flexible polymer materials having Young's Modulus two orders of magnitude lower than that of silicon is even more challenging due to the lack of stiffness. Several approaches have been made towards supporting the insertion procedure of flexible probes[73]–[75]. In a recent innovation, the smallest implantable probe realized by carbon fibre also showed significant reduction in chronic tissue reaction[71]. Yet these approaches often come with the cost of reducing the number of recording channels, which would limit their applications from more advanced neurophysiology. In this work, the aim was to design an implantable probe that is both flexible and minimal in size without compromising its scalability towards large number of recording electrodes in dense arrays for chronic applications.

2.2. Design

This probe has been designed for chronic behavioural neurophysiology to target layer-V of the rat motor cortex. The two outstanding criteria were to have a large number of recording electrodes and to have prolonged recording lifetime, which have previously proved challenging because of the intrinsic tradeoff between device size and the intensity of chronic tissue reaction[57]. In this work, 64 channels were integrated

into the probe, which must be designed with strategies to minimize tissue reactions near the electrodes.

The probe substrate was designed with parylene because of its biocompatibility, and flexibility (E = 2.8 GPa) for reduced tissue damage induced from micro-motion. The layout of the 64-channel probe is shown in **Figure 2.1**. It has eight shanks, each carrying 8 electrodes, which are extended 2 mm in depth in order to reach the layer-V motor cortex (**Figure 2.1**(a)). The total lateral recording span is 1.75 mm, accommodating a 250 μm pitch between each shank to prevent unnecessary adverse interactions between adjacent shanks. Each probe shank has a vertical recording span of 320 μm while adjacent shanks have a 200 μm vertical offset in order to maximize the recording coverage of the layer-V motor cortex (**Figure 2.1**(b)). The electrodes are grouped in a tetrode configuration with each electrode separated by a vertical pitch of 40 μm.

Because the number of shanks and the recording electrodes have been scaled drastically from a preliminary work[76] by an order of magnitude, each probe dimension must be minimized without sacrificing the fabrication yield. The parylene substrate is 8-μm-thick and has the bare minimum area to completely insulate all metal interconnection traces. This aggressive design allows a probe shank carrying 8 recording channels to have only 36 μm in width. A probe tip structure has a fork shape as shown in **Figure 2.1**(b), which may not resemble conventional silicon probe tip geometries. Therefore, this probe cannot penetrate the pia mater by itself and requires a mechanical

supporting structure for the duration of the implantation surgery.

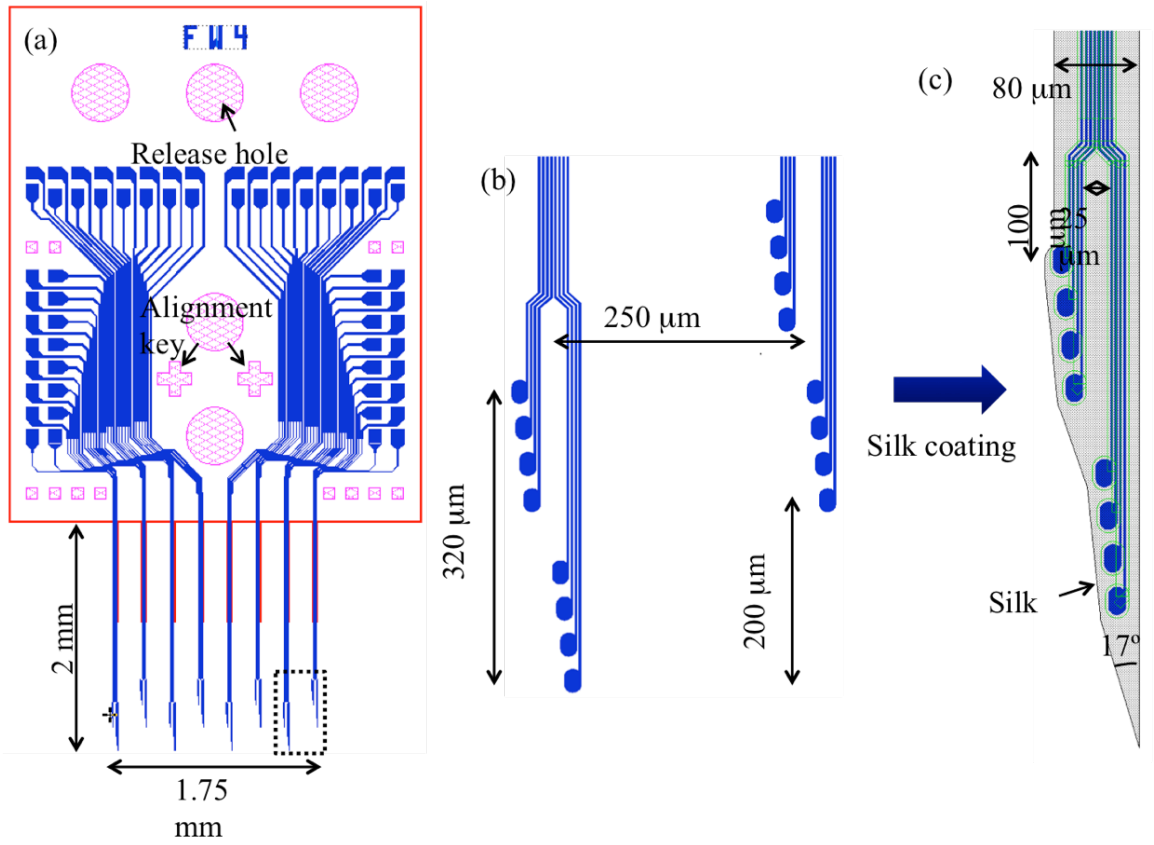

Figure 2.1: The schematics of a specific probe design: (a) overall probe layout showing 8 shanks with a backend containing bonding pads and holes within the parylene substrate for accelerating release process of the probes during fabrication and alignment during bonding process; (b) enlarged view of two adjacent probe shanks (metal layer shown only); (c) enlarged view of the probe tip with a biodegradable silk coating outlining the parylene probe to provide mechanical stiffness for insertion.

The parylene probe design can take any shape and flexibility because the mechanical stiffness required for insertion was predominantly controlled by the properties of a biodegradable coating of silk fibroin. This unique silk protein was selected among many other biodegradable materials because of its biocompatibility, process compatibility, high Young's modulus (E = 4-6 GPa) and controllable degradation time *in vivo*[77]–[79]. In a concurrent report, silk fibroin has been shown to

reduce gliosis with intrinsic biocompatibility and the potential to serve as a drug delivery vessel[80]. **Figure 2.1**(c) shows the schematic of a sharp probe tip shaped by a silk pattern that would support the insertion of the flexible parylene probe in any shape. Because the degradation rate of silk can be tailored, the coating was designed to remain mechanically stiff for the duration of the implantation procedure and will dissolve immediately after the targeted insertion depth has been reached. Once the silk dissolves, it leaves behind the flexible probe which has a unique structure specifically designed to favor minimized tissue reactions near the electrodes. In the specific design illustrated in **Figure 2.1**, the parylene probe has a fork-like tip to further reduce the parylene shank width by half. The topmost electrode was designed to have a 100-μm-long separation distance from the main probe shank. These design strategies are expected to reduce the chance of glial scar formation near the electrodes, knowing that the intensity of tissue reaction is proportional to size.

2.3. Probe fabrication

The fabrication process of the parylene probe is illustrated in **Figure 2.2**. A Cr/Au/Cr sacrificial layer was first deposited on a silicon wafer. The composite sacrificial layer has been shown to have a faster etching time than a single Cr layer in Cr etchant[81] in order to minimize the probe's soaking time in the acidic etchant. To form the bottom insulation, a 4-μm-thick parylene was deposited onto the sacrificial layer. The recording electrodes and the interconnection lines were formed by thermal evaporation of Ti/Au (20 nm/150 nm) layers followed by lift-off in acetone. The adhesion between parylene and Ti was enhanced by an O_2 plasma treatment at 100 W

for 30 seconds prior to the evaporation step. After patterning the metals, a 4 μm-thick parylene layer was deposited again as the top insulation layer. Next, the field parylene was dry etched by O_2 plasma to define the probe shape. In order to etch away the 8 μm-thick parylene without significant lateral etch, it was necessary to use a low stress, sputtered Cr layer (34 nm) instead of a thick photoresist as an etch mask. The Cr layer was patterned by a quick dip in Cr etchant with the patterned photoresist as a mask. After etching the field parylene, the Cr masking layer was patterned for the second time and was used to mask against a 4-μm-deep dry etch of parylene to expose the recording sites. Finally, the photoresist was stripped in acetone and the probes were released in Cr etchant, which etched away both the sacrificial layer and the Cr masking layer. The through-holes at the probe backend shown in **Figure 2.1**(a) helped to accelerate the wet etching process over the large parylene area.

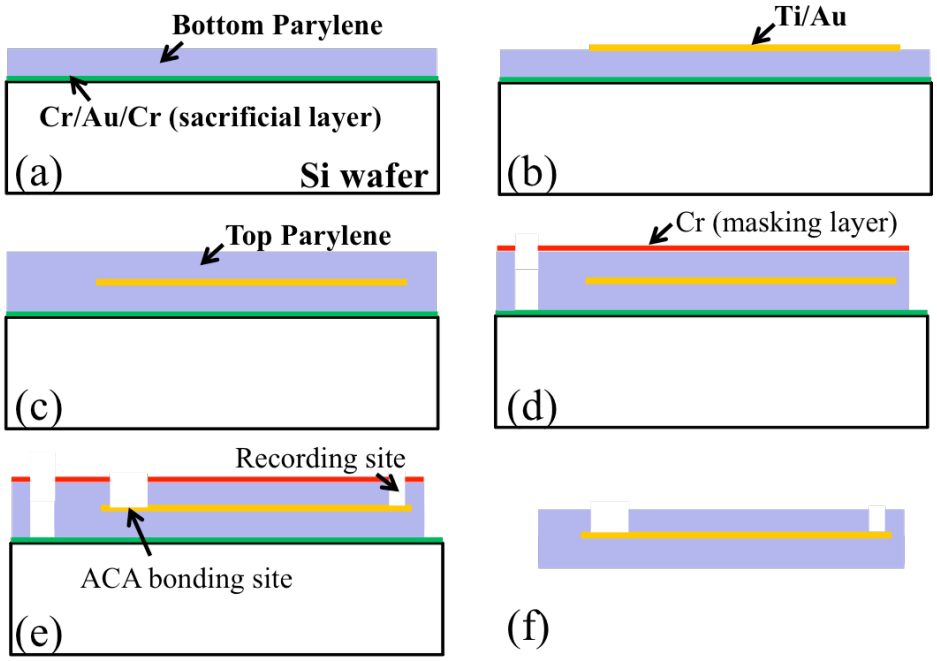

Figure 2.2: Fabrication process: (a) deposition of Cr/Au/Cr sacrificial layer and bottom parylene; (b) evaporation and lift-off of Ti/Au electrodes and interconnections; (c) deposition of top parylene; (d) etching of field parylene using Cr as a mask; (e) etching of top layer parylene to form electrical contacts; (f) final release of probe by etching Cr.

The fabrication yield was higher than 95% with a total of 265 probes released from a 4-inch-wafer. The microscope images of the probes are shown in **Figure 2.3**. The design in **Figure 2.3**(a) maximized the electrode density at a given vertical pitch of 40 μm on each side of the shank. The design in **Figure 2.3**(b) aimed to further reduce tissue reactions near the electrodes by dividing the electrodes into two smaller groups. Gold electrical interconnections and the recording electrodes were clearly visible, and were outlined by the parylene layers with the minimum overlap area to completely insulate the metal. The SEM images in **Figure 2.4** show straight shanks and smooth surface of parylene layers. The narrowest section of the cantilever-like parylene structure was only 8-μm-wide to cover the interconnection line that reached the deepest electrode.

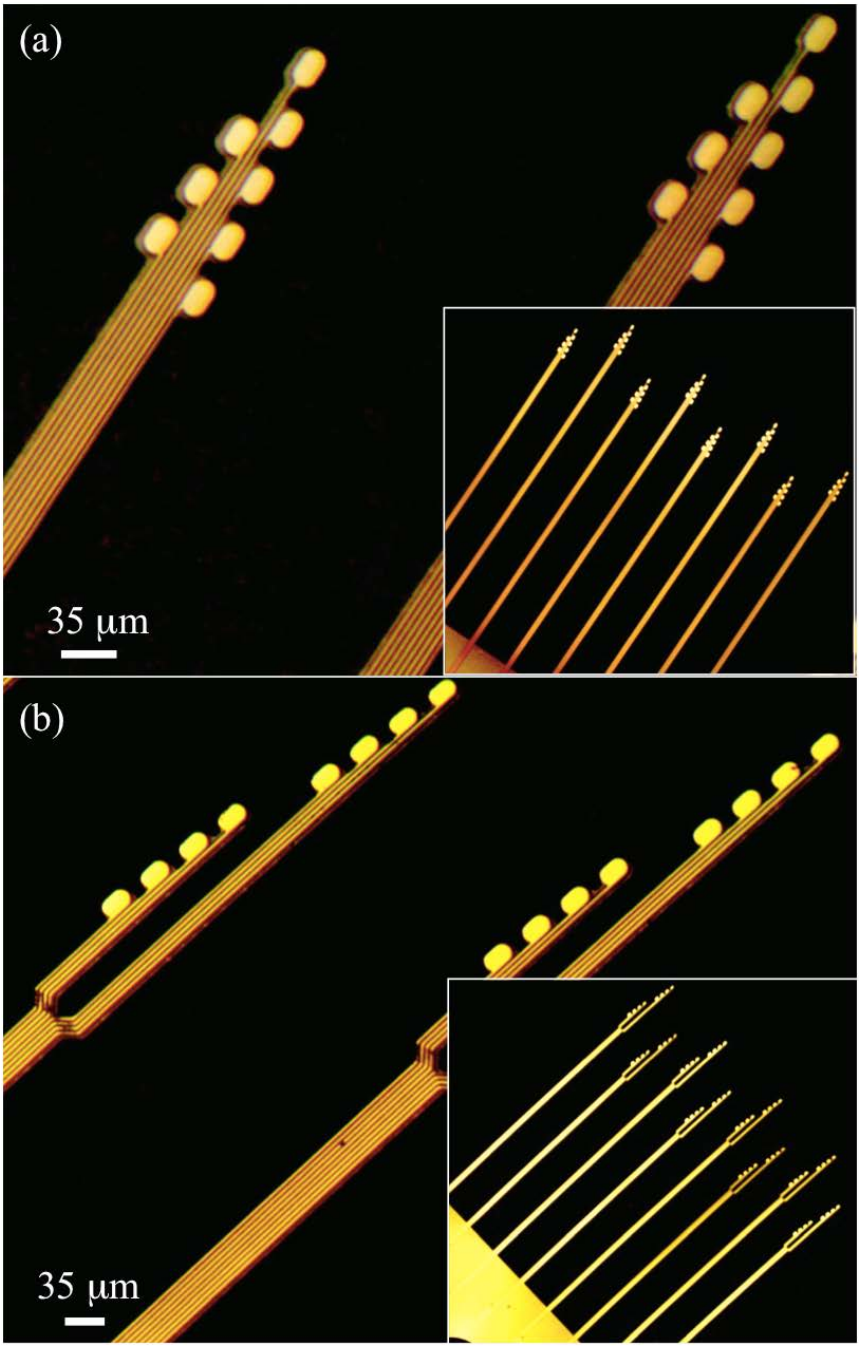

Figure 2.3: Microscope images of the fabricated probes with two different electrode configurations in (a) and (b).

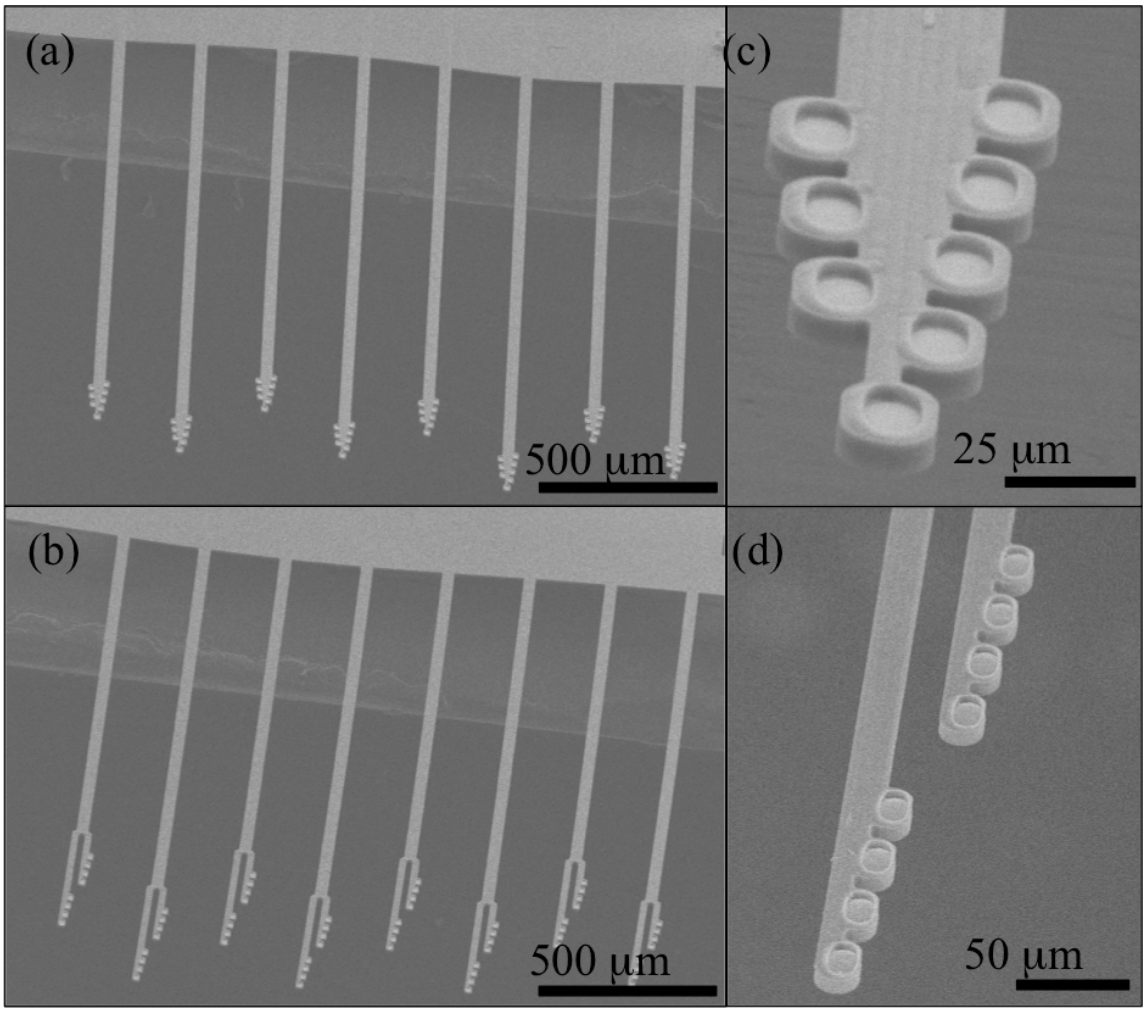

Figure 2.4: SEM images of the fabricated probes with two different designs in (a), (b) and their respective magnified view in (c) and (d).

2.4. Silk Patterning

Several methods to pattern silk fibroin have been developed by this work in order to coat the polymer probes. In each case, aqueous silk solution with protein concentration of 0.15g/mL was used. A simple dip-coating approach was first explored to embed a single-shank probe[76]. The advantage of the dip-coating method is that it required no alignment procedures to coat silk around the probes. However, there are several drawbacks to this simple method. Firstly, the coating could not exceed thickness of greater than 10 μm. With limited stiffness, it cannot be used for applications that

require probe penetration into deeper regions of the brain. In addition, the shape of the silk coating relies on the probe structure, which served as a scaffold during dip-coating. Therefore, the shape of the probe should resemble the final structure of silk and be able to provide features such as a sharp tip to assist the insertion procedure. This significantly sacrifices design freedom of probe dimension and shape to minimize the tissue reaction. Lastly, dipping the entire probe shank into aqueous silk solution would inevitably cover the electrodes, which can potentially create a void between active neurons and the recording sites even after silk degradation *in vivo*.

To improve the coating performance, a new patterning method was developed to address all of the problems encountered during the dip-coating experiments. Using standard soft lithography techniques, a PDMS mold was created to form trenches that resembled the final structure of the silk coating. The PDMS surfaces were first pretreated with isopropyl alcohol (IPA), which allowed aqueous silk solution to easily flow into the otherwise hydrophobic PDMS mold. The top surface of the mold remained hydrophobic, which conveniently served as a barrier to prevent silk solution from overflowing out of the trenches. The silk solution was allowed to dry over 12 hours at room temperature. Finally, the dried silk protein can be easily de-molded from the soft PDMS substrate without any structural deformation of the shanks. With this method, the silk protein can be patterned into any arbitrary shapes as shown in **Figure 2.5**. The fabricated silk structures have perfectly straight shanks, which are critical for insertion. The thickness of the dried silk protein was controlled by the trench depth and silk concentration. The silk thicknesses that were later used for insertion tests were 30 μm,

45 μm, and 65 μm, which were molded using trench depth of 40 μm, 75 μm, and 95 μm, respectively.

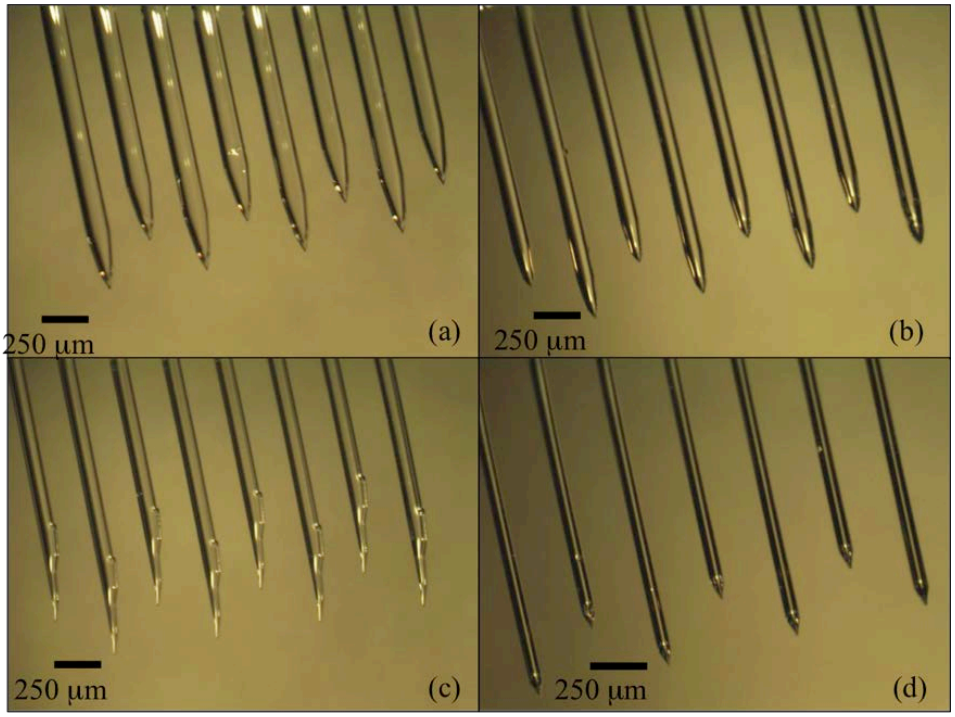

Figure 2.5: Silk patterned by PDMS molding for various shapes and mechanical stiffness.

2.5. High throughput packaging

In order to electrically connect the parylene probe to the PCB in a high throughput manner, a single flip-chip bond method using anisotropic conductive adhesive (ACA; Shiva Consulting, Carmel, IN)[82] was developed to simultaneously connect all 64 contact pads on the probe to the corresponding contact pads on the PCB. In this procedure, 4 μL of ACA was dispensed onto the PCB within a grooved boundary that contained all 64 contact pads. The ACA was degassed in a desiccator (20 mmHg) for 30 min to remove air bubbles. The parylene probe was then coarsely aligned with the bonding region on the PCB with the contact pads facing down. Because of the optical

transparency of parylene and a set of alignment keys on the probe (**Figure 2.1**(a)), the 64 pairs of contact pads between the probe and the PCB can be easily fine-tuned to overlap perfectly with each other. The assembly was then positioned at the center of a magnet (Dexter Magnetic Technology, Elk Grove Village, IL) inside an oven at 100 ºC. During the curing process, randomly distributed magnetic particles inside the ACA epoxy became aligned to the magnetic field, which was perpendicular to the PCB surface (**Figure 2.6**(a)). When the epoxy hardened, the magnetic particles became fixed in position to form a dense forest of vertically conducting columns with approximately 20-μm-pitch. These columns electrically connected the aligned pairs of contact pads while the epoxy resin insulated each column from the adjacent ones. **Figure 2.6**(b) shows a microscope image of the cross section of the ACA, demonstrating the formation of conductive columns inside the epoxy. **Figure 2.6**(c) shows a magnified top view of a probe aligned and bonded to the PCB. Each contact pad on the probe (Ti layer facing up) clearly overlapped with the Au contact pad on the PCB with a pitch of 200 μm. **Figure 2.6**(d) shows the overall view of the parylene probe bonded to the PCB with a Hirose connector at the backend for external connections to the recording system. Because these electrodes were relatively small ($175\mu m^2$) and were made out of Au, the expected impedance should be in the order of several mega ohms. In order to reduce the impedance for higher signal-to-noise ratio recording, the electrodes were electroplated. To characterize the impedance change, half of the electrodes of 3 test probes were electroplated and the impedances were measured using NanoZ (Tucker-Davis Technologies, Alachua, FL). Out of these 3 tested probes, around 95% of the electrodes were considered electrically functional, with impedance of 3-7 MΩ at 1 kHz prior to

electroplating. Only these functional sites were sampled for the statistical analysis of the impedance. As can be seen in **Table 1**, electroplating has reduced the impedance level of the electrodes down to less than 1-2 MΩ at 1 kHz (roughly 3 folds) due to the increased surface roughness.

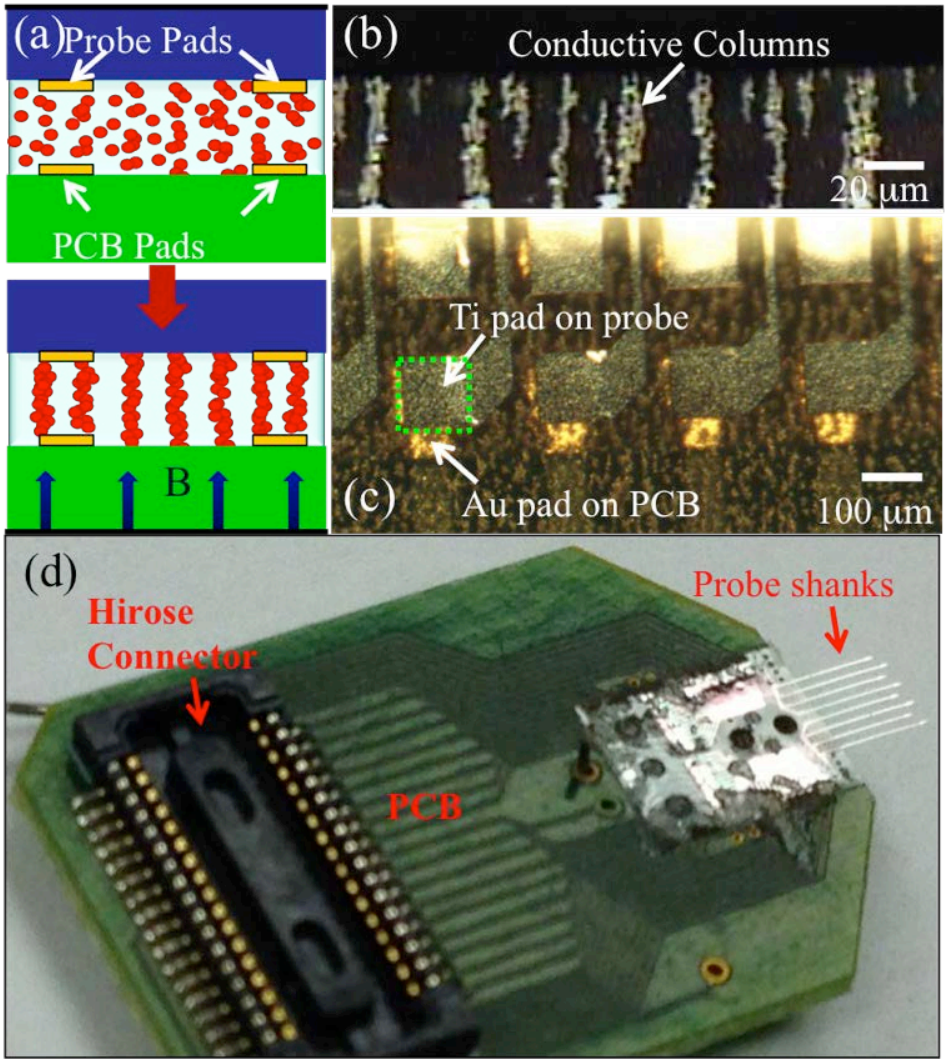

Figure 2.6: High throughput ACA bonding: (a) schematics showing the working principle of ACA; (b) microscope image of the cross-section of ACA showing the conductive columns; (c) microscope image of the top view of the assembly showing all of the probe pads aligned to the corresponding PCB pads; (d) image of the entire assembly with the probe bonded to the PCB and a Hirose connector attached at the opposite end.

Probe #		*Site 1-32 (plated)*		*Site 33-64 (non-plated)*	
		Magnitude (MΩ)	**Phase (°)**	**Magnitude (MΩ)**	**Phase (°)**
1	**n**	**32**		**32**	
	μ	**0.73**	**-83.28**	**3.35**	**-81.03**
	σ	**0.41**	**0.61**	**1.34**	**2.05**
2	**n**	**29**		**28**	
	μ	**1.83**	**-84.47**	**4.32**	**-80.33**
	σ	**1.17**	**2.63**	**2.01**	**2.93**
3	**n**	**30**		**31**	
	μ	**2.03**	**-83.14**	**7.49**	**-76.50**
	σ	**0.92**	**1.35**	**1.16**	**2.19**

Table 1: Impedance and phase statistics of 3 probes measured at 1 kHz: μ = mean, σ = standard deviation, n = sample size (number of electrically functional sites).

2.6. Silk coating onto packaged probe

In order to define the silk coating around the probe shanks with a minimal margin, the probe must be accurately aligned with the PDMS mold prior to silk casting. The PDMS mold was designed with only 5-μm-alignment margin with the parylene probe on each side to minimize the silk coating width. The PDMS mold and the probe (bonded to the PCB via ACA) were separately held by two micromanipulator stages. Because of the probe shank flexibility and electrical charges at the parylene surface, it would be extremely difficult to precisely lower the probe into the PDMS mold with all 8 shanks simultaneously aligned to each of the corresponding trenches using the

micromanipulators. Typically, the electrostatic force would prematurely pull the suspended probe shanks towards the mold from a large distance (>500 μm); and together with friction, it would prevent further adjustment of the probe position. To overcome this challenge, de-ionized water was first injected into the PDMS mold to fill the trenches. The probe was then coarsely aligned to the water-filled trenches using a micromanipulator (now there is negligible electrostatic attraction). Once the probe shanks come into contact with water, they were bounded by surface tension, which prevented them from escaping the trench. Fine-tuning of the shank position can then be done easily using the micromanipulator as the probe shanks float on top of the frictionless water surface. In addition, floating on top of the water surface also reduced the degree of freedom of the probe shanks to three (movements in plane with the water surface) from six, if they were suspended in air. The water evaporated within a few minutes, resulting in lowering of the probe shanks to the bottom surface of the mold. Once the shanks were aligned to the mold, the silk solution was then injected into the trench (**Figure 2.7**(a)). Because of the water stiction force that firmly attached parylene to the PDMS mold, silk was only coated onto the backside of the probe shanks. This method prevented silk from covering the recording sites, which were positioned with contacts facing the mold bottom surface during alignment. Once silk dried, all 8 shanks can be easily de-molded from the PDMS without curling as shown in **Figure 2.7**(b) and (c), which was critical for insertion. The magnified images in **Figure 2.7**(d) and (e) show that the silk coating can be defined with very sharp tips and in precise alignment with the parylene probe.

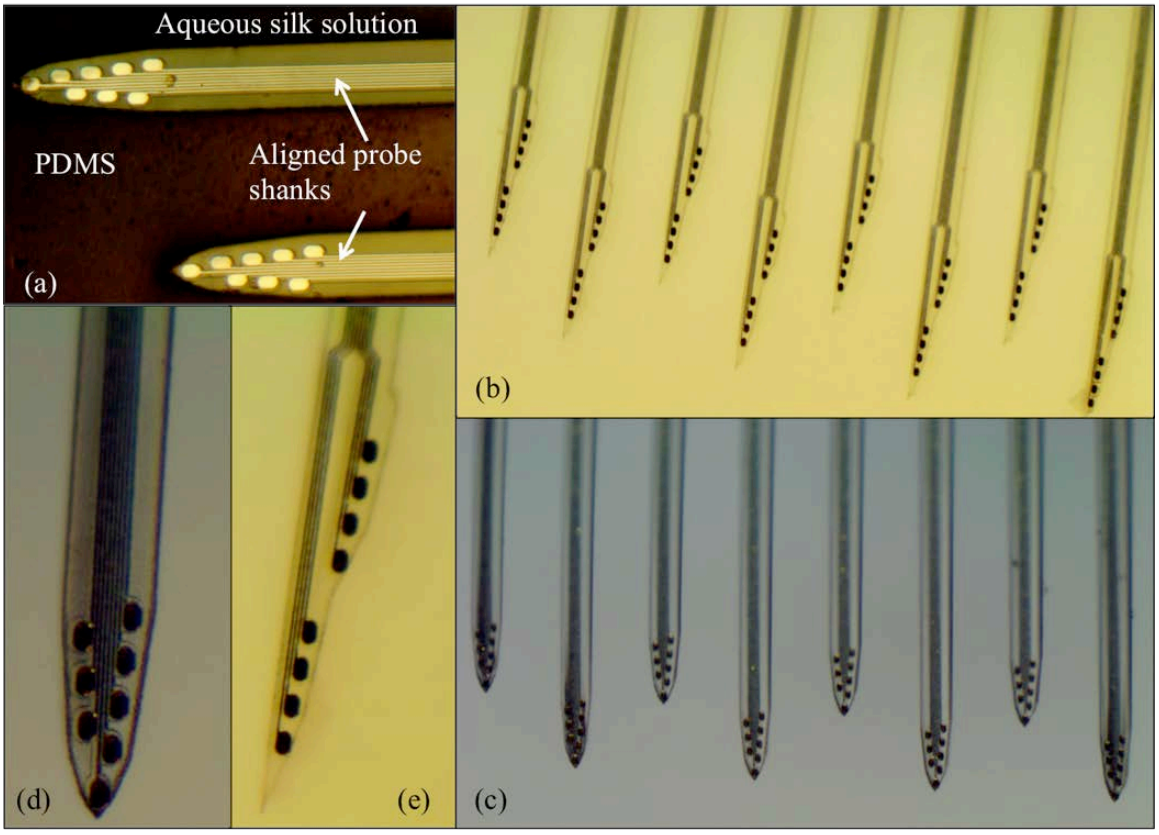

Figure 2.7: Silk coating procedure onto the packaged probe: (a) alignment of probe to the PDMS mold and casting of aqueous silk solution into the mold; (b), (c) two designs of the probe coated with silk; (d) magnified images of the probe tips of the two designs.

2.7. Insertion tests

Silk inevitably loses stiffness as it hydrates when coming into contact with the cerebrospinal fluid (CSF). It is difficult to predict the *in vivo* degradation dynamics and the required silk dimensions for a successful insertion. Many variables such as silk surface-area-to-volume ratio, number of shanks, quality of the craniotomy, insertion speed, etc. can have significant impact on insertion. In order to minimize tissue damage, and especially to avoid breaching the blood-brain barrier during insertion, the silk dimensions need to be minimized. The silk mold should have the minimum area

required to cover the parylene probe and to form a sharp probe tip. The minimum required coating thickness (and therefore the depth of the PDMS mold trenches) was determined empirically after insertion experiments. The silk shanks were molded in thicknesses of 30 μm, 45 μm, and 65 μm, respectively, and were attached to dummy PCBs. Half of the samples were water-annealed for 3 hours in a desiccator (under 20 mmHg) to increase silk's stability in water. Various coating shapes (shown in **Figure 2.5**) were prescreened by test insertions into 0.6% agar gel. All except for the narrowest (50-μm-wide) design shown in **Figure 2.5**(d) penetrated the agar gel. The design in **Figure 2.5**(a), on the other hand, displaced significant volume of the gel during penetration and was discarded due to expected severe tissue damage during insertion. We chose the two designs and the *in vivo* insertion experiment was then carried out for only the coating designs shown in **Figure 2.5**(b) and (c), both having a shank width of 75 μm. These probes were stereotactically inserted down to a depth of 1.4 mm in 3 seconds, targeting the layer-V of motor cortex in an adult Long Evans rat. The insertion results were quantified based on how many shanks were inserted into the brain without buckling. **Table 2** shows the minimum thicknesses for 100% penetration rate were 45 μm and 65 μm for water annealed silk and non-annealed silk, respectively. **Figure 2.8**(a) and (b) show the insertion experiment before starting and after completion, respectively. **Figure 2.8**(c) shows the brain sectioned at 1 mm in depth without staining on the second day post-surgery. The 8 insertion wounds with 250-μm-pitch can be seen clearly, indicating that all shanks were successfully implanted in parallel without deviation from the intended track.

Probe	Thickness (μm)	H_2O Annealing (hr)	Number of Shanks Penetrated
1	30	0	0/8
2	30	0	0/8
3	30	3	0/8
4	30	3	5/8
5	45	0	0/8
6	45	0	6/8
7	45	3	8/8
8	45	3	8/8
9	65	0	8/8
10	65	0	8/8

Table 2: *In vivo* insertion test results that measured the quality of insertion based on how many probe shanks penetrated the pia mater.

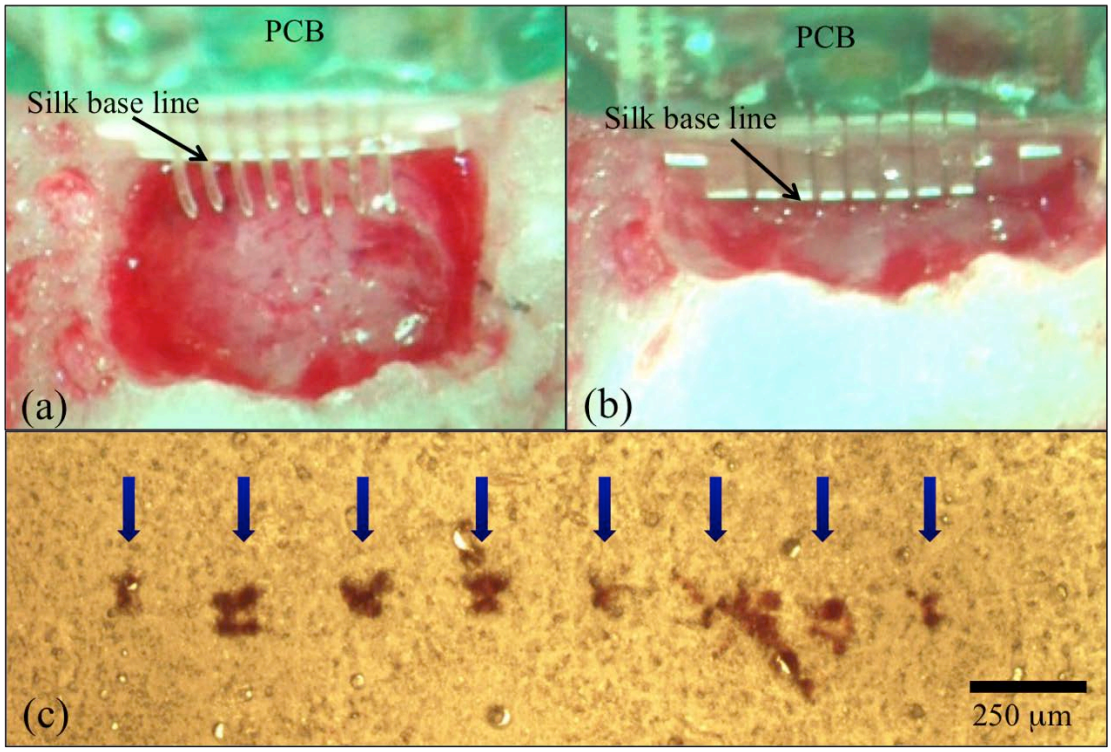

Figure 2.8: Insertion experiment of the silk-coated probe: (a) before entering the pia mater and (b) after successfully reaching a depth of 1.4 mm; (c) histology showing 8 penetration wounds in parallel at 1 mm below the surface of the brain.

2.8. Chronic recording

For chronic *in vivo* studies, one probe was implanted into each of the 6 Long Evans rats with the same procedure used for the insertion experiments. After successfully positioning the recording electrodes into the layer-V motor cortex, the craniotomy was covered by Kwik-sil. Finally, the PCB was secured onto the skull by dental cement.

The animals were allowed to recover from surgery for 3 days before the first recording session. **Figure 2.9** shows a representative spike waveform recorded on the 27^{th} day post surgery. After manually removing epochs with clear noise artifacts, two analysis approaches was used to assess the ability of the probes to record neural activity. Firstly, the rate of spiking events crossing the 4σ threshold was measured. Secondly, the power spectra of the recorded signals were examined. Here, "spikiness" was defined as the total signal power within the spike bandwidth (600 Hz - 6 kHz). Power spectra may indicate higher fidelity spike detection than threshold-crossing event counting because it is less likely to generate false positive spike counts from noise events having amplitude over the 4σ threshold. **Figure 2.10** shows 9 representative channels that can be distinctively separated into three groups in a particular 20-minute recording session. The first group (blue), which recorded obvious large-amplitude spike signals and local field potential (LFP), showed highest power over the spike band. The second group (green), which only recorded LFP but no obvious large spike signals showed lower power over the spike band. At lower frequency, the power spectra (< 100 Hz) matched that of the first group, indicating that these electrodes were indeed functional but only recorded LFP - possibly due to large separation distance from the nearest active neuron. The third

group (red) was chosen among those channels that showed high electrode impedance (>5 MΩ) prior to implantation: clearly, these channels did not record any physiological signals but contained large low frequency noise. These observations were reflected by the distinctive power spectra pattern showing high power density below 20 Hz and minimal power density within the spike band.

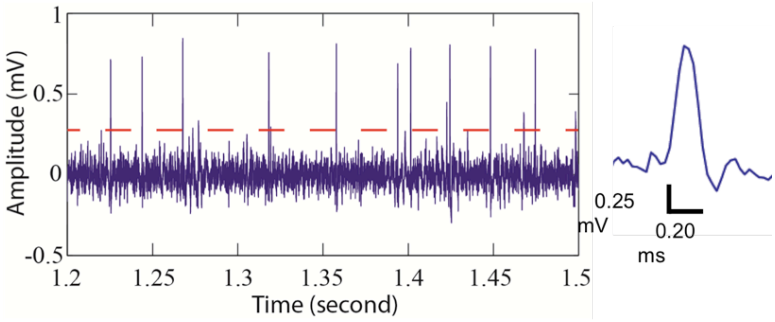

Figure 2.9: Spike train recorded on the 27th day post surgery for a 0.3 second recording window (left) and a magnified single spike waveform (right).

The chronic recording quality was evaluated by co-plotting the average threshold crossing event rate and the spikiness over time in **Figure 2.11**. The spikiness detection was more consistent than the threshold crossing event rates with less fluctuation over time, which may be due to the occasional high amplitude noise events counted in the automated threshold (4σ baseline) crossing detection. **Figure 2.12** shows the heat map of spikiness from each recording channel in a probe. From these results, no significant signal degradation in spike event rate or power was detected, indicating functional recording over period of 6 weeks.

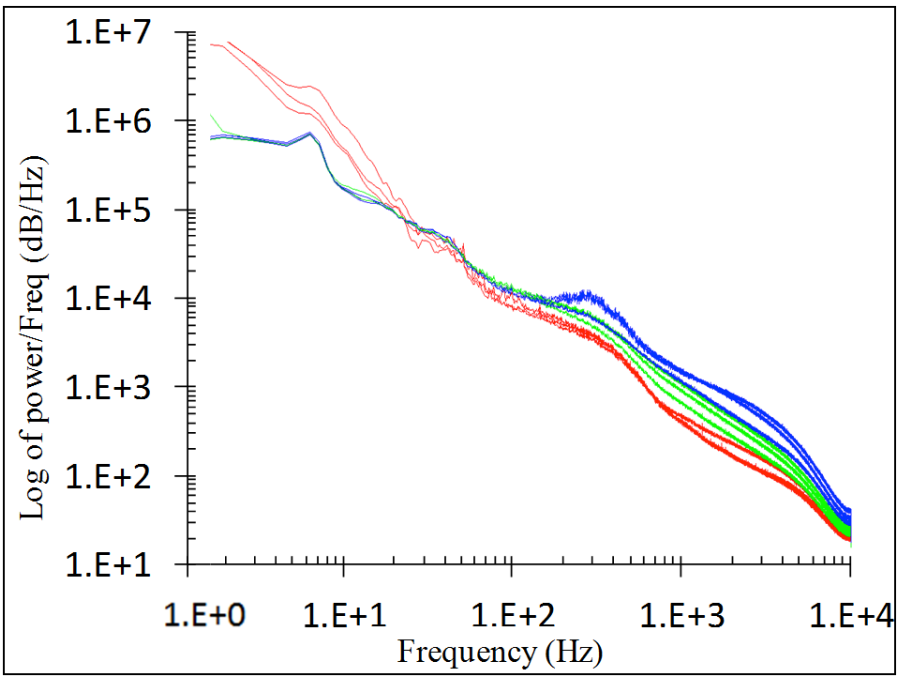

Figure 2.10: Power spectra analysis over 20-minute recording session to measure spikiness. The recorded spectra are separated into 3 groups: LFP and spike (blue), LFP only (green) and noise only (red).

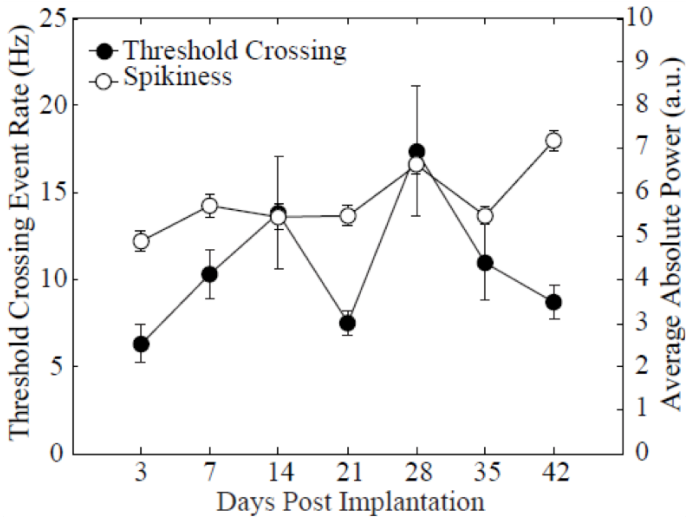

Figure 2.11: Average threshold crossing event rate and average absolute power summed between 600 and 6 kHz over each recording session over a period of 6 weeks.

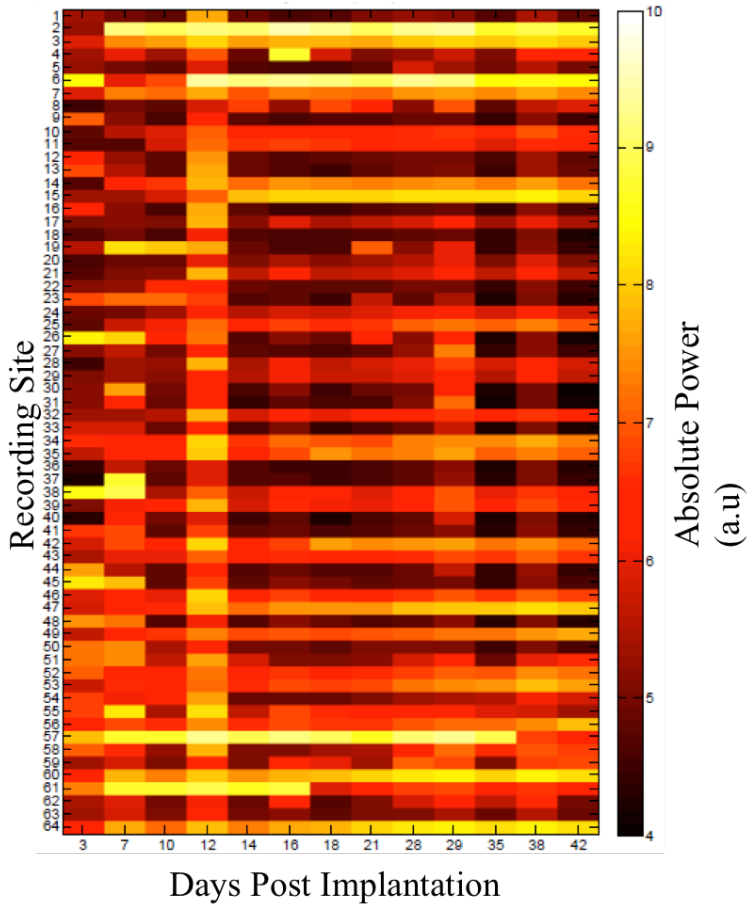

Figure 2.12: Heat map of absolute power summed between 600 and 6 kHz recorded over 42 days with each recording site from one animal.

2.9. Discussion

In this work, a biodegradable silk-backed parylene neural probe was designed and used for recording in behaving Long Evan's rats. The minimal silk dimension has been experimentally determined to obtain the necessary mechanical stiffness that would last over the entire stereotactical insertion process for 8-shank 64-channel probes. The flexible parylene probe can be designed in any geometry because the mechanical stiffness required for insertion was predominantly controlled by the properties of a biodegradable coating of silk fibroin. This allows complete design freedom of the probe in terms of material, size and shape. The *in vivo* recording quality was evaluated by both

average threshold crossing rate and the “spikiness” over time. The spikiness detection was more consistent than the threshold crossing event rates with less fluctuation over time, which may be due to the occasional high amplitude noise events counted in the automated threshold (4σ baseline) crossing detection. In fact, even though the activities recorded from a particular recording site fluctuated between recording sessions, the average performance improved slightly over time as shown by **Figure 2.11**. This observation can be explained by the recovery process from the initial insertion wound[83] as silk coating degraded over time. Still, 6-weeks recording is not sufficient to evaluate chronic recording performance of the new probes. In addition, it is still inconclusive whether the new design has significantly improved the reliability of recording without comparison with the conventional silicon-based probes. Such comparison may require extensive studies under carefully-controlled experiments, as there are often multiple design parameters, insertion methods, and even differences among animals that can affect the recording quality. Nonetheless, the method described in this paper can be utilized to optimize polymer probe structures without the design constraint of required stiffness in order to individually evaluate design parameters such as probe size, flexibility, electrode density, etc. for prolonged recording lifetime. In the future, extended studies should quantitatively correlate the recording quality and immunohistochemistry followed by comparison of the results against existing probe designs.

CHAPTER 3

INTEGRATED WAVEGUIDE OPTICAL STIMULATION PROBE

3.1. Introduction

Recent advances in optogenetics enable cell-type specific activation and silencing of targeted neurons with high spatiotemporal resolution[17]. Although optogenetics promises exciting new possibilities for neuroscience research, to date there is still an unmet need for reliable implantable tools to precisely deliver light to the targeted neurons and to simultaneously record the electrical signals from the individual neurons. Typically, optical stimulation has been achieved by placing a single light source on the surface of the brain[14] or a thick fiber in the brain parenchyma a few hundred microns away from the recording sites[84]–[90]. This approach inevitably activates many unmonitored neurons, making the separation between direct and population-mediated effects impossible. The high intensity used to activate deep neurons may generate multiple superimposed spike waveforms[91] and considerable light artifacts[86], [89], [90].

Current state-of-the-art implantable optical probes include the assembly of four tetrodes (25 μm in diameter each) symmetrically attached about the perimeter of a 200-μm-diameter optical fiber[85], [91]. Although the components of such systems are readily available, the distance between the tetrodes and the fiber cannot be accurately

controlled by manual alignment. In addition, the assembly displaces a relatively large neuronal volume and may cause tissue damage along its insertion path[66], limiting its potential for scaling up towards the large number of sites. In another innovation, a complete multi-site/multi-color optical stimulation and electrical recording system was demonstrated by using diode-coupled optical fibers attached to commercial multi-shank silicon recording probes[92]. The manual attachment of fibers glued to each probe shank is very labor-intensive, resulting in potential alignment inaccuracy and contamination of the recording sites by misplaced glue. Fabrication of waveguide array integrated onto a single silicon shank with dimensions similar to a 200-μm-diameter optical fiber was reported[93], but recording electrodes were not integrated onto the probe. Other recent work demonstrated a polymer-based neural probe integrated with SU-8 waveguide, electrodes and a microfluidic channel[94]. Although *in vivo* experiment was performed, spontaneous neural activities were only recorded in the tip-most electrodes (2 out of 9) that were farthest away from the bulky waveguide and microfluidic channel measuring over 200-μm-thick and 190-μm-wide. In addition, only a single neuron responded indirectly to blue light stimulation with excessively high power (1 to 2 mW)[94]. Another SU-8 design demonstrated the coupling of light from a bare laser diode chip[95]. Although the compact diode assembly presents significant advantage for chronic experiments with moving animals, no *in vivo* validation was reported, and the probe shanks were still too bulky for applications that require concurrent optical targeting and electrophysiological monitoring of dense neural population regions such as the hippocampus.

3.2. Design

In this work, the first implantable neural probes, designed and fabricated with integrated waveguides, are illustrated in **Figure 3.1**. This approach provides spatially-confined stimulation (activation and silencing) of simultaneously monitored neurons by enabling local light delivery precisely above the recording sites at specific wavelengths of choice. The lithographically-defined probe shank was designed with minimal dimensions to contain all necessary optical and electrical components, in order to minimize insertion-induced tissue damage and foreign body reactions, as well as to reduce alignment tolerance between the optical stimulation site and the electrical recording sites.

The first version waveguide is composed of an SU-8 core (refractive index of 1.70) with a bottom oxide-cladding layer (refractive index of 1.46) that can transmit light at specific wavelengths for optical stimulation of targeted neurons. A U-groove was lithographically defined at the proximal end of the waveguide for self-alignment with an optical fiber. Later, additional probe schemes incorporated various optical waveguides for different optogenetic applications[96]. Curved SU-8 has been patterned to form an optical splitter (**Figure 3.1**(a)) and an optical mixer waveguide (**Figure 3.1**(a)) for advanced optical functions. Dual-shank probes integrated with double-waveguides on each shank for stimulation at multiple sites, each independently controlled by a corresponding light source, were also realized as shown in **Figure 3.1**(c)[97]. The transmission efficiency of blue light (λ=473nm) from the fiber to the stimulation site through the SU-8 waveguide was measured at roughly 0.67%.

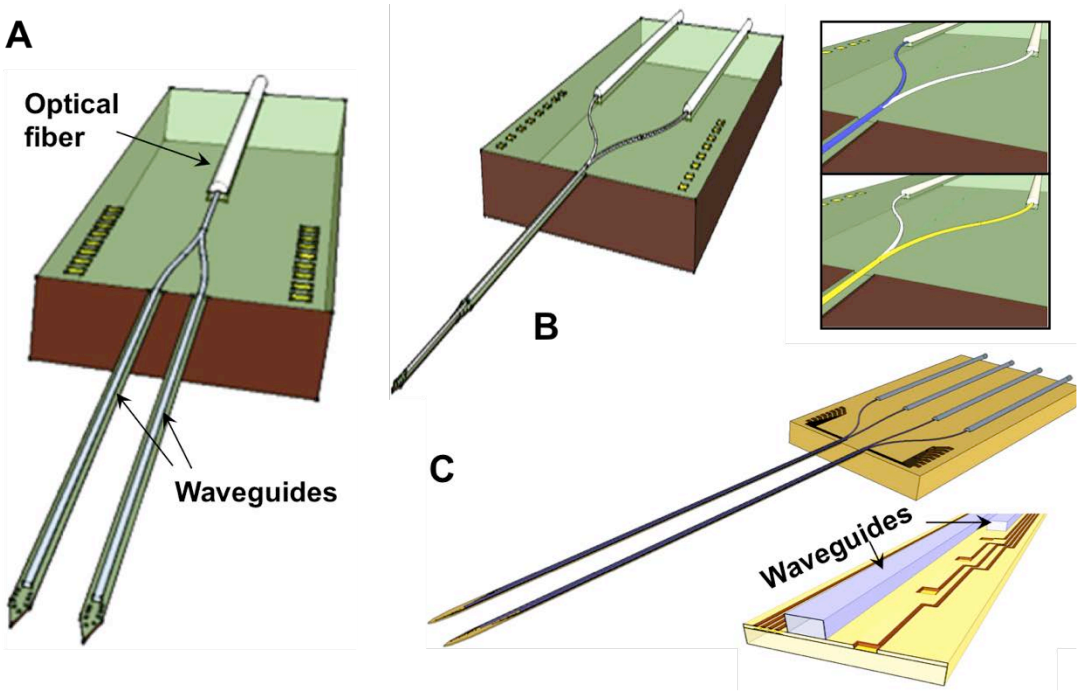

Figure 3.1: Schematics of waveguide configurations designed for the first generation integrated waveguide probes: (a) optical splitter; (b) optical mixer[96]; (c) dual waveguide per probe shank[97].

Although the probes using SU-8 waveguide core proved functional in terms of optical power transmission immediately after the fiber assembly, when the same probes were delivered to Prof. Buzsaki's lab at Rutgers University for animal tests, no light output can be detected at the stimulation sites. The source of failure was inspected and it was observed that the SU-8 waveguide could be damaged by the laser source during prolonged testing due to heating. In addition, SU-8 could absorb ambient moisture[98], which could adversely affect its transmission as well as coupling efficiency.

As an alternative to using SU-8 as the waveguide core, improvement has been made using an all-dielectric waveguide. To determine whether the integrated device has benefits to record in a densely packed brain region, the hippocampus CA1 pyramidal layer was chosen to be the ideal target in a rodent brain. Simplifying the design for the

initial feasibility study, the probe was designed with 8 nearby recording electrodes and a single waveguide, all integrated on a single silicon shank as shown by the schematics in **Figure 3.2**(a). The overall shank dimensions were designed to minimize tissue damage while maintaining sufficient mechanical strength for insertion and having enough space to contain all optical and electrical components. The shank thickness was defined by the top silicon layer of our starting Silicon-On-Insulator (SOI) wafer, which can be commercially made with 15 μm in thickness and an accuracy of ±0.5 μm. Combined with a lithographically defined sharp tip, the thin probe can easily penetrate the pia mater with minimal tissue damage along its insertion path. For this particular probe design, the shank width was 70 μm, the minimum dimension to carry 8 interconnection lines and a waveguide given the fabrication process constraints. The interconnection lines carried electrical signals from the 8 recording electrodes to the bonding pads, which were wirebonded to a custom-made printed circuit board (PCB). The waveguide delivered light from an aligned optical fiber to the stimulation site. The U-groove at the backend of the probe was designed to perfectly fit a 125-μm-diameter optical fiber, having the fiber core (50 μm in diameter) in an aligned position with the integrated waveguide as shown in **Figure 3.2**(b). The optical fiber provided a convenient coupling intermediate between an external diode-pumped solid-state (DPSS) laser source and the waveguide.

The optical waveguide was composed of a 5-μm-thick oxynitride core (index of refraction: 1.51) surrounded on each side by a 3-μm-thick oxide cladding (index of refraction: 1.46). The waveguide width tapers from 28 μm at the end proximal to optical fiber, to 14 μm at the distal end. The larger cross-sectional area at the proximal end

allowed higher coupling efficiency to the optical fiber core, while the smaller cross-sectional area at the distal end (**Figure 3.2**(c)) allowed spatial confinement of light exiting from the waveguide and minimized tissue damage. Assuming tissue isotropy and light scattering, the distribution of light coming out of the waveguide in the brain tissue can be estimated[92], [99]. Given a horizontal pitch of 40 μm between the top two recording sites and a light output of 0.5 mW at the waveguide tip, positioning the tip of the waveguide 50 μm above the top recording site placed all recording sites within a light cone with intensity above 7 mW/mm^2 (**Figure 3.2**(d)), which was sufficient to activate/silence single-units *in-vivo*[92].

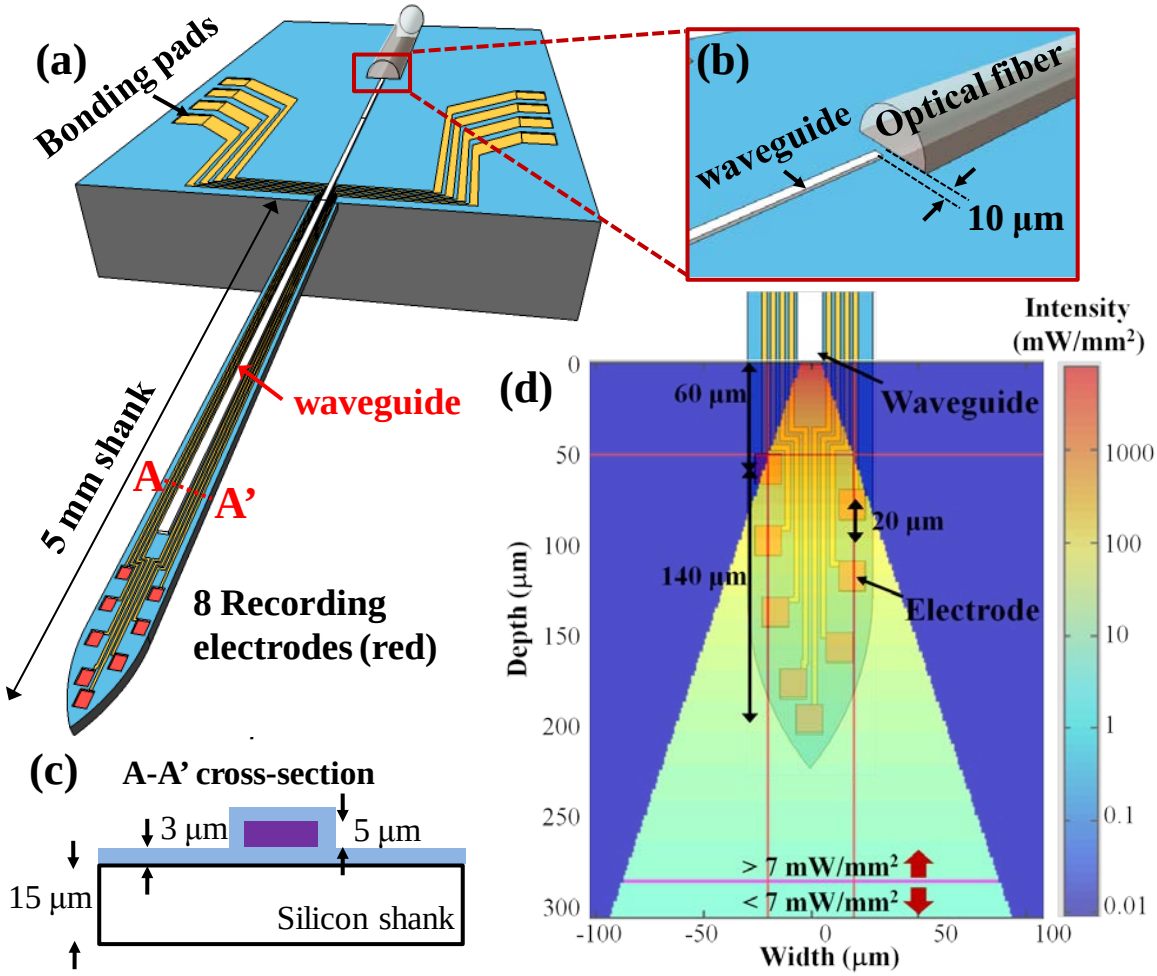

Figure 3.2: Design of single shank, monolithically-integrated probe: (a) 3-D schematics of overall probe design, (b) Coupling junction between the optical fiber and the integrated waveguide, (c) A-A' cross-section showing the waveguide with oxynitride core (purple) and oxide cladding (blue), (d) Simulation results of light intensity distribution as light propagates through the brain tissue.

Monolithic integration of both electrical and optical components of the neural probe allowed precise definition of the optical stimulation site and the recording electrodes in terms of position, size and alignment in a high-density array. For example, to enable single unit recordings in structures with dense cell body layer, such as neocortex and hippocampus, recording sites span 140 µm in depth with each electrode separated by a pitch of 20 µm[100]. Sizing the electrode area has a tradeoff between low

impedance, high probability of coming into proximity of an active neuron (large recording area) and the ability to distinguish single unit activity (small recording area)[101]. In this work, each electrode was designed with an area of 143 μm^2 to achieve low impedance and to record from dense populations of individual neurons (soma diameter 10-20 μm) in the neocortex and hippocampus. The accurate alignment between the waveguide and electrodes ensures precise delivery of light to the neurons monitored by the electrodes with minimal power. The spatially confined, low power stimulation generates less heat and minimizes electromagnetic interference to the recording channels, as well as unintended excitation of nearby neurons.

3.3. Fabrication process

Figure 3.3 shows the probe fabrication steps. Briefly, the probes were fabricated with Silicon-On-Insulator (SOI) wafers for precise control of the shank thickness, which was defined by the top silicon layer (15 μm in our probes). The process began by depositing a nitride layer for the electrical insulation from the silicon substrate. This nitride layer in tensile stress compensated compressive stresses of much thicker oxide cladding layers deposited in later processes. Electrical interconnections and recording sites were patterned by lift-off, after evaporation of gold and sputtering of iridium respectively. The waveguide was composed of a 5-μm-thick oxynitride core layer patterned by plasma etching, and 3-μm-thick oxide cladding layers deposited to surround each side of the core. Deep reactive ion etching (DRIE) of the fiber groove was performed after waveguide patterning steps. Finally, the probes were released by a double-sided DRIE process with the final structure shown sitting on top of a US quarter

in **Figure 3.4**(a). The recording electrodes and the waveguide are shown in the microscope image in **Figure 3.4**(b). SEM images of the waveguide at the distal and proximal ends (fiber coupling junction) are shown in **Figure 3.4**(c) and **Figure 3.4**(d), respectively.

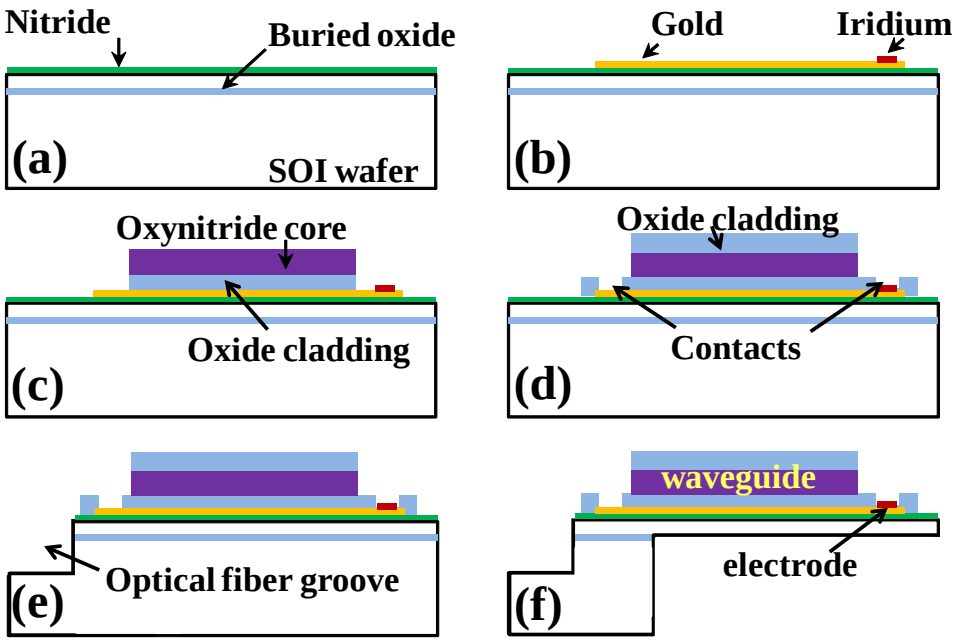

Figure 3.3: Outline of fabrication steps with cross-sections along the long axis of the probe: (a) Deposition of bottom insulation layer on SOI wafer, (b) Patterning of electrical interconnections and electrodes, (c) Defining waveguide bottom cladding and core layers, (d) Deposition of top cladding layer and formation of electrical contacts, (e) Silicon DRIE for the optical fiber groove, (f) Final release of the complete probe.

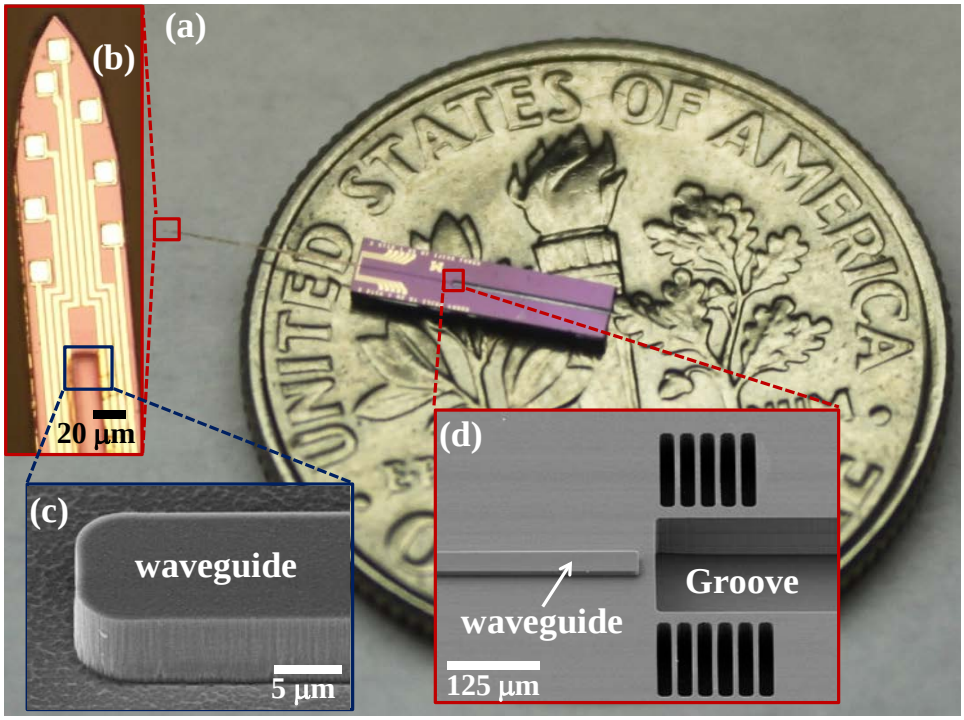

Figure 3.4: Images of the released probe: (a) Relative size in contrast with a US quarter, (b) Microscope image of probe tip showing the lithographically defined electrode array and the waveguide, (c) SEM image of the waveguide magnified at the distal end, (d) SEM image of the waveguide at the proximal end and the optical fiber groove.

3.4. Device performance characterization

The released probes were wirebonded to a custom-made printed circuit board (PCB) which has an Omnetics connector (A79038, Omnetics Connector Corporation, Minneapolis, MN) for electrical interface with an external amplifier. Impedances of recording sites were analyzed in saline solution with an impedance analyzer (HP 4194A Impedance/Gain-Phase Analyzer, Test Equipment Depot, Melrose, MA). The average impedance of the recording sites was 1.37 MΩ read at 1 kHz, which is sufficiently low to record neural signals with high signal-to-noise ratio.

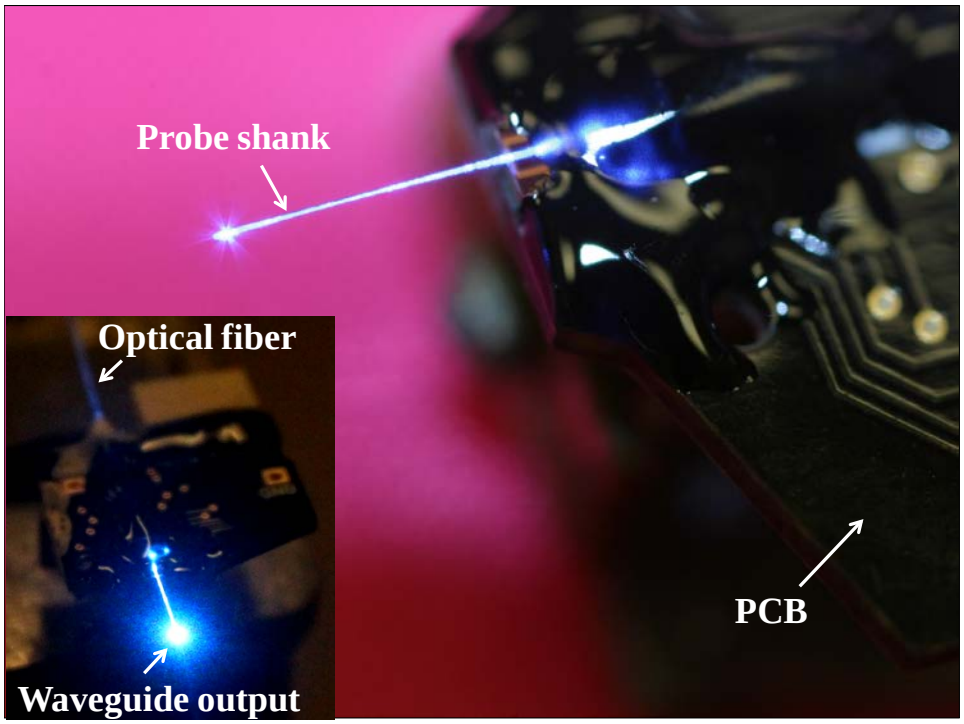

Figure 3.5: Fully packaged system with silicon probe bonded to the PCB and optical fiber aligned to the integrated waveguide. Light has been successfully guided from the laser source to the stimulation site.

The integrated waveguide was direct (butt-) coupled to a multi-mode optical fiber (GIF50, Thorlabs, Newton, NJ). The entire optical assembly is illustrated in **Figure 3.5** showing light transmitted from the 473 nm DPSS laser (Dream-Lasers), advancing through the optical fiber, and exiting at the distal end of the integrated waveguide. The overall transmission loss from the fiber to the stimulation site was 10.5 ± 1.9 dB (mean, SD; n = 3) for blue light. The optical loss predominately occurred at the coupling junction due to the cross-sectional area mismatch between the multi-mode fiber (core diameter = 50 μm) and the waveguide (area = 140 μm^2 proximal to the fiber). Nonetheless, coupling to a multi-mode fiber with 7 mW blue light output produced a total power of 660 μW at the end of the waveguide. Given the small aperture size of our waveguide (70 μm^2) at the distal end, this corresponded to an optical intensity of more

than 9400 mW/mm^2. In general, we observed an increase in transmission efficiency through the oxynitride waveguide as wavelength increased: roughly doubled efficiency when switching from 473 nm to 593 nm laser source and tripled efficiency upon switching from 405 nm (Sony KES-410ACA) to 639 nm laser diode (Opnext HL6359MG).

3.5. In-vivo experiments

The 8-site single-shank oxynitride waveguide probe was implanted into the neocortex and hippocampus of a wild-type rat expressing ChR2 under the CAG promoter. In the CA1 pyramidal layer, a brain region in which cells are tightly packed, the electrodes recorded spontaneous local field potentials and spiking activities of multiple single-units (**Figure 3.6**), indicating that the electrode configuration was adequate for recording from multiple singe cells and that the additional volume of the waveguide did not compromise the quality of the recordings. To demonstrate optogenetics, a 473 nm DPSS laser (Dream-Lasers) with a sinusoidal light output was adjusted to 120 μW peak power at the probe tip, corresponding to an intensity of ~51 mW/mm^2 at the center of the electrode array given the attenuation of optical intensity through neural tissue. This resulted in robust spiking of multiple single units; notably, different units exhibited distinct firing patterns during the light stimulus (**Figure 3.7**). For instance, the “red” unit occasionally fired one or two spikes during a given stimulus cycle. In contrast, the unit depicted in pink emitted multiple spikes per stimulus cycle.

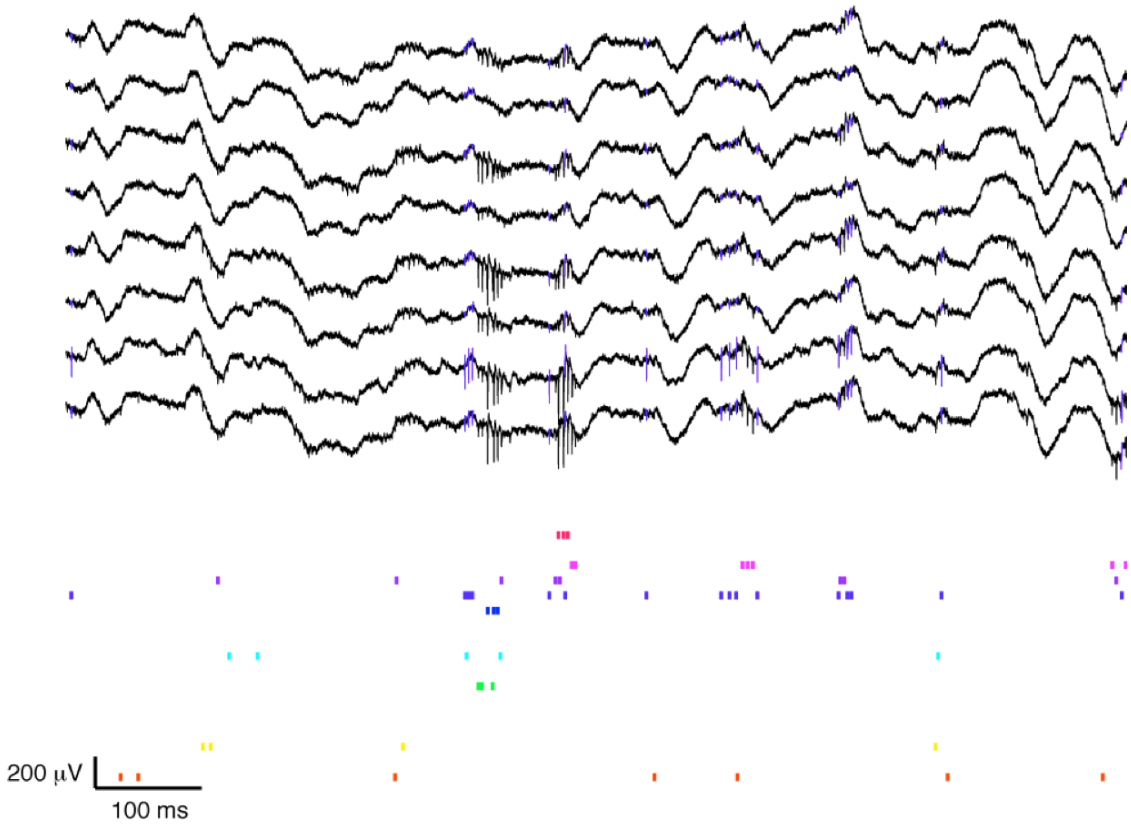

Figure 3.6: In-vivo recording of spontaneous local field potential and spiking activity from the CA1 pyramidal layer of a Long-Evans rat across 8 recording channels (sites 1 and 8 correspond to the deepest and shallowest recording sites respectively, which is shown with site 1 as the lowest trace). Each spiking event is marked and color-coded to represent a distinguishable single unit at the bottom.

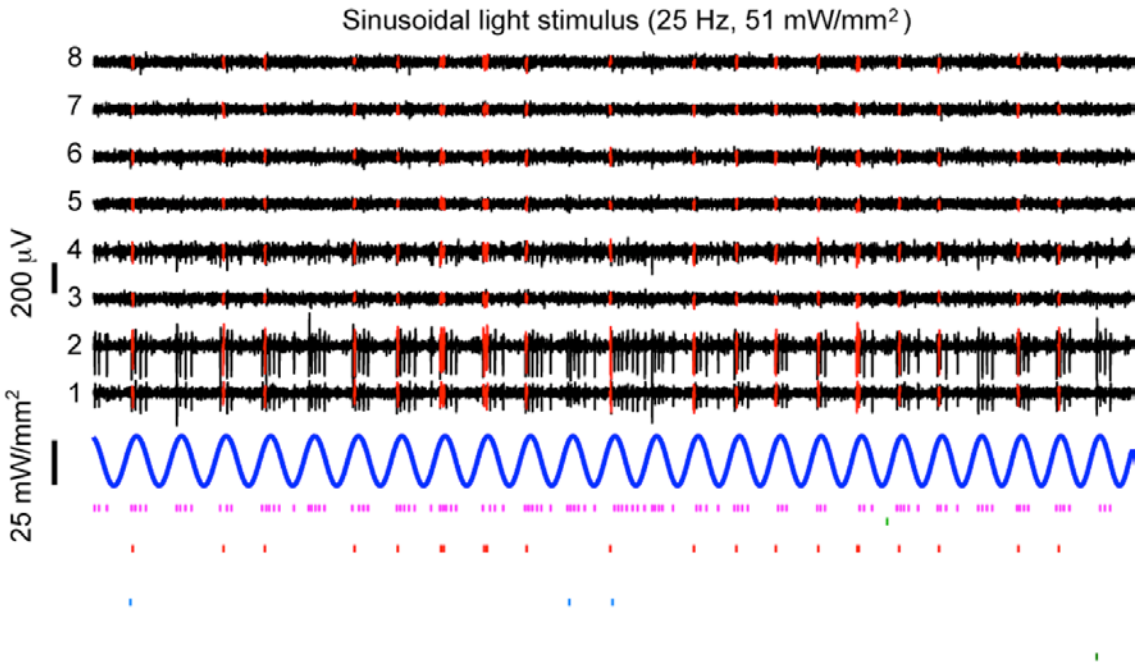

Figure 3.7: Spiking activity recorded during a 25 Hz sinusoidal optical stimulation pattern. Two distinct single units (pink and red) spiked robustly following the optical stimulation cycles.

To quantify the temporal relations between light stimulation and single-unit spiking as well as the influence on extracellular spike waveforms, we also used square light pulses at weaker intensities (40 µW, corresponding to 17 mW/mm^2 at the shank center). The first (red) unit described above tended to spike following most light pulses (71%) at short latencies (median latency, 4 ms), suggesting a direct light effect (**Figure 3.8**, top). In contrast, the second (pink) fired only following some light pulses (31%) and at longer latencies (center of mass, 41 ms), suggesting a network-driven effect (**Figure 3.8**, bottom). For both cells, the spontaneous and light-induced waveforms were indistinguishable (correlation coefficient >0.99). Thus, the monolithic silicon waveguide/recording platform enables monitoring and control of multiple single-units in dense brain structures *in-vivo*.

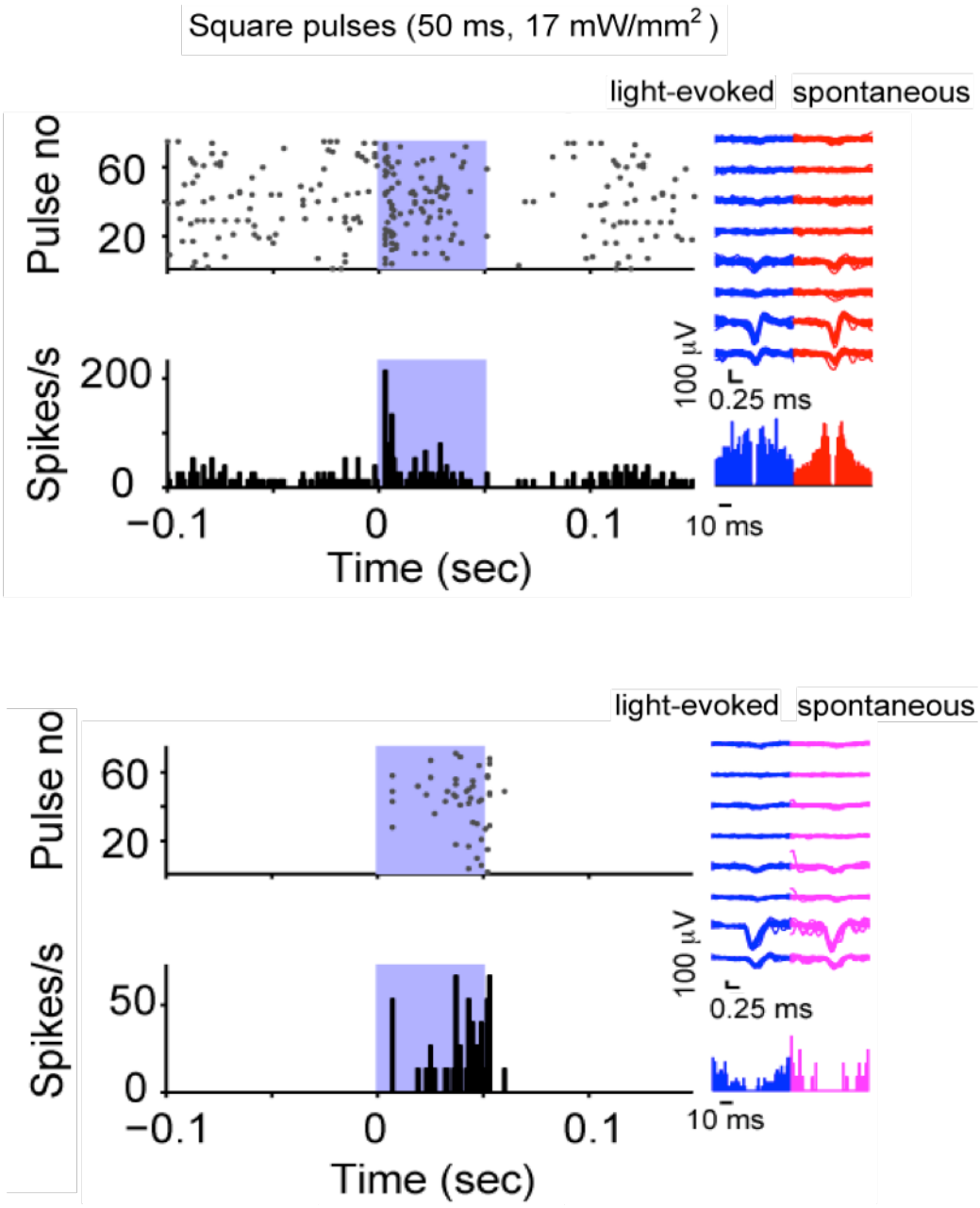

Figure 3.8: Optical stimulation with square pulse waveforms (50 ms, 40 µW max power) showing distinct temporal relations between the light stimulus and spiking of the two units: red (top) and pink (bottom), which were identified in **Figure 3.7**.

3.6. Discussion

In 2005, the first neuron firing a precise action potential in response to blue light stimulation was demonstrated[19]. Although many investigators have realized the

unparalleled advantages that optical stimulation of neurons had offered as compared to the conventional electric stimulation, only few laboratories had the capability to couple optogenetics with extracellular recordings for *in-vivo* neuroscience research due to the lack of reliable optical stimulation probes.

In this study, a new probe with monolithically integrated optical waveguides and recording electrodes was designed. The key innovations of this work are in the precise geometric definition of all electrical and optical components as well as the overall miniaturization of probe dimensions for biocompatibility and scalability. The recording electrodes and the optical stimulation sites can be custom-designed into any configuration to target a specific application. For simple validation experiments *in vivo,* a single-shank probe with 8 recording electrodes and 1 waveguide was used. The electrode array has been carefully designed in terms of recording site area, pitch and total recording span, in order to maximize the probability to record from single-unit potentials given the anatomy of the hippocampus CA1 region. Because the stimulation site was positioned very close to the recording sites (60 μm from the closest), only a small amount of light (<20 mW/mm^2) was required to illuminate all the neurons being monitored by the electrode array, thus preventing spike superposition and LFP offset which can be the result of strong photo-induced currents[91]. Yet the current design also enables emitting higher light intensities, on the order that may be required to target large neuronal populations and influence certain behaviors[14], [99]. The shank dimensions were also reduced to the bare minimum to avoid displacing large volume of tissue during implantation. This is critical especially for scaling towards simultaneous

stimulation and recording from large number of neurons with multiple probe shanks without serious insertion damage or increased foreign body reactions.

One of the biggest challenges of this technology was to obtain high optical transmission efficiency from the optical fiber to the stimulation site via the integrated waveguide. The dielectric waveguide was more appropriate than SU-8 waveguides for applications that involve the stimulation of ChR2 expressed neurons since absorption loss of SU-8 is very high near 473 nm[94], [102], [103]. In addition, SU-8 absorption of water is well known and could significantly affect long-term optical property of the waveguide[98]. The two drawbacks of the dielectric waveguide were the surface roughness created during plasma etching of the waveguide sidewall and the limitation of waveguide thickness constrained by the fabrication equipments (up to 5 μm) such as deposition and etching tools. The surface roughness can lead to propagation loss through the waveguide surface but has been alleviated by optimizing the lithography and plasma etching conditions to create smooth sidewalls as shown in **Figure 3.4**(c). Because it was difficult to fabricate thick dielectric layers due to stress and extended plasma etching time, a thin waveguide limited the ability to match the mode-shape between the large multi-mode optical fiber core and the smaller waveguide. This resulted in relatively large coupling loss at the fiber-waveguide junction. To reduce coupling loss, the width of the waveguide at the fiber junction was doubled from 14 μm to 28 μm, which allowed the waveguide to overlap 7.13% of the total cross-sectional area of the 50-μm-diameter optical fiber core. In previous report[93], very low coupling loss (0.4 ± 0.3 dB) was achieved due to their fabrication capability of depositing very thick (9 μm) dielectric waveguide core, which matched closely with the cross-sectional area of their single-

mode optical fiber with 8 μm in diameter. In this work, it is also possible to achieve a higher coupling efficiency if a single-mode fiber (3-μm-core-diameter; 460HP, Thorlabs, Newton, NJ) were used to couple to the oxynitride waveguide (5-μm-thick). However, the single-mode fiber suffers more than 60% loss in comparison to the multi-mode fiber when coupled to the laser source. Therefore, in order to maximize the output power at the end of the waveguide, it was more appropriate to use multi-mode fiber despite larger coupling loss to the waveguide. Nonetheless, in this work the total loss through the entire assembly has been measured to be 10.5 ± 1.9 dB, which is comparable to recent report using SU-8 (> 12.4 dB) with significantly larger cross-sectional area (150 μm ×150 μm)[94]. Besides reducing insertion damage, another advantage of the small waveguide aperture is the confinement of high optical intensity (9400 mW/mm^2) into a small region (14 μm × 5 μm) with minimal input power (7 mW from optical fiber). This not only provides stimulation with high spatial resolution but also minimizes electromagnetic interference from the optical stimulation site to the recording channels.

When coupled to the yellow (593 nm) laser, the overall transmission loss was roughly 7.45 dB, which included coupling and propagation losses through the waveguide. The overall efficiency (18%) was higher than the cross-sectional area ratio after application of index-matching epoxy at the fiber/waveguide junction, which helped convergence of skew rays towards the waveguide and reduction of reflective loss at the waveguide interface. Previous studies have achieved coupling efficiencies at around twice the ratio of the fiber core area to the waveguide cross-sectional areas[92]. The lithographically-defined waveguide and fiber groove have allowed precise self-alignment to obtain a coupling efficiency close to the theoretical value (more than twice

the fiber-to-waveguide cross-sectional area ratio), given the current waveguide design. Because the coupling loss dominated the total transmission loss at 593 nm (total measured transmission efficiency was close to the maximum theoretical coupling efficiency), it can be deduced that the propagation loss through the oxynitride waveguide at 593 nm was negligible. However, a dramatic increase in propagation loss was observed as the wavelength of the coupled light sources reduced. The measurements have indicated that the efficiency of yellow (593 nm) light was roughly two times that of the blue (473 nm) light and at least three times that of the violet (405 nm) light. For applications involving excitation of ChR2 expressed neurons, it is sometimes advantageous to use violet (405 nm) rather than blue (473 nm) light source because of lower source cost, smaller spatial spread, and greater spectral separation from the longer wavelengths that could be used to activate other types of opsins[17]. From the preliminary results, it can be estimated that the transmission efficiency of violet light by the dielectric waveguide is roughly 67% of the blue light. In addition, the sensitivity of ChR2 to violet versus blue is approximately 60%[22]. The maximum output power of the probe for this *in-vivo* experiment was 1.1 mW when connected to a 17 mW blue laser source. Therefore, since the effective stimulation power of the violet light was around 40% of the blue light, it would still be more than enough to excite ChR2 as we have shown robust photo-induced spiking in response to 40 μW stimulation power.

The acute *in-vivo* experiment demonstrated the feasibility of the monolithically integrated optical stimulation probe by recording single-unit activity in response to a variety of optical stimulation patterns in the rat hippocampus CA1 region. However, concurrent local field potential (LFP) analysis (in addition to spike detection) was not

possible during optical stimulation because it was necessary to filter out the low frequency light artifact, which also removes other low-frequency features of the LFP.

The light artifact was mainly caused by a large amount of light (>80%) leaking at the fiber-waveguide junction, which was only 1 mm away from the nearest wire bond (rather than photons hitting the recording sites). In a simple modification to the current design, the bonding pads would be moved farther away from the fiber-waveguide junction, allowing sufficient amount of opaque epoxy to be applied on the pads, thus blocking the electrical signal lines from the leaked light.

In the future, the number of recording channels and optical stimulation sites can be scaled up without compromising the intrinsic advantages of the monolithic integration technology. Flexibility of design alternatives can be introduced in waveguide structures, such as implementing an optical mixer configuration to deliver different wavelengths from multiple light sources to the same stimulation site[96]. Recent work[92] demonstrated the advantages of directly integrating multiple light sources, such as light emitting diodes (LED) or laser diodes (LD), on the animal head stage to enable free animal movement while minimizing mechanical damage to the implanted probe by removing tethered optical fibers altogether. Combining this assembly technology with the monolithically integrated waveguide probe design can be the next step towards applications involving chronic large-scale extra-cellular recordings and optical stimulation in behaving animals. Although challenging, as there will be two optical coupling junctions (LED or LD to fiber and fiber to waveguide), the high transmission efficiency from fiber to waveguide obtained in this work (~ 9%) is likely to suffice given the previously reported 5% transmission efficiency from LD to fiber[92].

Even without any modifications to the present probe, commercially-available 10 mW LD will deliver ~45 μW at the tip of the waveguide, similar to the power used to activate single-units in the current study. Therefore, the monolithically integrated optical probe, having precisely defined geometries through lithography, high optical transmission efficiency obtained by enhanced fabrication/packaging technologies, and the flexibility for alternative configurations as well as scaling, can bring optogenetics to its full *in-vivo* potential.

CHAPTER 4

MONOLITHIC INTEGRATION OF μLEDS ONTO PROBE SHANK

4.1. Motivation towards designing a "dream probe"

The successful fabrication and *in vivo* testing of the single-shank probe with monolithically integrated waveguide described in Chapter 3 generated tremendous excitement to the engineering group. Although it was a significant leap in technical achievement[104], the single-shank, single waveguide probe was far from being useful for practical neuroscience studies. The key challenge was scaling of the number of sites both in recording and stimulation, while keeping the entire system, including packaging, in its minimal volume and weight. This was especially critical for Buzsaki group's research, that is primarily focused in the CA1 region of the hippocampus to study spatial memory and navigation in behaving animals. To target the CA1 pyramidal layer in mice, which is only roughly 50-μm-thick or 4-6 cell layers across, high-density electrodes and multiple optical stimulation sites are needed to study the densely populated region. This sets a limitation on the depth span of the probe tip that would be useful to interact with the CA1 pyramidal layer, and therefore also the number of active components (electrodes/optics) within that span. Clearly, the size of the active components must be reduced while maintaining reasonable light output intensity, electrode impedance, etc. (which scale unfavorably as size reduces), in order to simultaneously interact with

multiple cells in this tiny neural structure. In addition, because the most practical animal subjects are behaving mice, weighing only 25-40 g, the total weight of the implanted device including headstage and cables should be no more than 10% of the mouse's body weight. All of the tethering cables/connectors should neither restrict the animal movement nor transmit mechanical force down to the probe shanks, either when the animals are moving or when cables are plugged in/out of the headstage. The previous design from Chapter 3 relied on guiding light through one external optical fiber per stimulation site. The tethered fiber was too bulky for a behaving mouse, so that it was only suitable for larger animals such as rats, or for acute experiments using anesthetized animals. Having acknowledged the limitations of the previous design, the new goal statement was *to design the next generation "dream probe" with scalable quantity and resolution of integrated active components to enable neuroscience studies at the cellular level neural circuitry in behaving animals*.

4.2. Initial approach and other published works

At the very beginning of the design stage, the most important objective was to eliminate the bulky optical fiber because it was a non-scalable approach. An intuitive advance from the previous design was to use external laser diodes or LEDs to couple light into the integrated waveguides. The rationale was that these semiconductor optical devices require only electrical wires instead of optical fibers to deliver the light; and that these wires can be made extremely lightweight and flexible. Potentially, these light-emitting devices can also be powered wirelessly to eliminate the mechanical tethering to the animal headstage completely. **Figure 4.1** illustrates the concept of coupling an

external LED array to the neural probes with integrated waveguides. The LEDs can be purchased from vendors (Cree Inc., Durham, NC) with the smallest emission area of roughly 250μm × 250μm. However, even in these dimensions, the Lambertian emission profile of the LEDs cannot be efficiently coupled into the integrated waveguides having a cross-sectional dimension in the order of 20μm × 15μm. Despite considering approaches such as using intermediate tapered fibers to couple light between the LED and the waveguide, the light cannot be effectively converged towards the waveguide as restricted by the conservation of Etendue[105], resulting in significant coupling loss. A more power efficient approach is to use laser diode, which has a much more confined emission. Currently, chip-level laser diode chips are rare and expensive, especially at around the 470 nm wavelength range (ideal for the activation of ChR2). In all cases, the LED and diode coupling approaches require significant engineering as well as highly accurate manual assembly to address the coupling challenges, which drive up the cost and production time while decreasing yield and scalability. Lastly, the number of waveguides-per-shank and the shank pitch were severely limited by the pitch of the LED linear array as clearly illustrated in **Figure 4.1**.

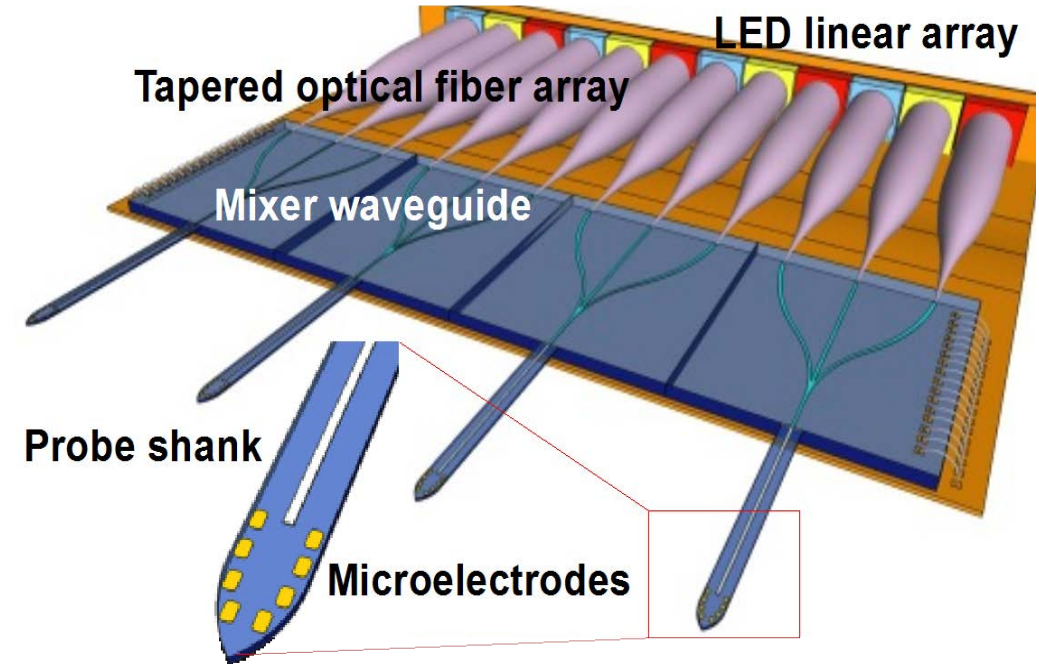

Figure 4.1: 3-D illustration of the first concept to scale up the number of optical stimulation sites by coupling LED array to the integrated waveguides.

Concurrent with the development of the new approach that will be described in the majority of this Chapter, a few other academic groups have attempted to integrate LEDs onto the probe shank that would allow increased numbers of stimulating sites on a probe shank without optical fiber connections. One approach was hybrid integration: manually assembling the microfabricated LEDs onto a flexible platform[106]. Although the individual LEDs could be made relatively small (50μm x 50μm) using a laser lift-off technique, the hybrid assembly gave a large probe shank width of over 400μm. This probe substrate is too wide to study delicate brain regions such as the CA1 layer. In addition, the flexible substrate is incapable of continuous driving in depth after implantation, which is essential to locate the optimal recording position in the CA1 layer. In Kim et al., the GaN LED active layer was removed from the sapphire substrate and protected by an adjacent polymer film attached using epoxy[106], [107]. Water and ion

permeability in the organic layers may limit longevity and reliability and may increase parasitic capacitance, thereby compromising the signal-to-noise ratio[108]–[111]. Another group proposed using the mature technology of fabricating GaN LEDs on sapphire to create LED-on-sapphire probes[112]. Although the thermal and optical characterizations of these μLEDs with diameters of 40μm have been reported, no probe shank was defined and no recording electrodes were integrated. The same report suggested that the probe shape can be patterned by laser dicing and that the substrate can be thinned mechanically, but it would be extremely difficult to etch the sapphire substrate reliably into a desired probe shape and produce a sharp needle-like structure, which again is crucial for probing small brain regions such as hippocampus.

4.3. Monolithic integration of μLEDs onto silicon probe shanks

The final goal of this dissertation is to design the "dream" probe targeting optogenetic applications that require high spatiotemporal resolution for interactions with multiple single-units in behaving animals. After numerous communications with collaborators (Dr. Stark and Prof. Buszaki), the specifications for the next generation optoelectrode can be summarized as following:

1. Overall shank dimensions (5-mm-long, 70-μm-wide, 30-μm-thick) and recording electrode array configuration (number, size and pitch, material) should be kept the same as the single-shanked probe described in Chapter 2, as it was proven to record single-unit activities in the CA1 region.
2. The number of shanks should be increased to at least four to cover the lateral recording span.

3. The number of optical stimulation sites should be maximized given the shank dimension, with the emission area similar to that of one recording electrode (or the soma of a neuron) to achieve subcellular stimulation resolution.
4. The entire assembly must be minimal in size and weight no more than 3-4 g (~10% of a mouse's average body weight).

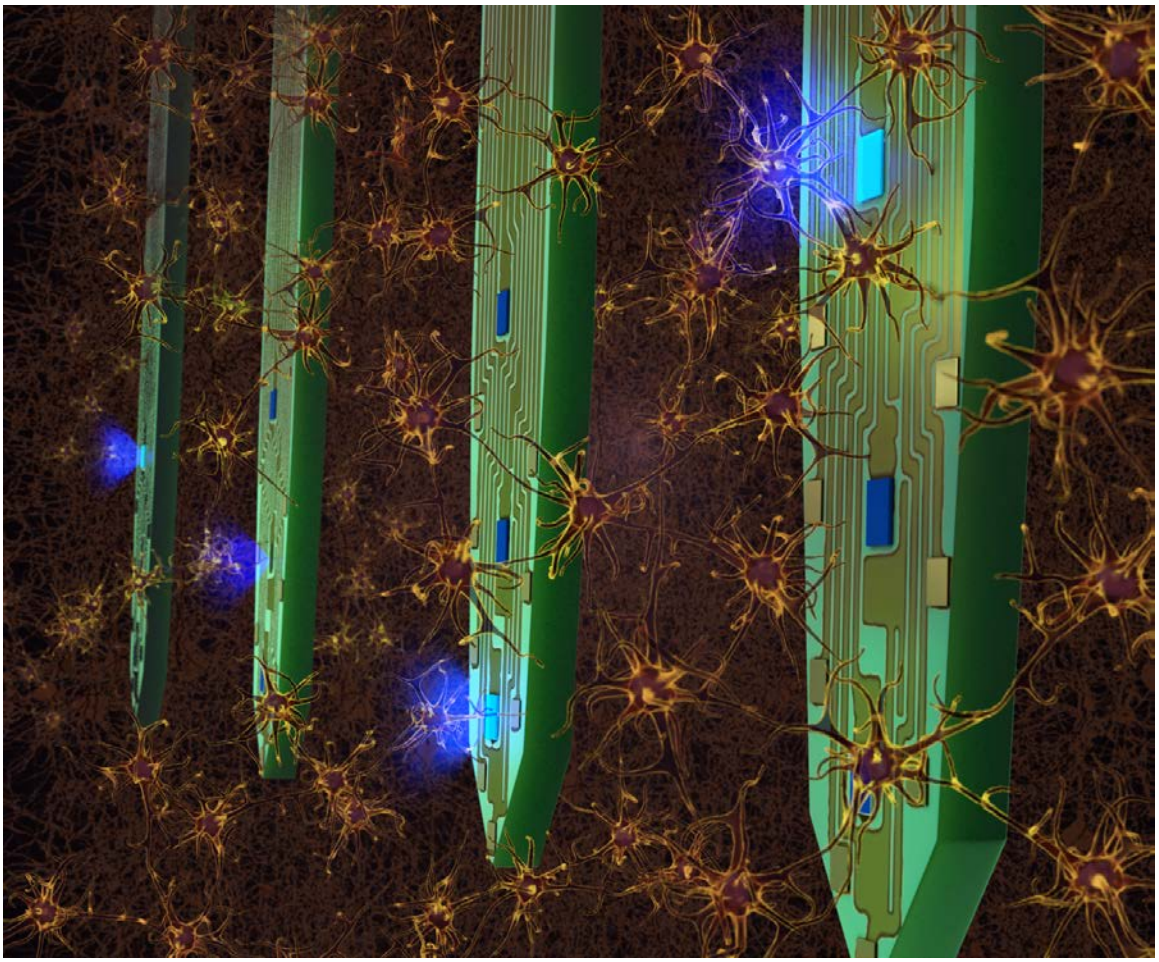

Figure 4.2: 3-D schematics of proposed 4-shank neural probe with monolithically integrated 32 recording electrodes (gold) and 12 μLEDs (blue).

While the natural approach to couple diodes to the previously designed waveguide probes seemed to have limited potentials, other alternative techniques to integrate LEDs onto the probe shanks could not meet our specifications[106], [112].

However, it was clear that the direct integration of light sources onto the probe shanks was necessary because of the quantity and resolution of the optical stimulation sites it can achieve; the question was only how. Finally, a completely novel modification to the Michigan probe has been devised as illustrated in **Figure 4.2**, *monolithically integrating 3 μLEDs and 8 recording electrodes onto each of the 4 silicon shanks*. This new design offered several significant advantages over the integrated waveguide approach described in Chapter 3. Firstly, the μLED power supply can be wired to external electronics with flexible cables, which helped to enhance animal mobility because of the reduced assembly size, weight and rigidity. Furthermore, it can be easily wirelessly controlled, even in small animals[106]. Secondly, the μLED size can be arbitrarily designed for any specific application. For the initial prototype, the μLEDs were designed with 15μm × 10μm emission area (which can be tailored into different sizes for other applications), similar to the size of a typical neuronal soma. This is an important advancement over all the previous optical probe designs because it even holds promise to stimulate with a spatial resolution to target a specific subcellular structure (e.g., soma, dendrite, axon, etc.). Thirdly, because of the small electrical interconnection line width required to power the μLEDs (~2-5 μm) as compared to the width of our previously designed integrated waveguides (~ 15 μm), it was possible to fit 3 μLEDs onto the same probe shank with dimensions necessary to contain a single waveguide. Having a total of 12 μLEDs distributed across 4 probe shanks, there are 12! (480 million) possible stimulation sequences that can be programmed to manipulate the spike timing at these 12 different locations. This will allow highly versatile manipulation of high-resolution neural circuits, which is critical to study memory formation/consolidation by stimulating

very specific parts of the hippocampus where synaptic junctions are highly plastic[113], [114].

4.4. LED-on-Si technology

To specifically design μLEDs that can be monolithically integrated onto the probe shank, the μLED materials and architecture must be carefully selected, which would determine the emission wavelength(s), substrate choice, theoretical efficiencies and process compatibility[115], [116]. The simplest form of LEDs is a p-n junction where electrons and holes are injected into an active region where they recombine to form photons[115]. Multiple quantum well (MQW) structures have been engineered at the active region of LED junctions to enhance radiative recombination (i.e., to effectively produce photons rather than generating heat)[117]–[119]. The emission wavelength of the active region is determined by the bandgap energy of the small bandgap material in the quantum well[120] (**Figure 4.3**(a)). InGaN/GaN MQW is most attractive for optogenetic applications because, by tuning the InN to GaN ratio, the MQW emission wavelength can be tailored across a wide range within the visible spectrum[121], suitable for activating commonly used opsins such as ChR2 (blue), Archaerhodopsins (green and yellow), and Halorhodopsin (green, yellow, and red), as shown in **Figure 4.3**(b).

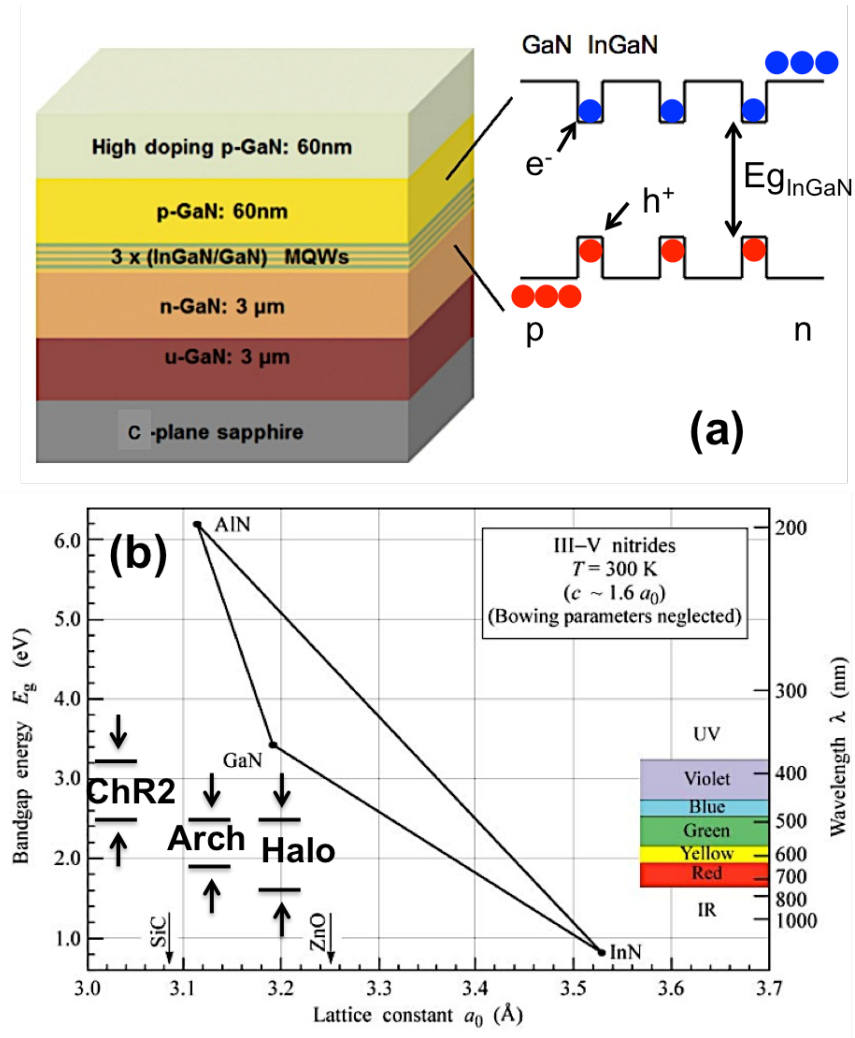

Figure 4.3: (a) Cross-sectional view of LED structure showing MQWs (intrinsic) between p-type semiconductor and n-type semiconductor, all grown on top of a substrate (sapphire)[120]; (b) Chart showing bandgap and wavelength tuning by varying the composition of the MQW materials.

A significant challenge in fabrication of GaN-based devices is that GaN wafers do not exist, so that GaN must be deposited on a substrate with different material composition having significantly different atomic lattice structure[122]–[124]. As a result, the deposited GaN is stressed when forced to bond with the different atomic arrangement of the substrate material, which leads to dislocations and other forms of defects as shown in **Figure 4.4**. These defects can propagate from the interface and

become detrimental for high efficiency optoelectronic devices. Typically, GaN-based LEDs are fabricated on top of sapphire or SiC substrates where lattice mismatch is most acceptable[125]. McAlinden, et al. has reported that miniaturized LEDs fabricated on sapphire substrates have the potential to be used for optogenetic probes, after a detailed analysis of the LED efficiencies and thermal budget[112]. However, sapphire is impractical as a substrate for neural probe fabrication because it is extremely difficult (or almost impossible) to etch sapphire into a desirable, needle-like structure to penetrate into the brain tissue without detrimental tissue damage.

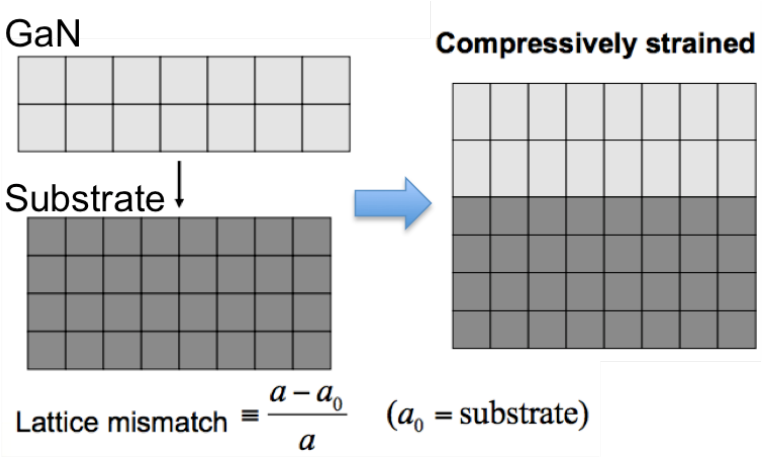

Figure 4.4: Lattice mismatch between two crystalline semiconductors resulting in strained film deposition.

Recently, growth of GaN on Si (111) technology has shown tremendous progress by introducing buffer lattice matching layers to reduce the interface defects[126]–[130]. Significant progress in this area to further optimize the interface between GaN and Si are being made with the primary goal of reducing LED costs with large-scale Si wafer processing[126]. Currently, customized GaN films on Si wafers are commercially available (NovaGaN, Kyma, etc.). The wafers used for the work described in this Chapter were purchased from NovaGaN with the customized specifications given in

Figure 4.5. Silicon substrate is ideal for neural probe fabrication because well-established micromachining techniques can accurately define the silicon probe shape by either dissolved wafer process[11], [47], [48] or DRIE approach[96], [104], [131]. Silicon also has approximately 5 times higher thermal conductivity than sapphire, allowing more effective dissipation of heat generated by the LEDs[132]. In addition, having an opaque silicon substrate helps to confine light emission only from the top side of the LED, as opposed to LEDs-on-sapphire, which can emit light isotropically even through the transparent substrate. This could be advantageous for large-volume illumination, but it is certainly undesirable for high-resolution stimulation of a local neural circuit, which is the target application of this work. Despite obvious advantages of fabricating LEDs on silicon, there is one significant drawback of this approach: The interface defect density of GaN grown on silicon substrate is still roughly 10 times greater than that grown on sapphire[126]. As a result, LED efficiency is expected to be lower. Section 4.6. will discuss in detail about how this efficiency deficit is manageable based on modeling and theoretical calculations.

12		GaN:Mg			100.0 ± 10	$p = 5e^{17}\ cm^{-3}$
11		AlGaN:Mg		25%	20.0 ± 3	$p = 5e^{17}\ cm^{-3}$
10	5x	GaN			12.0 ± 1	
9	5x	InGaN	14%		2.5 ± 0.25	
8		GaN:Si			580.0 ± 30	$n = 3e^{18}\ cm^{-3}$
7		GaN/AlN Supperlatice			60.0 ± 6	nid
6		GaN			380.0 ± 20	nid
5		GaN/AlN Supperlatice			60.0 ± 6	nid
4		GaN			380.0 ± 20	nid
3		GaN/AlN Supperlatice			60.0 ± 6	nid
2		GaN			380.0 ± 20	nid
1		AlN		100%	60.0 ± 6	nid
0		Silicon HR Ø = 2 inch. CMP Backside			500 µm	

Figure 4.5: Specifications of the GaN-on-Si wafers purchased from NovaGAN.

4.5. Fabrication process

The fabrication process is illustrated in **Figure 4.6**. Briefly, the process began with the commercially available Si (111) wafer with quantum-well epitaxial layers (NovaGaN). The GaN/InGaN quantum wells were tailored to have an emission spectrum centered at 440 nm for the activation of ChR2 expressed neurons. The epitaxial layers were etched down to expose n-GaN, forming an isolated LED mesa structure. Then, 500-nm-thick PECVD oxide was deposited to insulate the mesa sidewalls. Using the same photoresist mask, the oxide was wet etched to open a contact to p-GaN, and a semi-transparent Ni/Au (5nm/5nm) layer was patterned by liftoff to form an ohmic contact to the p-GaN. Later, a separate mask was used to open a contact to the n-GaN layer. Next, a Ti/Al/Ti/Au (50/300/50/100 nm) layer was patterned to form the electrical interconnection lines for recording channels as well as for powering the LEDs. The bottom Ti layer served as the adhesion layer with a proper work function to form ohmic contact with n-GaN. The multiple metal stack was selected because of its thermal stability and enhanced resistance to both interlayer diffusion and surface oxidation[133]. At this stage, the LED fabrication was complete and was available for characterization using a probe station. Post-LED fabrication began with etching of the GaN layer in the field region (outside of the probe shank) completely to expose the GaN sidewalls and the underlying silicon substrate. Double layer of dielectrics (30-nm-thick Al_2O_3 by atomic layer deposition (ALD) and 500-nm-oxide by PECVD) was then deposited to insulate the GaN layers. The additional ALD oxide has been shown to significantly reduce the moisture permeability of the insulation layer[134]. The oxide bilayer was then etched to open the contact at the recording sites and Ti/Ir was sputtered over the contacts to form

the recording electrodes. Finally, the silicon substrate was etched from top as well as from bottom, using a double DRIE process to release the probes from the wafer.

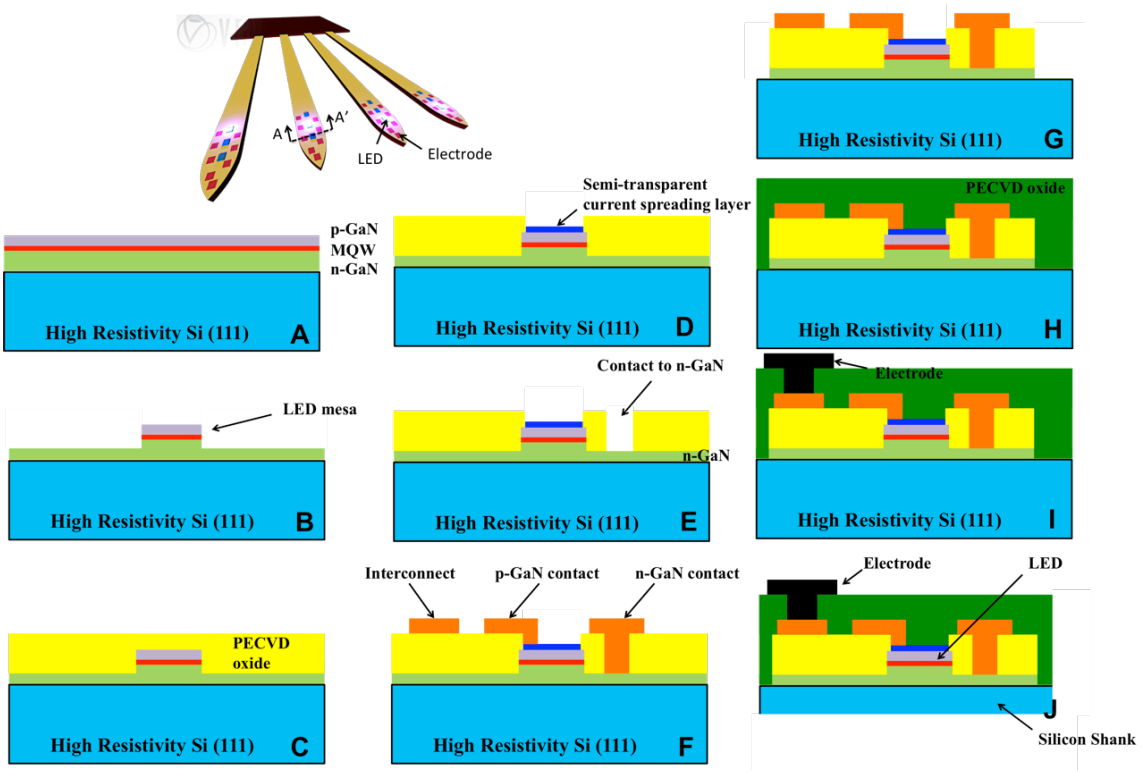

Figure 4.6: Fabrication processes of LED-integrated probes, showing cross-section through A-A': (a) starting wafer with epitaxial LED layers grown on <111> silicon wafer; (b) plasma etching of GaN to form LED mesa; (c) deposition of PECVD oxide; (d) patterning current spreading layer; (e) plasma etching of oxide to expose n-GaN; (f) patterning of Ti/Al/Ti/Au for interconnection lines; (g) plasma etching of field GaN; (h) deposition of PECVD oxide for complete insulation of LEDs; (i) etching oxide to form electrical contact and patterning of Ti/Ir to form recording electrodes; (j) front and back DRIE processes to define probe shank dimensions and release probes from wafer.

Figure 4.7 shows the fabricated devices with high magnification at the probe tip to highlight some of the key fabrication steps. In **Figure 4.7**(a), the μLED mesa has been etched and the Ni/Au current spreading layer can be seen as a slightly smaller rectangular region inside the mesa. The current spreading layer must be carefully engineered to produce a low resistance ohmic contact to p-GaN[133]. In addition, the layer must be transparent to the emission wavelength. The Ni/Au (5nm/5nm) layers

create a reasonable ohmic contact to p-GaN with contact resistance of 10^{-5} Ω-cm and have 75% transparency to blue light (460 nm). This was significantly better than using Indium Tin Oxide (ITO) deposited from the Lurie Nanofabrication Facility, which had roughly 4 magnitudes higher contact resistance. The poor ITO ohmic contact would raise the turn-on voltage of the μLEDs from 2.8V to over 10V. The n-contacts were defined close to the mesa to minimize series resistance through n-GaN, while taking into consideration of the alignment margin and routing of the interconnects. The GaN defects were clearly observable as black dots in this image, which were present both in n-GaN region and on top of the mesa. These defects existed on the starting wafer due to the lattice mismatch between GaN and silicon. **Figure 4.7**(b) shows the interconnection lines patterned by liftoff using projection lithography. The line width and spacing were 2 μm each for the recording channels, while the line width for the LED power lines was 5 μm to reduce the resistance, which was roughly 100Ω for the 5-mm-long metal interconnect. This process step was very critical due to the density and length of the interconnects: any defect would cause open circuit to a channel. It was necessary to avoid contact lithography because of the intrinsic tensile stress of the GaN-on-Si wafer (~100 MPa), which causes ~15 μm wafer bow (wafer diameter = 2 inch). This resulted in poor contact between the mask and the wafer, which led to diffraction through multiple "slits" from the mask pattern and inability to resolve 2-μm-features. Using projection lithography instead, this problem was effectively circumvented. In **Figure 4.7**(c), the field GaN was removed completely by dry etching. The photoresist here must be sufficiently thick (> 8 μm) to withstand the poor selectivity through Cl_2/BCl_3 plasma etch for the ~2-μm-thick GaN/AlN (n-GaN and buffer layers). Etching through the

alternating stacks of GaN/AlN showed distinctive colors, typically a mixture between red, green and blue. This was an easy visual aid to control the etch timing so that the silicon substrate, which was clearly grey in color, would not be roughened undesirably by plasma over-etching. In **Figure 4.7**(d), the Ir electrodes were patterned, which had impedance of ~ 1MΩ at 1 kHz with an area of 143 μm^2. In **Figure 4.7**(e), a narrow, 10-μm-wide trench surrounding the probe perimeter was etched using DRIE. The trench depth was 30 μm, which defined the shank thickness. This etch depth was conservatively chosen because of the lack of an etch stop in SOI wafers such as the work described in Chapter 3. A thinner shank would be more preferable for reducing the tissue damage during probe insertion, but would be more difficult to control the final backside etching process, which could significantly lower the yield of released shanks. It was also critical to define only a narrow trench around the probe, instead of etching the field region entirely. Having minimal amount of Si removed in this step greatly helped the uniformity of the backside Si etch in the next step for two reasons: 1) the reactive ions inside the plasma is being consumed during Si etch, and therefore the plasma density depended on the amount of Si present; 2) the heat generated during the etching process conducts through the Si substrate, which also depends on the amount of Si present. Therefore, preserving most of the Si substrate would generate least variation in thermal conductivity and plasma density during the backside etching process, and this would result in the most uniform etch rate across the entire wafer. **Figure 4.7**(f) shows the released probe after backside Si etch. The etch uniformity of the backside etch (465-μm-deep) must be less than 5% in order to release all of the probes having thickness of ~ 30μm. With the minimal trench width defined in the front DRIE step and multiple

dummy silicon pieces surrounding the actual device wafer to buffer the etch rate, 100% of the probes from a 2-inch-wafer were successfully released. **Figure 4.8** and **Figure 4.9** show larger scale appearance on the wafer right before release and a released probe, respectively.

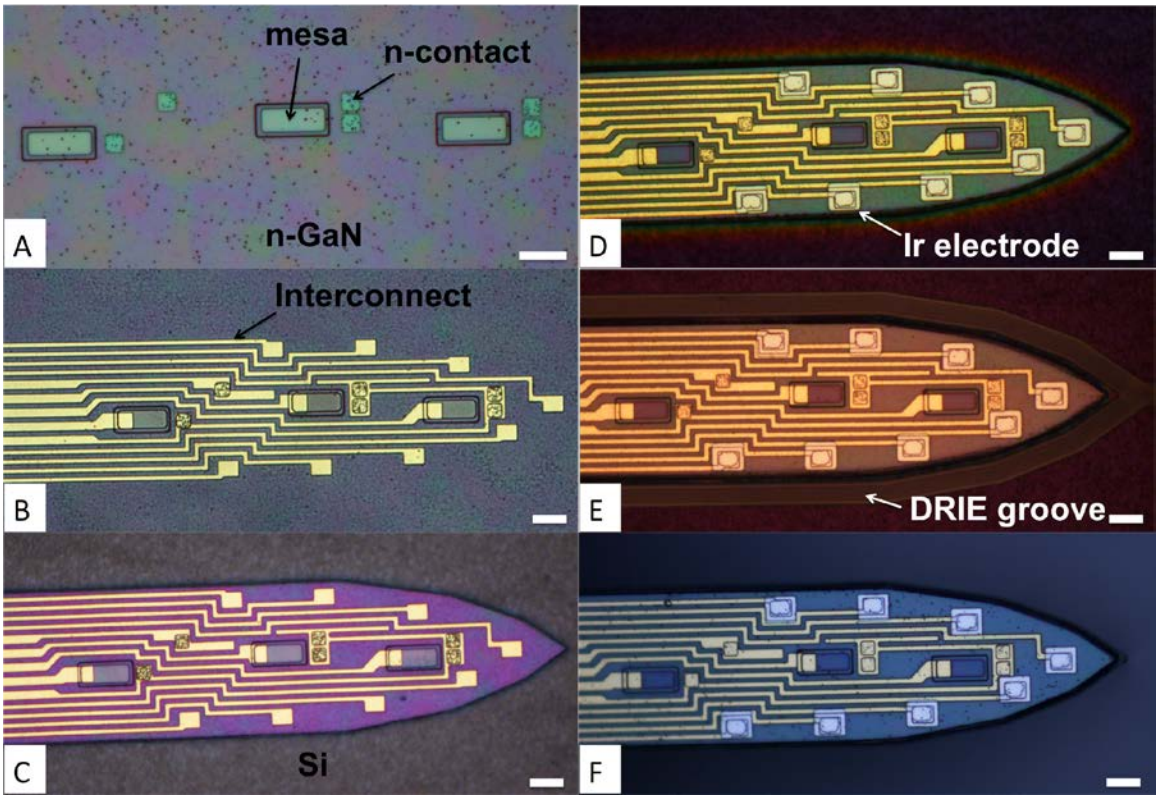

Figure 4.7: The microscope images of the probe tip following several key fabrication steps shown in **Figure 4.6** (all scale bars = 15 μm): (a) LED mesa structure with a stack of MQW, p-GaN and Ni/Au in addition to n-contact opened after step E; (b) liftoff of Ti/Al/Ti/Au forming interconnects; (c) complete etching of GaN in the field region to expose the Si substrate; (d) patterning of Ir electrodes; (e) front DRIE of Si substrate to define probe shank perimeter and (f) after backside Si etching to release the probes from the substrate shown.

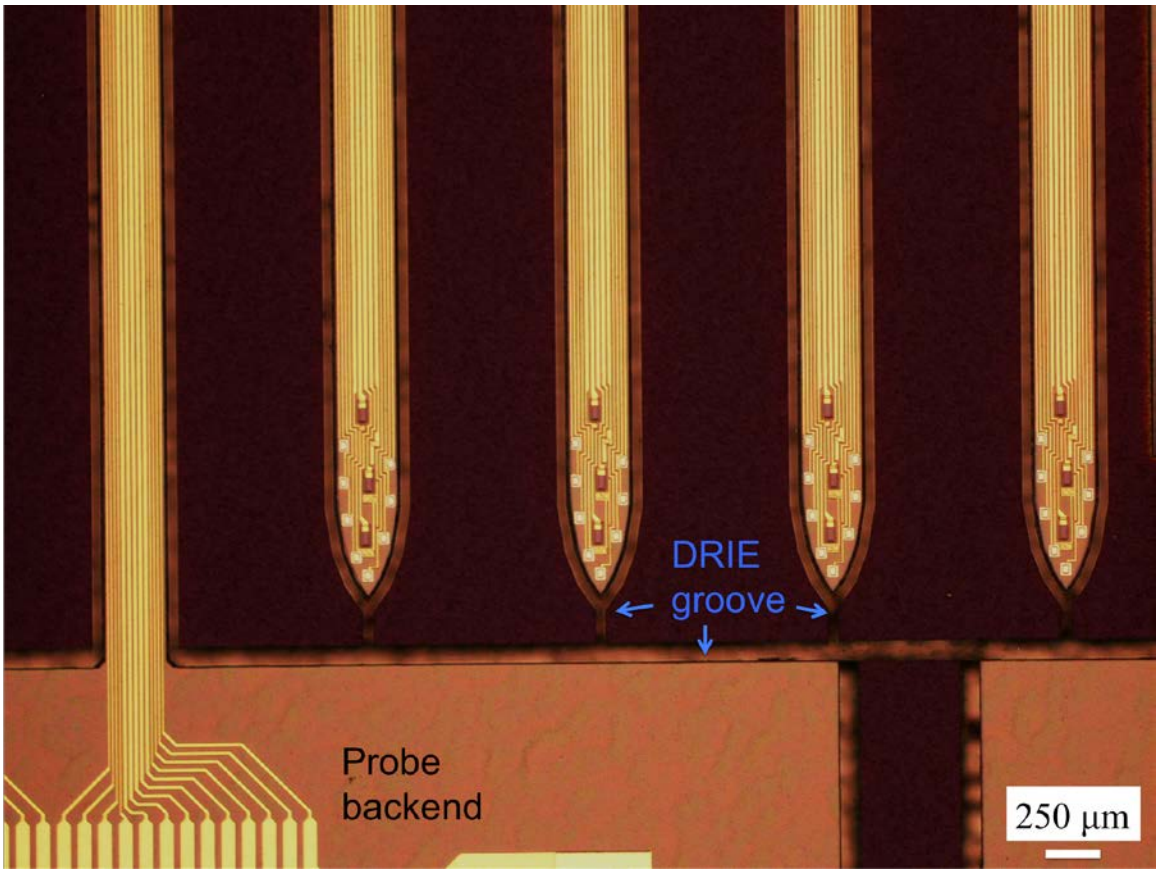

Figure 4.8: Overview of the wafer immediately before the last releasing process with two probes next to each other, showing the backend of probe 1 (left) and the tips of probe 2 (right).

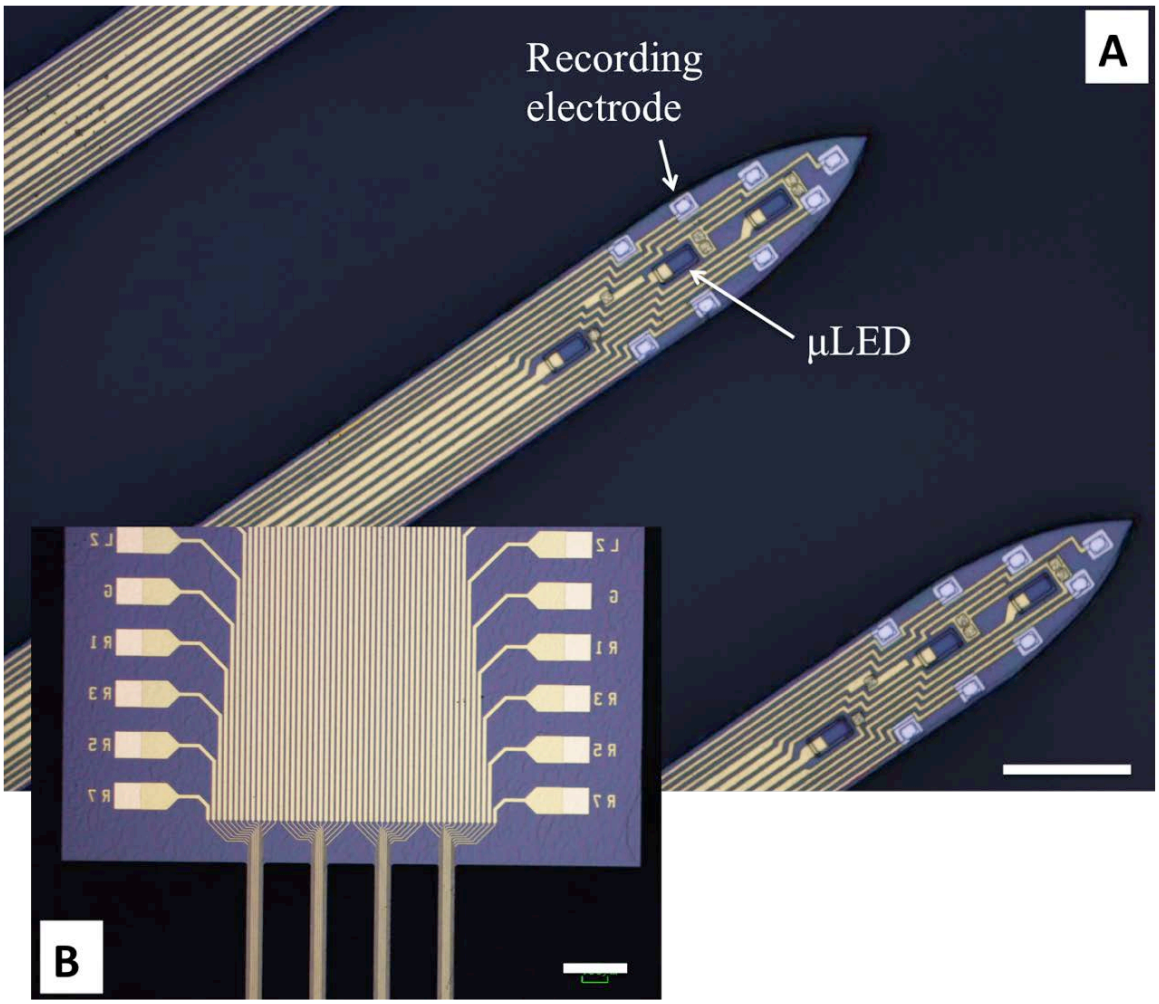

Figure 4.9: Low magnification microscope images of the released 4-shanked probe showing (a) probe tips (scale bar = 70μm) and (b) probe backend for wirebonding (scale bar = 250μm).

SEM images from **Figure 4.10** show further details of the probe structure. **Figure 4.10**(a) illustrates with a tilted view of the probe tip. **Figure 4.10**(b) shows a μLED with the nearby interconnects and contacts. The high contrast between metal and the underlying oxide show that excellent alignment was achieved by the projection lithography required for high-density integration. **Figure 4.10**(c) shows a high magnification image of a mesa structure just after plasma etching. The defects seen as "pits" can be correlated with the "black dots" seen from the light microscope images

shown in **Figure 4.7**(a). These defects are present on top of the mesa (p-GaN) and at the bottom (n-GaN). Clearly, these defects were not the caused by the GaN etch step. In contrast, **Figure 4.10**(d) shows a mesa structure etched by a different plasma condition, composed of only Cl_2 gas instead of a mixture of Cl_2 and BCl_3 as was used for the etching process shown in **Figure 4.10**(c). It was previously reported that the addition of BCl_3 in plasma etching increases the chemical reactivity, and hence is more material selective[135].

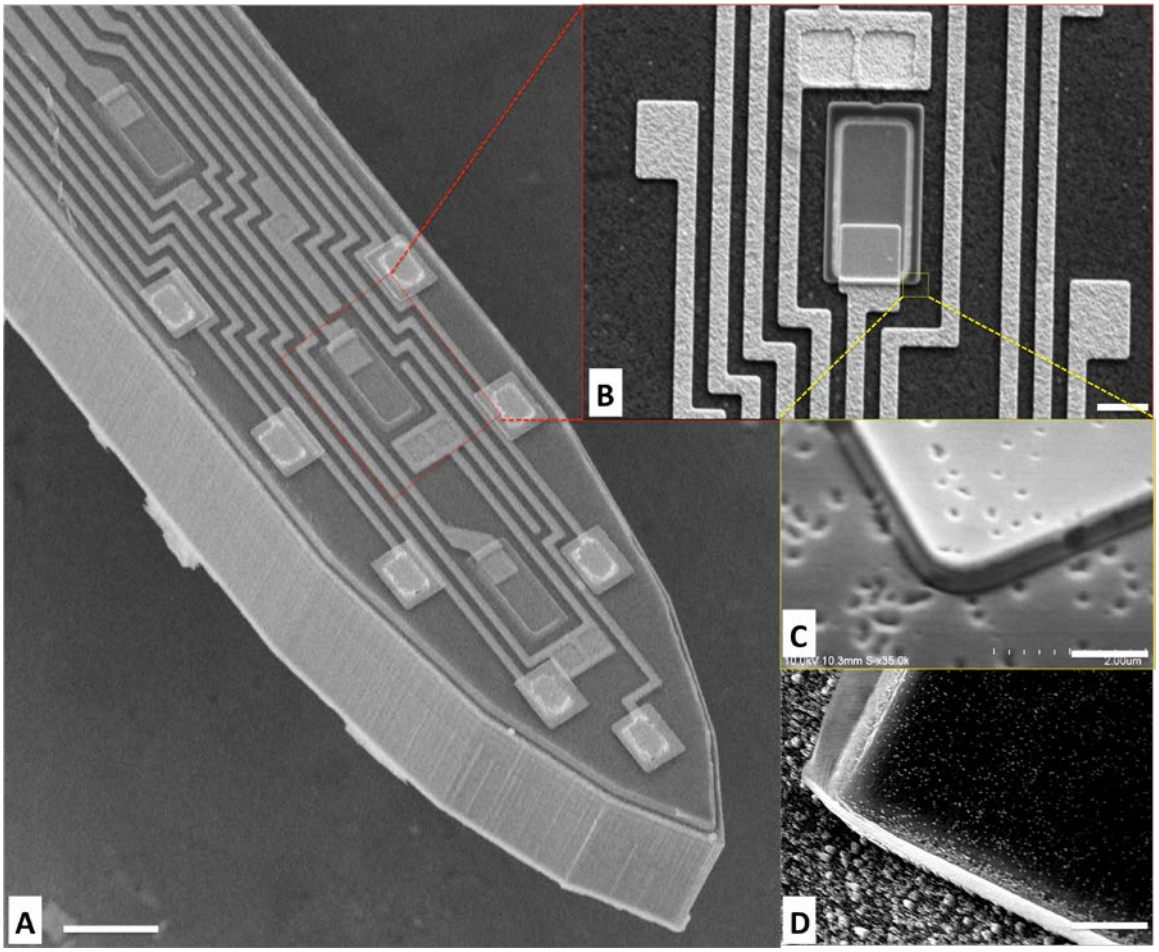

Figure 4.10: SEM images showing (A) released probe at the tip (scaled bar = 35μm); (B) LED and the metal interconnects (scaled bar = 6μm); (C) LED mesa etched with Cl_2/BCl_3 plasma (scaled bar = 1μm); (D) LED mesa etched with Cl_2 plasma (scaled bar = 1μm).

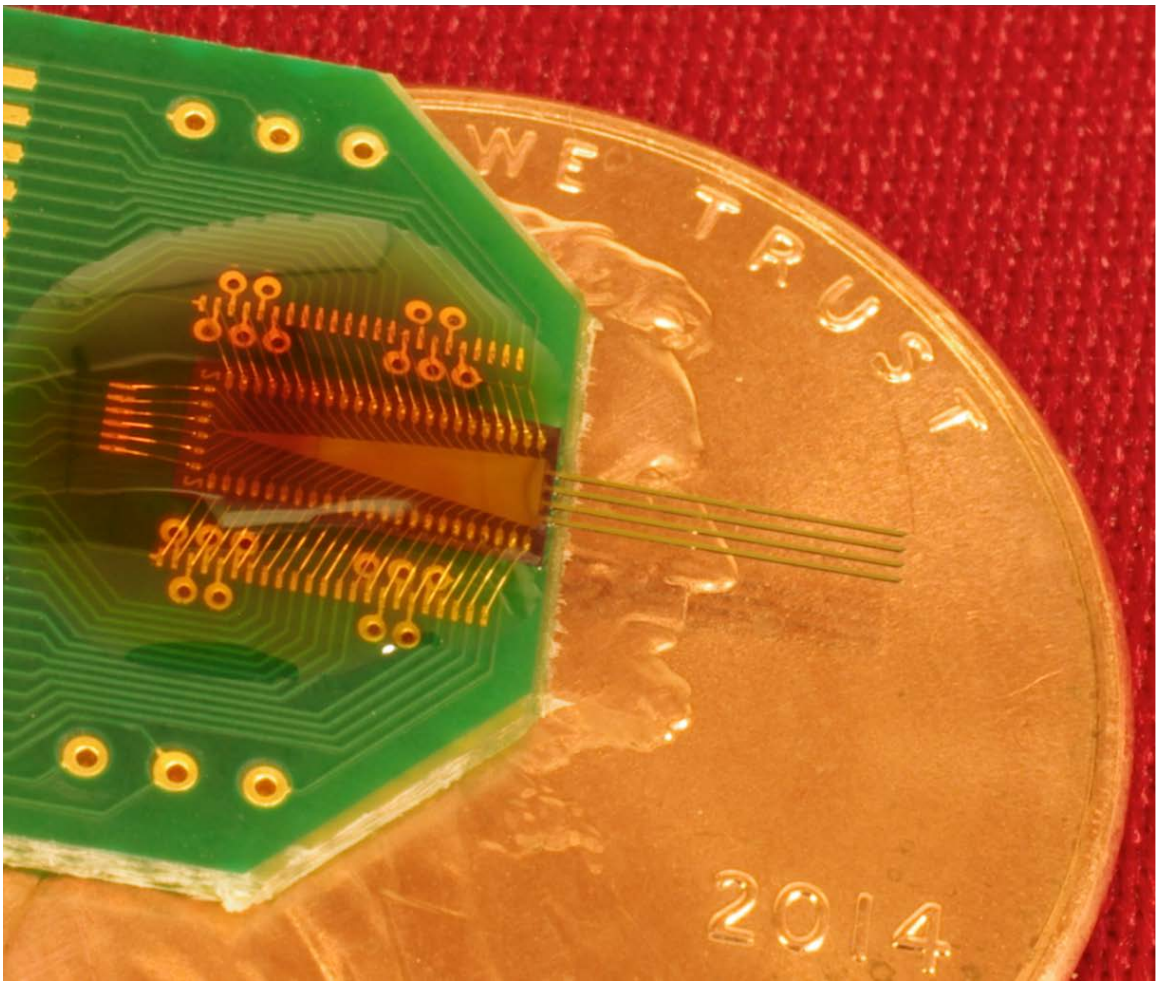

Figure 4.11: Probe wirebonded to a customized PCB.

4.6. µLED characterization

The µLED efficiency is the utmost important determining factor for feasibility of the fabricated probe: the output power must be sufficiently high enough to activate targeted opsins without exceeding the input power limit as constraint by the thermal budget and interference to the recording channels.

The LED plug efficiency or power conversion efficiency (η_0) can be approximated by $\eta_0 = \eta_i \times \eta_r \times \eta_e$. The first term, η_i, is defined as the injection efficiency of the LED, which indicates the fraction of injected carriers that enter the

quantum wells. The injection efficiency is strongly affected by the fabrication process, especially by the quality of the p-GaN ohmic contact formation and interconnects patterning. Once these steps were optimized, the I/V characteristic of the μLEDs should show a low turn-on voltage and small differential resistance. The second term, η_r, refers to the internal quantum efficiency (IQE), which measures the fraction of carriers inside the quantum wells that radiatively recombine to generate photons. Commercially available LEDs on sapphire substrates can easily achieve greater than 80% IQE. GaN LEDs fabricated on a Si substrate unfortunately have more than one order of magnitude higher dislocation density ($5\times10^9/cm^2$) as compared to sapphire (DD ~ $3\times10^8/cm^2$), which will trap injected carriers and prevent radiative recombination. As a result, the IQE from GaN-on-Si LEDs has been measured to be around 33% by other work[136]. The third term, η_e, refers to the extraction efficiency, which indicates the fraction of generated photons that can escape the semiconductor. The photons generated at the active region (MQWs) are emitted in all directions. The opaque silicon substrate absorbs almost all of the photons emitted downwards (approximately half of the total photons). A majority of the other half of the generated photons emitted away from the substrate is trapped by total internal reflection (TIR): only the fraction of photons hitting the GaN/air interface with an incident angle less than the critical angle θ_c can be extracted[136]. A simple first order approximation using equations $\eta_e = 0.5 \times (1 - \text{Cos}(\theta_c))$ and $\theta_c = \text{Sin}^{-1}(n_{GaN}/n_{air})$ reveals that only 4.5% of the photons fall within the extraction cone, using index of refractions values $n_{GaN} = 2.45$ and $n_{air} = 1$. Additionally, the Ni/Au current spreading layer has 75% measured transparency to blue light. The extraction efficiency, η_e, is therefore only 3.37%, which is similar to the results from the

previous report[136]. Photon extraction is a common challenge to all LED designs, which in most application can be alleviated by roughening the semiconductor surface to reduce TIR[137]. This method was not explored in this work due to the significant complication of the fabrication process after surface roughening (e.g., poor ohmic contact to p-GaN). Therefore, the theoretical plug efficiency for the μLED-on-Si is roughly 0.9% (product of IQE and extraction efficiency), assuming negligible injection loss from the optimized fabrication process and negligible Fresnel reflection.

Figure 4.12 shows the first neural probe with monolithically integrated μLEDs arrays lighting at the tip of the shanks. Qualitatively, the emission appears uniform on a single μLED, suggesting that the injected current is uniformity distributed across the entire mesa. In addition, the 3 μLEDs biased using the same voltage source also showed uniform emission, which indicate consistent fabrication quality in terms of contact resistance, interconnect resistance, etc., because any variation would be exaggerated visually, as the optical power is an exponential function of the bias voltage. **Figure 4.13** shows all 12 μLEDs being driven at the same time. In this fabrication run, around 50% of the probes had all 12 functional μLEDs, and the other 50% had only 1 or 2 mal-functioning μLEDs. The photoluminescence plot from **Figure 4.14** shows the emission wavelength centered at 440 nm, which is within the sensitivity range of ChR2.

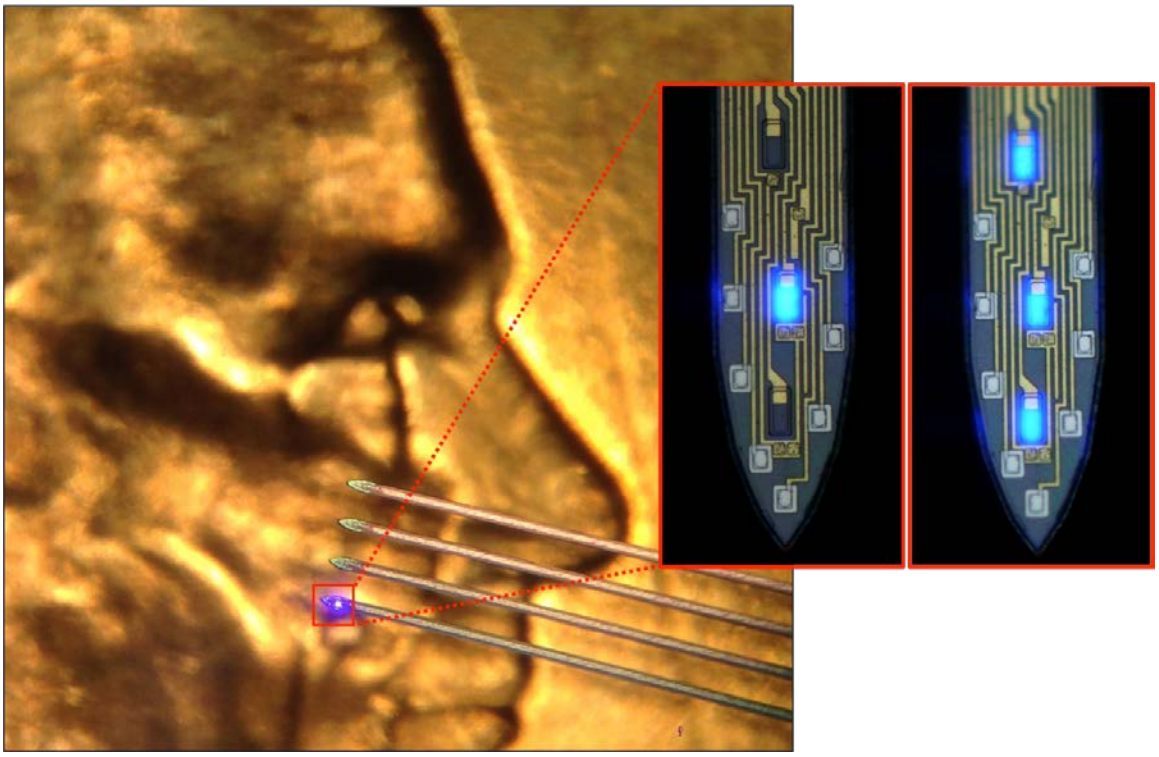

Figure 4.12: Microscope images of the fabricated probe on a U.S penny (left) and high magnification images showing single and triple μLEDs lighting at the probe tip (right).

Figure 4.13: All 12 μLEDs lighting captured by low magnification microscope.

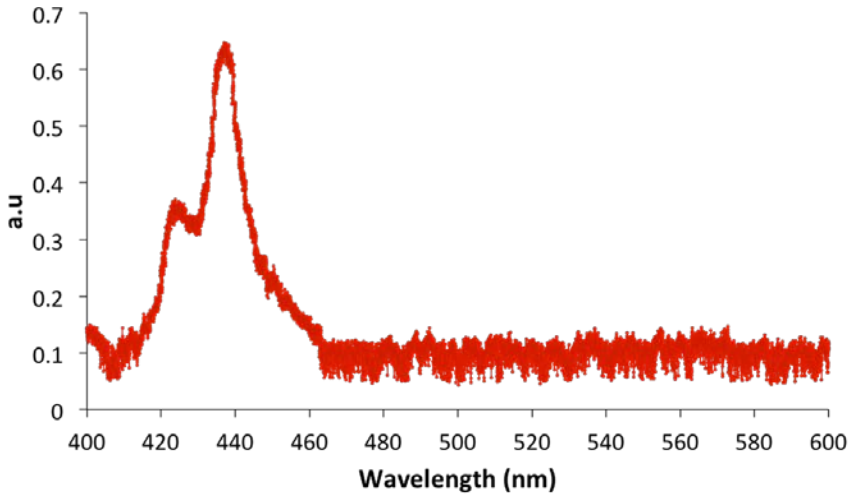

Figure 4.14: Photoluminescence measurement from the GaN-on-Si wafer.

The characterization of μLED performance is summarized in **Figure 4.15**. Emission was visible to bare eye at a bias voltage of ~ 2.4V. In some previous device runs, when the poor ohmic contact to p-GaN was made by sputtering ITO, the μLEDs did not turn on until over 10V. The high turn-on voltage was attributed to the Schottky barrier between ITO and p-GaN[133], [138]. In the modified process, a thin Ni/Au film was annealed at 500 °C for 5 minutes to form an ohmic contact to p-GaN, which showed nearly 4 orders of magnitude reduction in contact resistance. This improvement increased the overall plug efficiency of the μLEDs (the ratio between total optical output power to the total electrical input power) by nearly 4 times. From **Figure 4.15**(b), although the total output power was in the microwatt range, the intensity was significantly higher than 1 mW/mm^2 that is required for ChR2 activation[92]. This is because of the small emission area of the μLED, which also has advantages of high resolution for confined stimulation. The output power saturates at around 53 μW (333.25 mW/mm^2 assuming uniform emission from the entire μLED surface of 150μm^2) with 12

mA of injected current, which can provide an option to stimulate a larger tissue volume. The efficiency droop for InGaN-based LEDs is a well-known phenomenon but is still largely under debate[139]. The similar effect can be shown in **Figure 4.15**(c). **Figure 4.16** shows the near-threshold performance of the μLED. The lowest detectable output power of 0.02 nW occurred at 2.4V bias, with only 20 nA of current injection. The operating point that produced 1.2 mW/mm^2 (just barely over the published ChR2 threshold) is at 3.1V, 7.38 μA (22.88 μW input power), which was in fact near the measured peak plug efficiency of 0.87%.

,

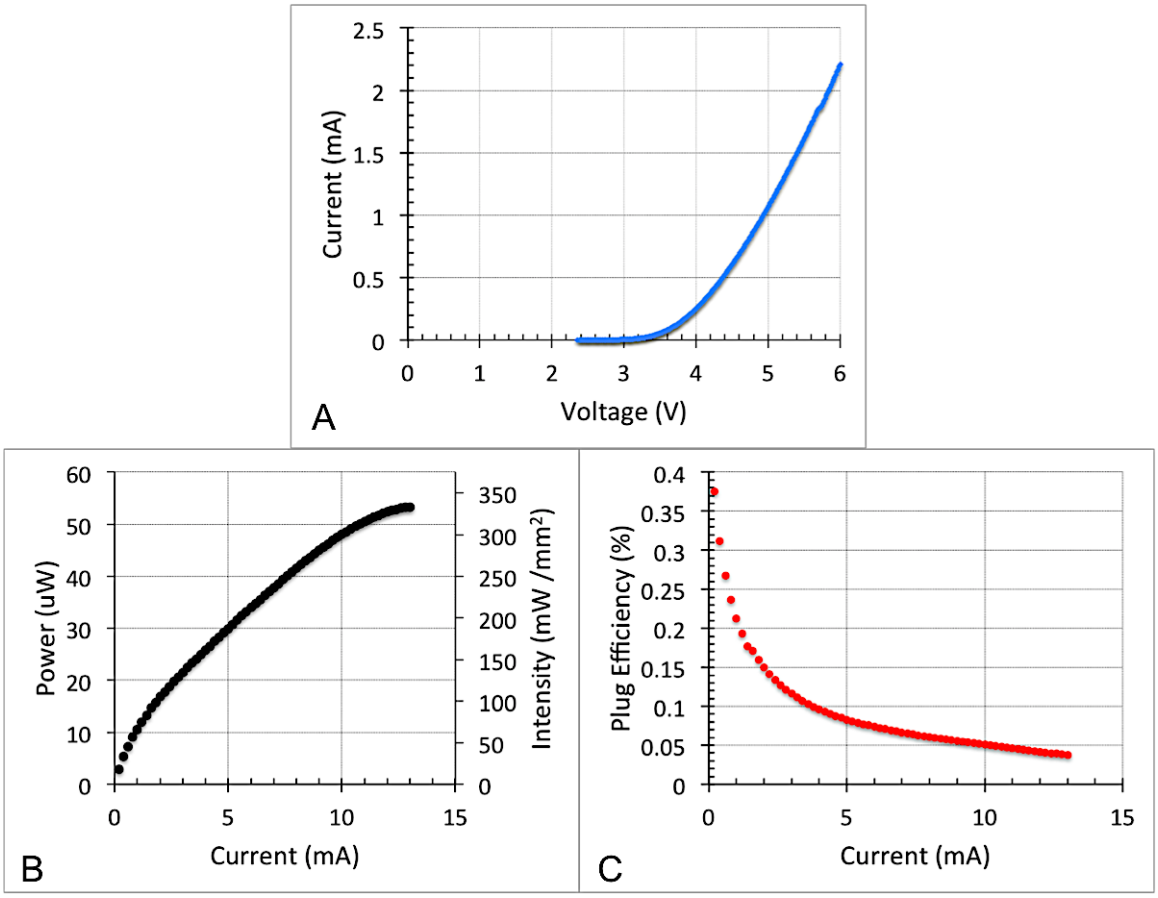

Figure 4.15: Measured characteristics of the μLEDs across large bias range.

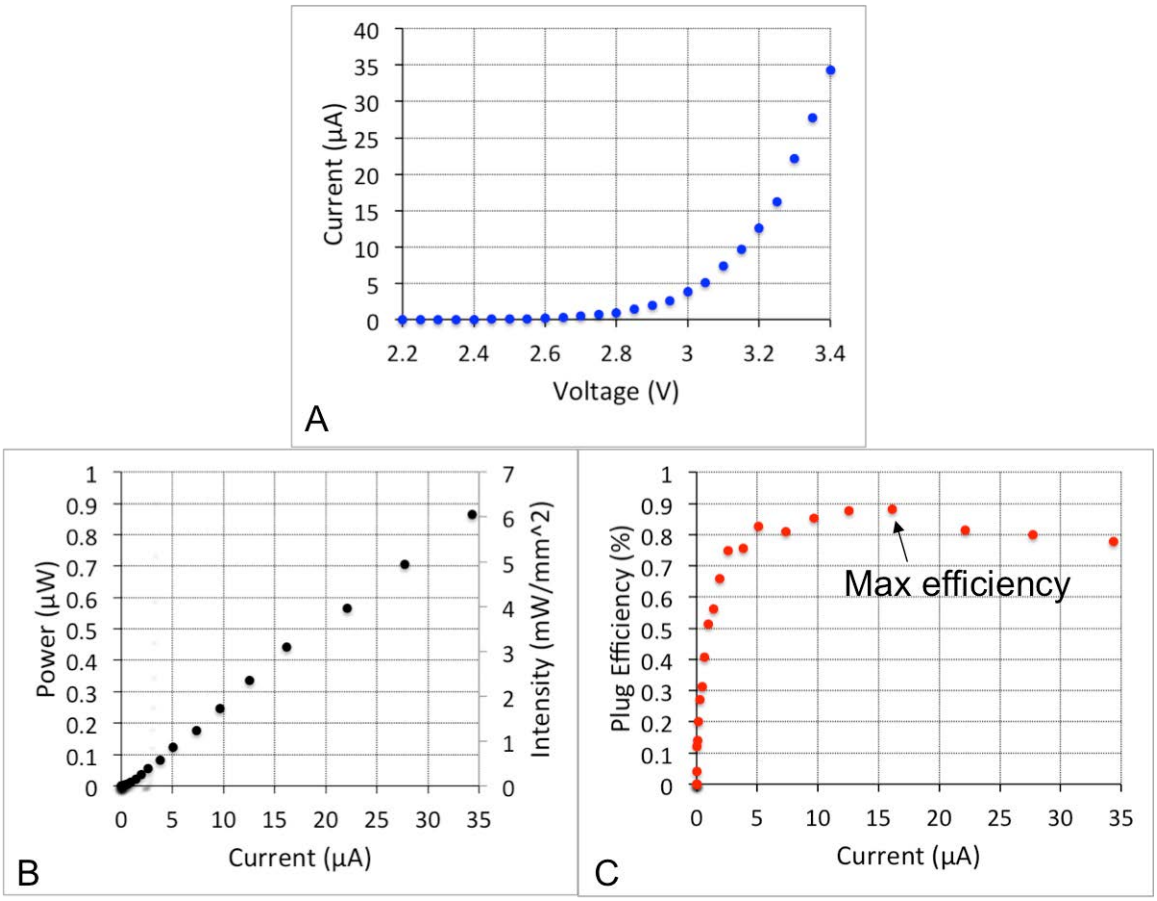

Figure 4.16: Measured characteristics of the µLEDs near the threshold.

4.7. Thermal modeling

According to the literature, even the slightest increase in temperature over 1ºC can adversely affect neural tissues[140]. In this study, COMSOL Multiphysics software was used to estimate the temperature rise in nearby tissue during µLED operation. The upper µLED driving power limit was simulated to meet the thermal budget. To simplify the model, only the probe tip with 3 LEDs on a 60-µm-vertical-pitch was modeled as shown in **Figure 4.17**. The probe shank consists of 30-µm-thick bulk silicon with 2-µm-thick GaN and 1-µm-thick oxide on top. A large rectangular box with a boundary surface 300 µm away from the probe is drawn to model the surrounding brain

environment (not shown). **Table 3** summarizes material properties used in the COMSOL model. The thermal energy will mostly be contained within the GaN and Si layers due to the high thermal conductivity of these materials. The brain ambient was defined with a convective coefficient of $5W/Km^2$ to model the capillary cooling effect[141]. Large specific heat of the brain ambient also helps to increase the thermal time constant, which slowed the tissue temperature rise. **Figure 4.17** shows the temperature rise across the probe tip when the μLED was driven by 1 mW input (electrical) power. The maximum temperature rise of LED1 is roughly 0.2 °C higher than that of LED3, as shown in **Figure 4.17**(a, c), because the silicon probe shank (high thermal conductivity) acts as a heat sink and distributes the thermal energy towards the backend. For the same reason, when all three LEDs are turned on at the same time (**Figure 4.17**(d)), the maximum temperature also occurs at the probe tip.

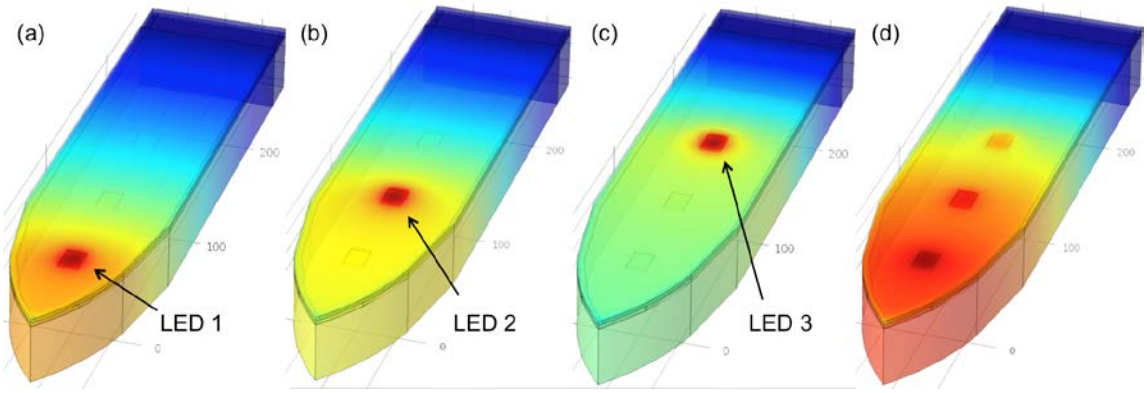

Figure 4.17: Surface temperature distribution across the probe tip with each LED operating at 1 mW electrical power input, showing (a) LED 1 on: T_{max} = 37.75 °C; (b) LED 2 on: T_{max} = 37.61 °C; (c) LED 3 on: T_{max} = 37.5 °C; (d) all three LEDs on: T_{max} = 38.39 °C.

Material	Thermal conductivity [W/(J*C)]	Specific Heat [J/(kg*C)]
Brain ambient	0.45	3650
GaN	230	500
Si	130	700
SiO_2	1.4	730

Table 3: Material properties used in the COMSOL model.

To conservatively estimate the upper limit of input power, it is important to simulate the temperature rise of μLEDs at the steady-state condition. **Figure 4.18** shows the temperature change of LED1 (the distal LED) during a period of 1.4 seconds, where the system has reached thermal equilibrium. The result indicates that even if the μLEDs are continuously turned on in the brain, the temperature rise would not exceed the 1° C limit with voltage bias less than 3.4V. In fact, all of the data points shown in **Figure 4.16** are below this thermal threshold. At 3.4V, the output power is 0.91μW, corresponding to an optical power of 6.06mW/mm^2, which is certainly capable of activating ChR2.

More realistically, typical *in vivo* studies require pulsed light output with duration in the order of, or less than, the thermal time constant, which is approximately 150 ms. In these more practical cases, temperature would not reach its steady-state value. For example, if a 30ms long square pulse is used, the maximum bias would be 4.37V, corresponding to 2.2mW in electrical input power as shown in **Figure 4.19**, and 7.28μW (45.5mW/mm^2) in optical output power, respectively. Even higher optical output power can be obtained up to 53μW (the μLED operation limit shown in **Figure 4.15**(b)) with proper input frequency and duty cycle[106].

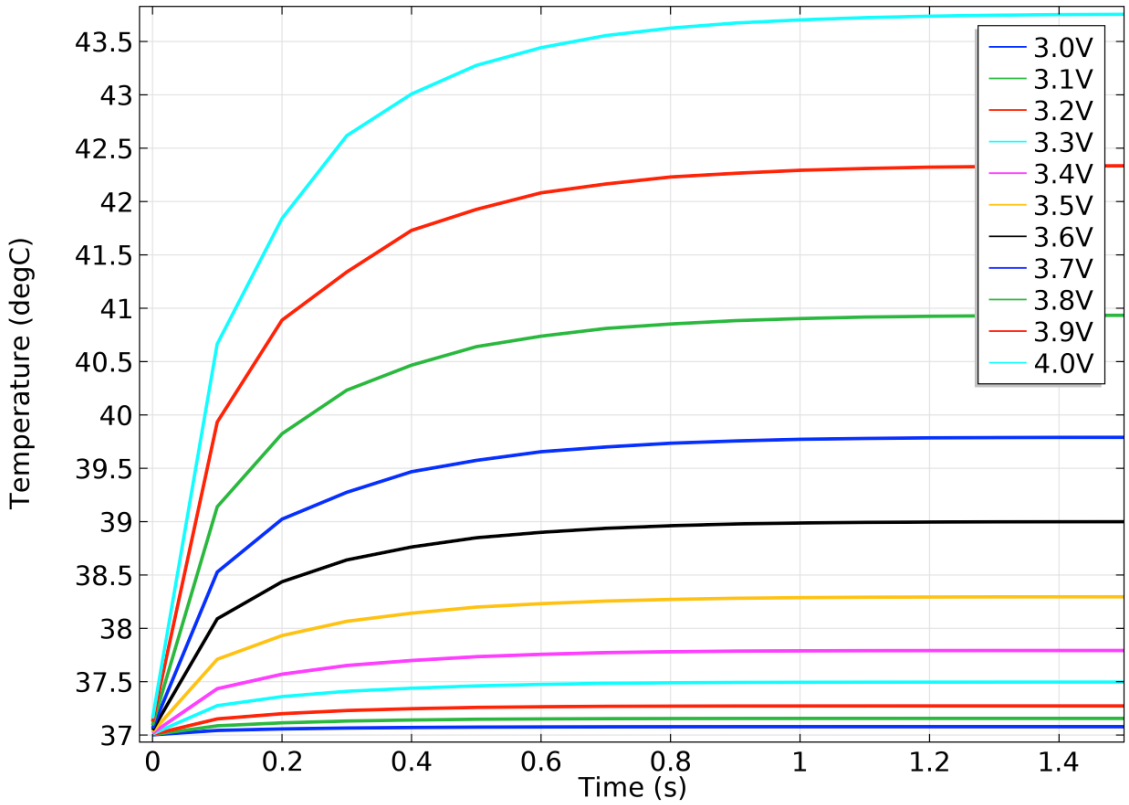

Figure 4.18: Extended time thermal simulation of the LED1, showing equilibrium temperature at different input voltages.

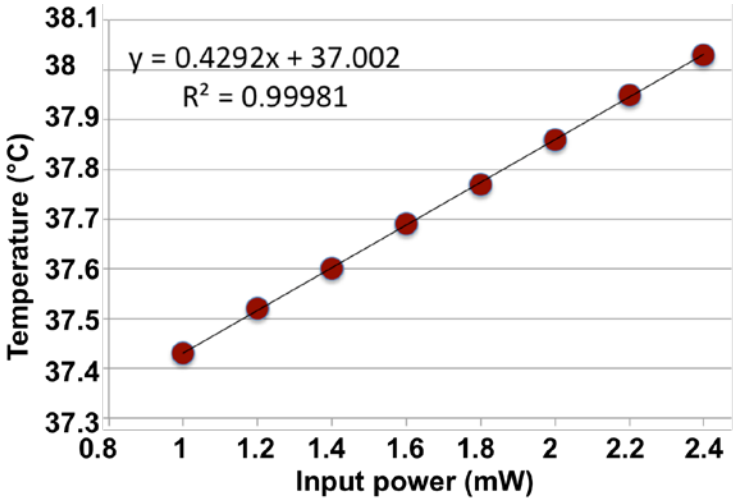

Figure 4.19: Temperature rise in tissue above LED1 at t = 30 ms with varying input power.

4.8. Acute *in vivo* studies

The probes were tested in urethane-anesthetized mice (CaMKII::ChR2). All testing was done with the same probe, which was repeatedly used in 5 acute animals and the recording was done with a multiplexed (AmpliPex) system. The entire headstage (PCB and the multiplexor) was shielded by a copper mesh in order to minimize ambient interference. The targeted brain region was the CA1 pyramidal layer inside the mouse hippocampus. The 50-μm-thick layer is densely packed with cells (4-6 cells across) as shown in **Figure 4.20**. It is extremely challenging to position an array of electrodes accurately to record from this tiny layer of cells. Therefore, it was crucial to design a dense array of recording electrodes and μLEDs to interact with as many of these cells as possible. It was also important to minimize the shank dimensions so that the displacement of tissues during probe insertion does not significantly deform the layer.

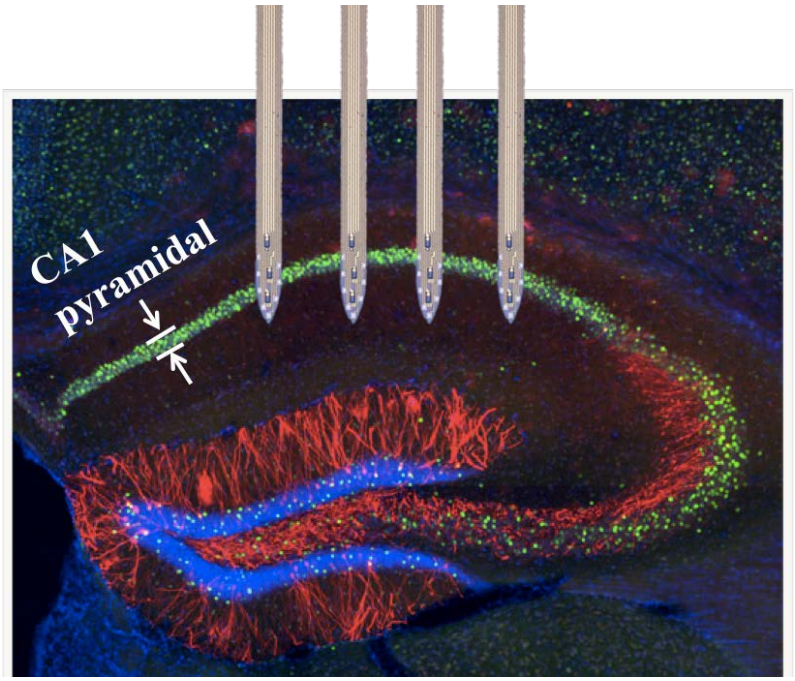

Figure 4.20: Fluorescence image of the mouse hippocampus with a superimposed, hypothetically inserted probe. The dense layers of cell bodies (labeled in green) show the CA1 pyramidal layer (image credit: Steve Ramirez and Xu Liu from MIT).

Figure 4.21 shows the spontaneous recording in the CA1 pyramidal layer when the electrodes have been optimally positioned in terms of implantation depth. The recording sites were color-coded in categories according to the shank number. Single-units pyramidal cells (PYR) and interneurons (INT) were identified and mapped in **Figure 4.21**(b), which could in fact be used to layout the CA1 pyramidal layer. The position of the probe relative to the CA1 pyramidal layer can be speculated with the illustration in **Figure 4.20**. In anesthetized mice, the ripples were easily observed as shown in **Figure 4.21**(b, c). These ripples have been hypothesized to associate with memory consolidation and are especially prominent when the animals are not moving[30]. Concurrent spiking in **Figure 4.21**(d) can also be identified to match the waveforms recorded in **Figure 4.21**(c).

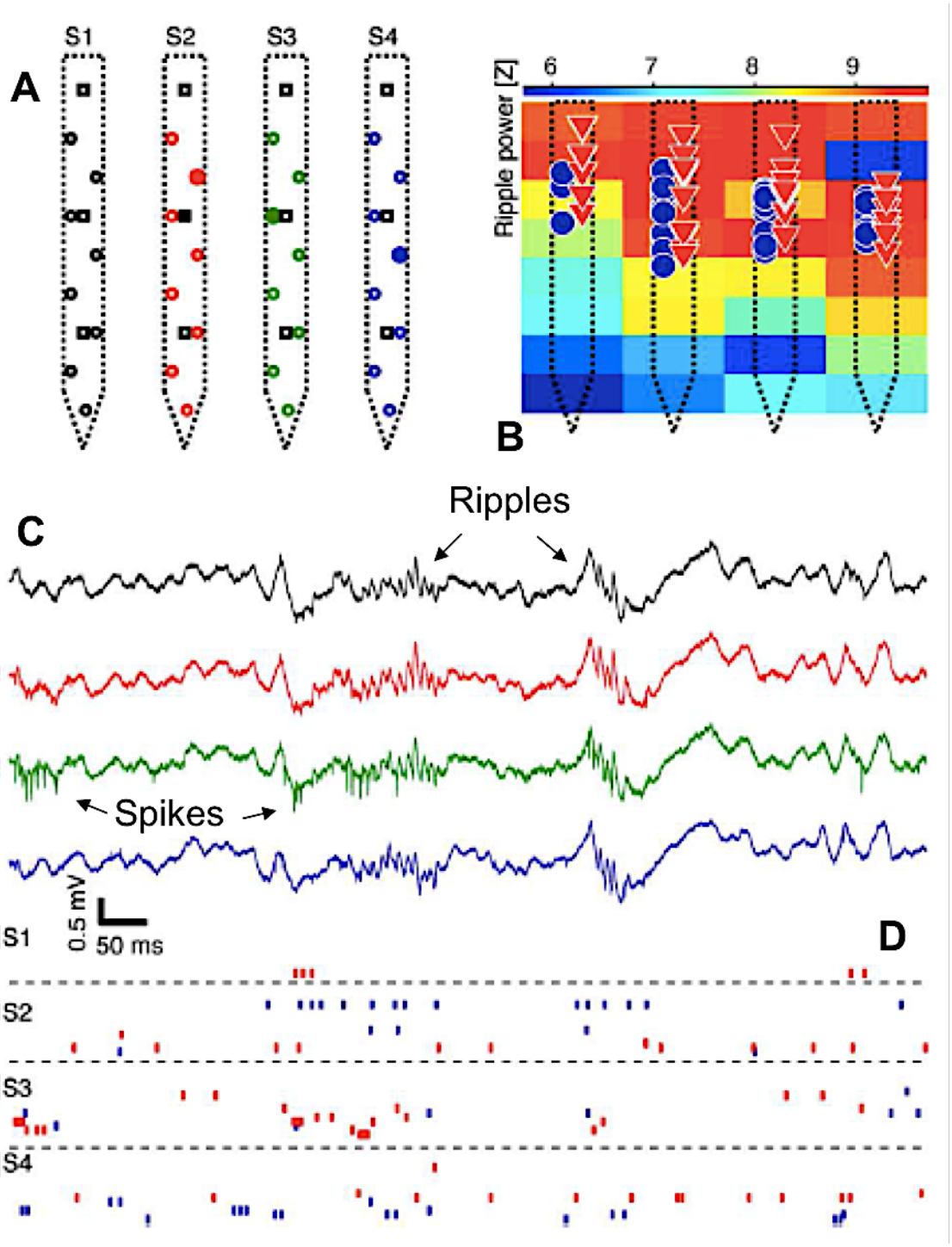

Figure 4.21: Spontaneous activity recorded from CA1: (a) mapping of the electrodes and μLEDs with color coding; (b) ripple power heat plot (one malfunctioning recording site on shank 4) with superimposed location of identified pyramidal cell (PYR, red triangles) and interneuron (INT, blue circles); (c) 1s snapshot with 2 consecutive ripples and spikes; (d) concurrent spiking (red, PYR; blue, INT).

Figure 4.22 shows the optically induced activities using the same probe at the same location as shown in **Figure 4.21**. Using sine-wave (5 Hz) stimulation, there was clear entrainment of neural activity by light. However, whenever the LED power was on, there was significant interference, which was capacitive coupled to the recording channels via the n-GaN layer. Using low bias (0-3.6V) to drive a μLED on the third shank (green) and after filtering out the artifacts, robust spiking was observed (green trace in **Figure 4.22**(b)). At the same time, the red and blue traces from the adjacent shanks only recorded spontaneous activities: no light effect was observed. **Figure 4.22**(c) shows the gain (total number of light-induced spike events over the number of spike events during spontaneous activity) relative to the phase of the sine-wave input. It can be shown that when the μLED on shank2 was turned on, only the channels on shank2 recorded gain in spike events (**Figure 4.22**(c, top left)), whereas the channels on shank3 recorded zero gain (**Figure 4.22**(c, top right)). Similar effects can be seen when the μLED on shank 3 was turned on and the resultant spike events contrast between shank2 and 3 (**Figure 4.22**(c, bottom row)).

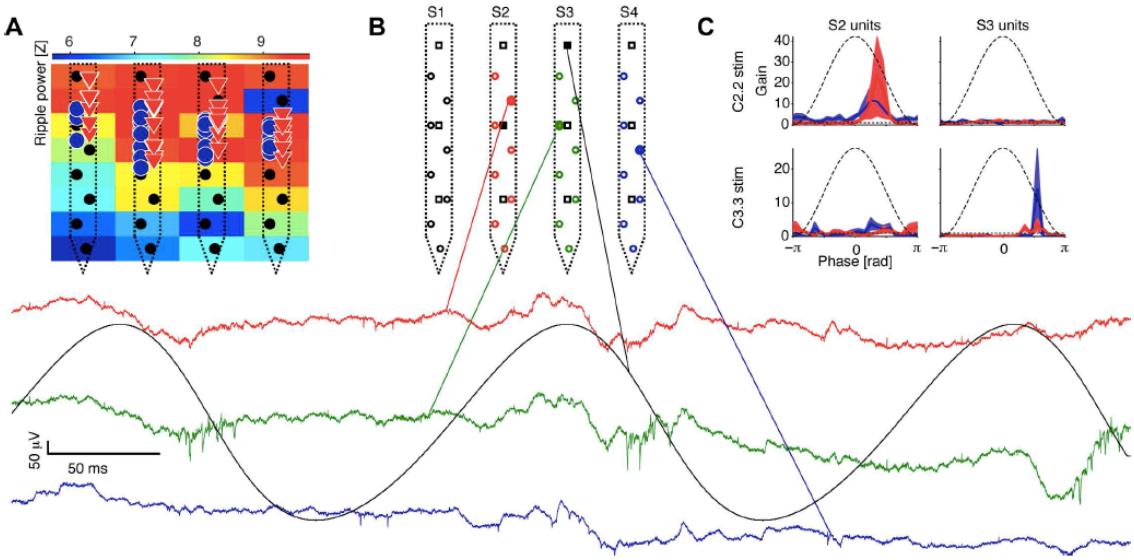

Figure 4.22: (a) Layout somata and spatial distribution of ripple power during spontaneous activity; (b) Probe layout and wide-band, artifact-free traces from 3 shanks during sine-wave polarization on shank 3 (5 Hz, 0-3.6V, central LED – black circle). Note local induction of entrained spikes on shank3 (green trace). (C) Group data, shown separately for units recorded on shank 2 (S2) and on shank 3 (S3; PYR in red, INT in blue). Different rows show the neuronal activity during polarization of the central shank 2 LED (C2.2) and of the top LED on shank 3 (C3.3). Note localized entrainment of cells on the shank level.

4.9. Chronic *in vivo* studies

For chronic studies, 4 probes were mounted on a movable micro-drive and were implanted into 4 mice (two CaMKII::ChR2 and two wild type), respectively. In order to reduce the interference as observed during the acute experiments, the stimulation cable was built out of two 24-strand Litz cables that were shielded and grounded (12 signal wires and 2 ground wires to power the μLEDs, the rest were used to provide shielding). All stimulation cable grounds were connected to the recording ground (earth) directly.

The mice were allowed to recover over a course of one week and then recordings and stimulation were carried out, targeting the CA1 pyramidal cell layer. To be safe, the probes were first inserted to about 0.8 mm in depth to reach the neocortex, so that the

probe tips do not pass through the CA1 pyramidal layer, which is located at around 1.1mm to 1.7mm in depth. Brain edema during surgery is common, so the exact depth of the target cannot be accurately predicted. Because the CA1 pyramidal layer is composed of only 4 to 6 cells across (~50-μm-thin) as shown in **Figure 4.20**, the probes were advanced slowly at a rate of 70μm per day while observing the signals from the electrodes. All 4 probes rarely recorded spikes from the neocortex. As the probe tips finally reach the CA1 pyramidal layer, spontaneous spiking and ripples were first observed at the tip-most electrodes while the upper electrodes were silent as they were still in the CA1-orien, a sub-layer structure mostly absent of cell bodies. **Figure 4.23** shows a snapshot of the spontaneous recording at the CA1 layer. Here, a single ripple (140-180 Hz oscillation) can be seen across the recording channels, which was a clear indication that the recording electrodes were inside the CA1 pyramidal layer[30]. The red traces in **Figure 4.23**(a) show the location of maximum ripple power. The individual cells can be identified and located after spike sorting and are shown in **Figure 4.23**(b) with the pyramidal cells (PYR; red triangles) and interneurons (INT; blue circles). The location of the PYR cells and the maximum ripples can be used to map the CA1 pyramidal cell layer across the 4 shanks.

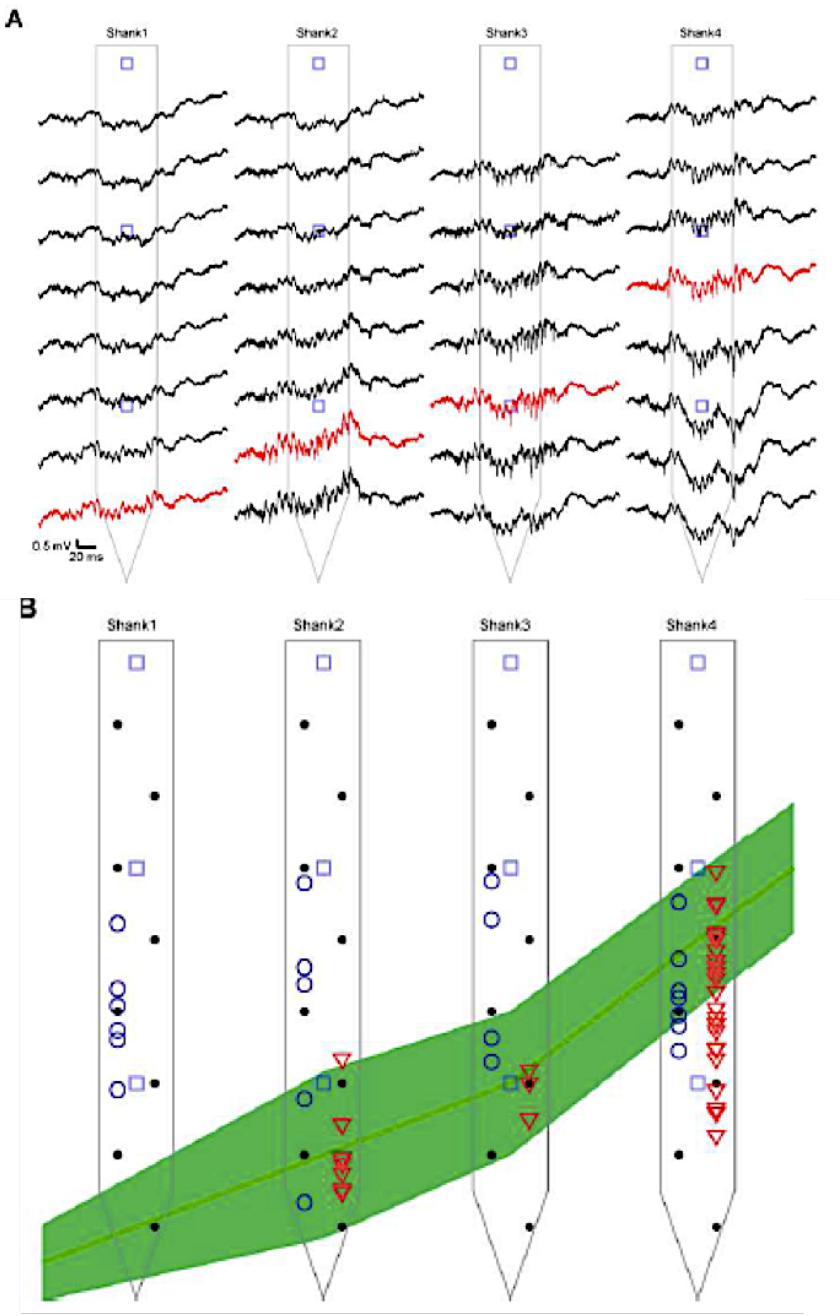

Figure 4.23: Spontaneous recording in chronically implanted mouse at the CA1 pyramidal layer: (a) Snapshot of wide-band recording (0.3-10,000 Hz; 200 ms; 31 recording sites) from CA1 of a freely moving mouse during a single CA1 ripple. Red traces indicate the estimated center of the CA1 pyramidal cell layer; (b) example recording session showing the estimated locations of pyramidal cells (PYR; red triangles), interneurons (INT; blue circles), and the center of the CA1 pyramidal cell layer (sites with maximum ripple power are connected by the green line and the green band thickness represents the mean ripple power). The recording sites are shown as black circles and the μLEDs are shown as blue squares.

Following the stimulation procedures for the acute animal study, a 5 Hz sine-wave stimulation waveform was also used to drive the μLEDs in both CaMKII::ChR2 mice and wild type mice. The amplitude of the sine wave varied between 0V and a peak value ranging from 2.5V to 4V. The intensity of the μLEDs at the peak of the sine wave can be easily found in **Figure 4.16**. It should be noted that, even though the input waveform was a sinusoid, the μLEDs were only turned on during a short pulse when the voltage surpassed the diode threshold which is ~2.8V. This method effectively eliminated the high frequency component of the electrical input (if a square pulse was used) to generate a short pulse of light; thus reducing the interference capacitively coupled to the recording channels. **The effects of the optical stimulation were clearly observed in the CaMKII::ChR2 animals and were intensity dependent: spikes was induced at low intensities (as low as 2.9V, corresponding to about 37nW, 0.25mW/mm^2 intensity), and high frequency oscillations (HFOs) were induced at higher intensities (as low as 3.2V, corresponding to about 350nW, 2.3mW/mm^2 intensity).** In contrast, no effects on spiking or HFOs were seen in any of the wild-type animals, despite the fact that the probes were recording spikes and ripples from the CA1 pyramidal cell layer. This evidence rejected the hypothesis that the electrical current used to drive the μLEDs can also generate spikes due to capacitive, inductive or thermal effects.

Figure 4.24 demonstrates the high spatial resolution that can be achieved using low optical power stimulation. All 4 cases show the recorded data from the same location with stimulation amplitude ranging from 0V to 3.35V to drive the μLEDs (peak optical output power: 0.8μW, 4.9mW/mm^2). The blue/red open circles mark the

estimated locations of the somata (cell bodies): triangulation was only possible in the vertical dimension. Therefore, the blue circles (INT) were plotted to the left and the red ones (PYR) were plotted to the right for convenience.

For optical activation at the specified level, all spikes of a given cell were collected during a recording session. Each cell was then assigned a vector: the magnitude (0-1) defined the fraction of spike events that were phase-locked to the light input; the phase (0-2π) defined the relative timing between the sine wave peak and the spike. If a cell were statistically phase-locked to the light input, it was plotted as a filled circle, with the diameter and color representing the magnitude and phase, respectively. For example in Case1, when the lower μLED was turned on, two PYRs within 20 μm of the μLED were strongly entrained, firing near the peak of the light as shown by the two large red circles. These two PYRs were not entrained in Case2, as shown by the two open circles, when the middle μLED (60μm away from the lower μLED) was turned on. In this case, an INT just below the middle μLED was entrained more strongly than in Case1, and appeared in phase with the light peak. Because the animals were CaMKII::ChR2, INT cannot be directly affected by light. Therefore, the activation of INT was an indirect effect, most probably by the output of a nearby PYR that was activated by light. This was consistent with an unpublished work from Prof. Buzsaki's group showing the PYR activation of INT with very short time lag (3ms). In addition to the local circuit activation, distant indirect effect was also observed using low power stimulation. In both Case1 and 2, a PYR on shank4 was strongly entrained by both μLEDs. This suggested an indirect PYR-INT-INT-PYR circuit (note PYR is excitatory cell and INT is inhibitory cell), where the first PYR was illuminated by light and the output eventually activated

the second PYR with a series of INT connections. The expected delay as signal propagate through this circuit was consistent with the $\pi/2$ phase shift as indicated by the cyan fill, which also disambiguate the circuit effect from a direct light effect precisely because the cell fired only during the absence of light.

Similar effects can be observed on shank4 as shown in **Figure 4.24**, where the lower and the middle μLEDs induced activities from different cells. The nearest cells to each of these two μLEDs were further analyzed to demonstrate the sub-layer resolution in **Figure 4.25**. In this figure, the two PYRs were labeled by the red and pink triangles, respectively. The red PYR and the pink PYR had the highest recording amplitude near the 6^{th} and 4^{th} electrode, respectively. Therefore, the separation distance between these two cells were only around 50μm, which is equivalent to the thickness of the CA1 pyramidal layer. Clearly, when the μLEDs were driven with low peak intensity of 4.9mW/mm^2, only the PYR close to the μLED was phase-locked, while the other PYR at the opposite side of the CA1 pyramidal layer did not respond to light. **These observations clearly demonstrated sub-layer stimulation resolution, even within the 50-μm-thin band defined by the CA1 pyramidal layer.**

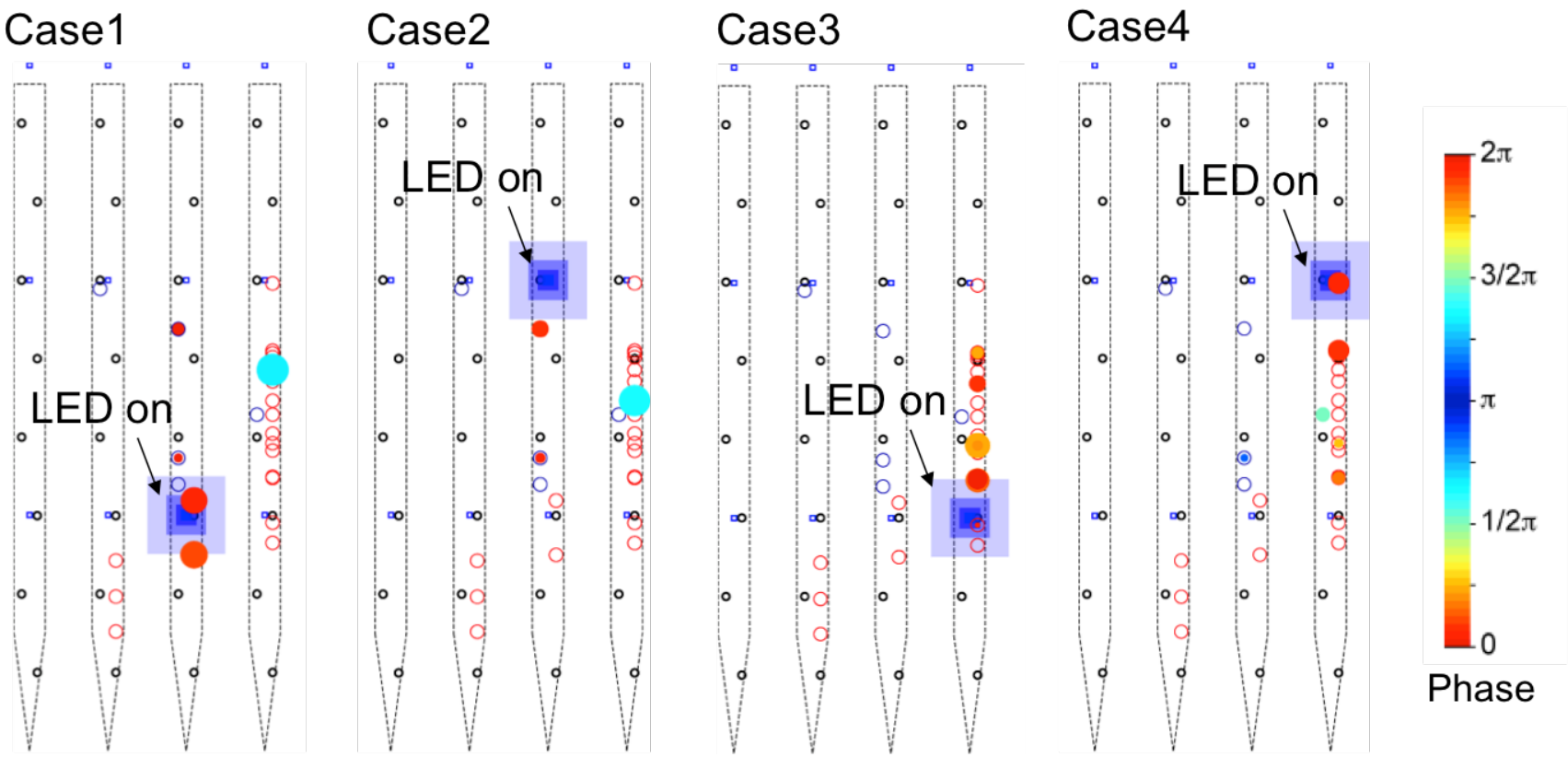

Figure 4.24: Stimulation using low optical power (0.8μW, 4.9mW/mm^2) showing precise localization of induced activities even with adjacent μLEDs. Case1 and 2 show different activities induced by two μLEDs on shank 3; Case 3 and 4 show different activities induced by two μLEDs on shank 4. The diagram shows μLEDs (blue squares), recording electrodes (black circles), PYR (open red circles), INT (open blue circles). Each operating μLED is shown as enlarged blue square. Cells that are phase-locked to the light input are shown as filled circles: the diameter of the circle is proportional to gain in spike event rates that are phase-locked to the light stimuli; the color of the filled circles represent the phase between induced spike timing and the peak of the sinusoid light input.

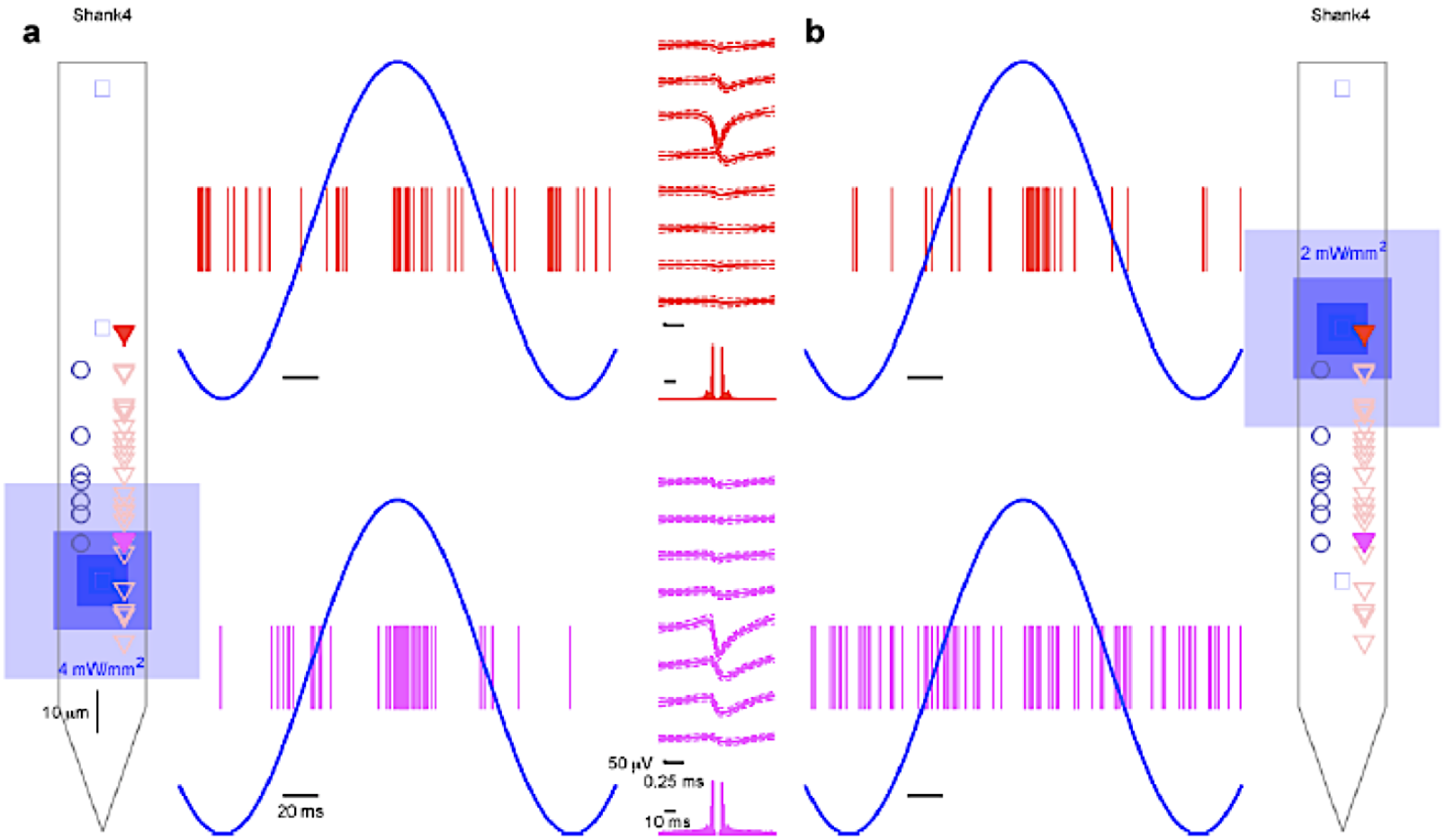

Figure 4.25: Sub-layer resolution control of spiking in the CA1 pyramidal layer shown by independent control of distinct cells on shank4 between the bottom and middle µLEDs using same bias conditions in **Figure 4.24**: (a) bottom µLED generated phase-locked spiking of a well-isolated PYR (pink) next to the µLED, but not of another well-isolated PYR (red) at the opposite side of the pyramidal layer; (b) middle µLED generated phase-locked spiking of the adjacent PYR (red) but not of the distant PYR (pink).

In contrast to using low power, confined emission for high-resolution stimulation, higher power (4μW, 28mW/mm^2) stimulation only achieved inter-layer resolution. **Figure 4.26** shows that when the bottom and middle μLEDs were turned on sequentially, several cells were unselectively activated by both μLEDs without phase delay. Since PYR-PYR circuit activations are extremely rare[142], and that PYR-INT-INT-PYR activation would show time lag, the distant in-phase activation can be attributed to the stronger light output reaching remote cells and activating them directly. Very interestingly, illumination above the CA1 pyramidal layer (in the CA1 oriens) by the top μLED leads to anti-phase locking for the same group of cells that were activated in-phase by the bottom and middle μLEDs. **Figure 4.27** shows a single isolated PYR firing in-phase to the sinusoidal light input when the bottom and middle μLEDs were turned on. The same cell fired during the anti-phase, at the absence of light when the top μLED was used. This result demonstrated the possibility to control the induced spiking phase relative to the light input (i.e., different activation mechanism of the same cell), by using different μLEDs. This also suggested an interlayer circuit effect, mediated by basal dendrites (dendrites from above the cell, in contrast to most dendrites in CA1, which are apical, or coming from below the cell)[143], which is still unproven to the neuroscience community and would require further evidence to understand its underlying mechanism. The discovery demonstrated that the fabricated μLED probes can allow for conducting a new set of experiments for neuroscience studies that could not have been done using the previous optogenetic devices because they would have unselectively stimulated both the CA1 oriens and the CA1 pyramidal layers.

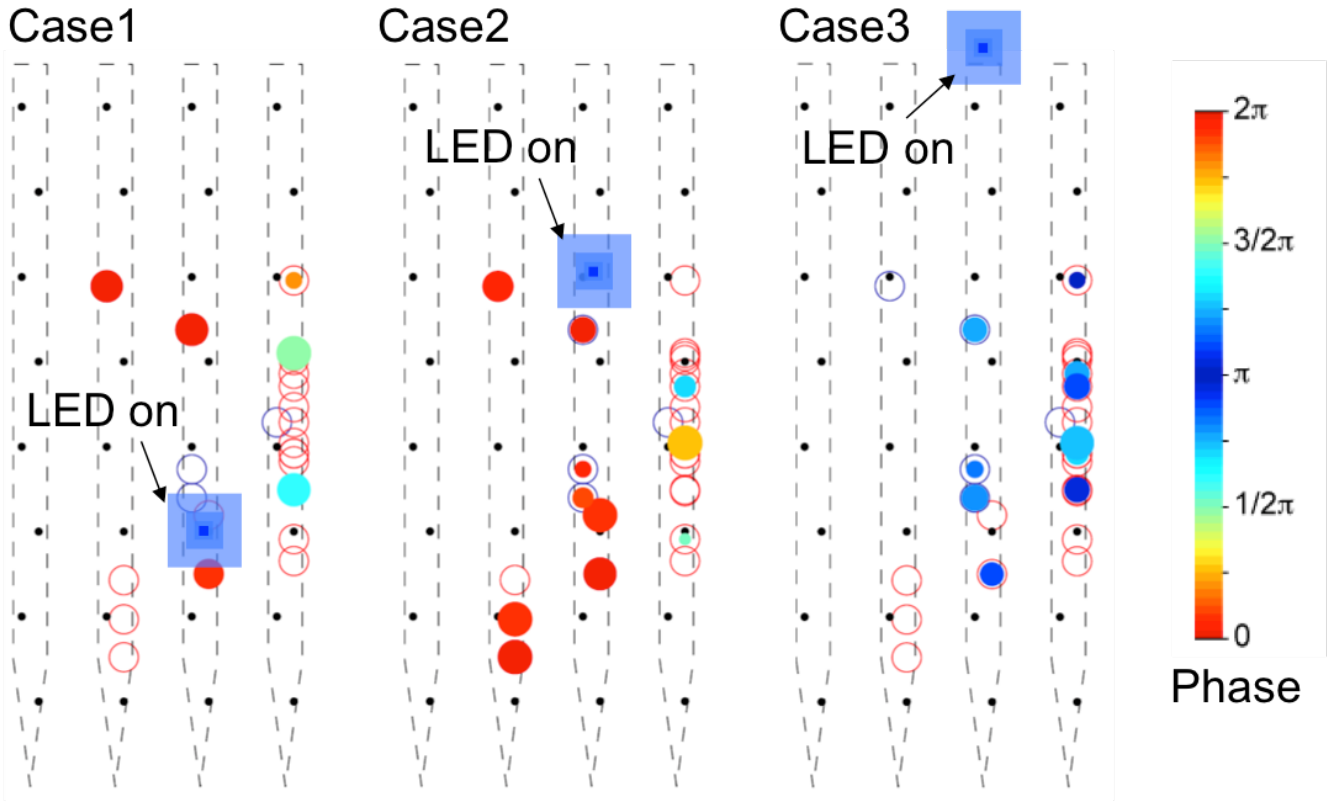

Figure 4.26: Stimulation using relatively high optical power (4μW, 28mW/mm^2) showing several cells activated unselectively by both the bottom and middle μLEDs. The same cells were also activated by the top μLED outside of the CA1 pyramidal layer with a phase delay, indicating indirect circuit effect. The diagram shows μLEDs (blue squares), recording electrodes (black circles), PYR (open red circles), INT (open blue circles). Each operating μLED is shown as enlarged blue square. Cells that are phase-locked to the light input are shown as filled circles: the diameter of the circle is proportional to gain in spike event rates that are phase-locked to the light stimuli; the color of the filled circles represent the phase between induced spike timing and the peak of the sinusoid light input.

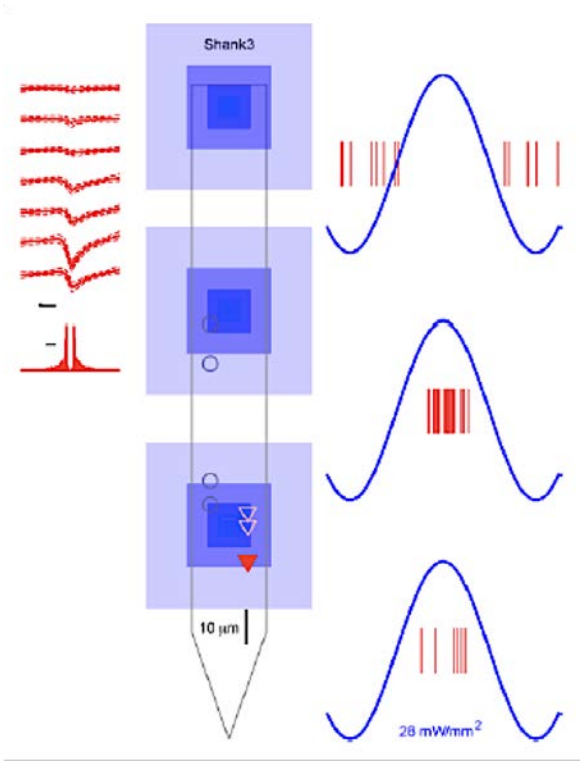

Figure 4.27: Control of spike phase by direct vs. indirect activation. A well-isolated PYR recorded on shank3 fired in a phase-locked manner upon (putatively somatic) illumination with the bottom µLED (5 Hz; peak power, 4 µW; peak intensity at the µLED surface, 28 mW/mm^2), and maintained its phase during application of the same pattern via the middle µLED. However, application of the same pattern via the top LED induced anti-phase spiking (putatively activating the basal dendrites, at the sine wave troughs, i.e., during the lack of light).

4.10. Discussions

The importance of understanding cellular level neural circuit has been highlighted by the recent 2014 Nobel Prize in Physiology or Medicine, which was awarded for the discovery of place cells and grid cells that enable the sense of place and navigation[144], [145]. At the same time, another recent 2014 Nobel Prize in Physics was awarded for the invention of blue LEDs. Coincident or not, the µLED neural probe described in this dissertation bridged the technological advance in semiconductor LEDs to its new application in neuroscience.

One of the early objectives of this work was to eliminate the bulky optical fiber connection in many of the previous work[85], [99], [104], [146] in order to alleviate the constraint on animal movements in behaving experiments. Only few efforts[92] has been made in recent years to couple semiconductor light emitting devices to short optical fibers attached to the probe shanks, thus using only light-weight, flexible electrical cables to deliver the power. It is also possible to couple the off-shelf LEDs or laser diodes to integrated waveguide probes as described in Chapter 3. This method requires significant engineering challenges and assembly techniques to efficiently couple light from the external light source into the small waveguide. However, at least with the current available technologies, it offers the advantage of interchangeable light sources with different wavelengths, which cannot be done easily with the monolithically integrated μLEDs on the probe shanks. Certainly, being able to silence and excite targeted cells is one of the revolutionary advances that optogenetics can offer in comparison to conventional electrical stimulation. Although not a mature technology yet, the emission wavelength of LEDs fabricated from the same material can be tuned by controlling its mesa size and therefore the built-in stress. **Figure 4.28** shows the preliminary work done by Prof. Ku's group from the University of Michigan, which demonstrated multi-wavelength emission from the same LED epitaxy layer by reducing its lattice strain for a blue shifted effect[147], [148]. This method suggests the possibility of monolithically integrating multi-wavelength μLED arrays using the same epitaxy wafer, which would provide another degree of freedom in neural activity manipulation by the added capability of silencing neurons.

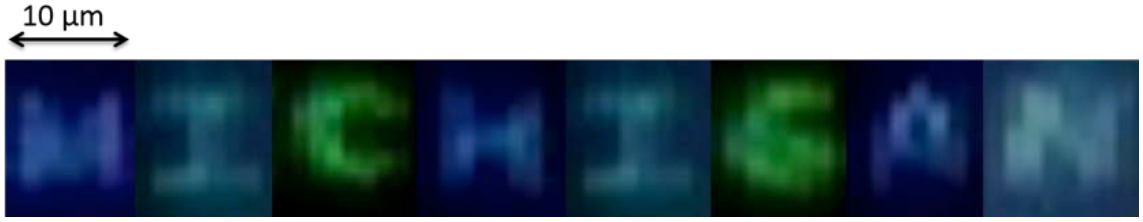

Figure 4.28: Wavelength tuning by changing the built-in stress of individual nano-pillar LED mesas.

The monolithically integrated μLED probe described in Chapter 4 has tremendous impact for the neuroscience community (even with single emission wavelength). It completely eliminated optical fiber connections, which supported behavioral studies in small animals and allowed scaling of the number of μLEDs to 3 per shank for a total of 12 μLEDs, while using the same shank width (70 μm) of the single-shank probe described in Chapter 3. For confined stimulation, the μLEDs were designed to have a small emission area (10μm ×15μm), similar to the size of the recording electrodes and the size of a cell body of neurons. The μLED architecture also minimized its protrusion from the shank surface below sub-micron range, which could further reduce unnecessary tissue damage during insertion. The μLEDs were fabricated on a GaN-on-Si wafer, which has intrinsically a low quantum efficiency due to high dislocation densities caused by lattice mismatch in the GaN/Si interface. However, by optimizing the fabrication processes, it was demonstrated that the μLEDs can be made with low contact resistance and low leakage, so that total measured efficiency at an optimal operating point is close to the theoretically-calculated plug efficiency of 0.9%. Despite the seemingly low efficiency, it was shown that the μLEDs could operate at

their steady state as well as transient, pulsed conditions, to emit light at intensity enough to activate ChR2 without exceeding the thermal budget of 1°C in tissue temperature rise.

The μLED probes were first tested in anesthetized (n=5) and then followed in behaving mice (n=4) at Prof. Buzsaki's lab in New York University. All of the probes were inserted into the optimal position inside the CA1 pyramidal layer of the hippocampus. The acute experiments were designed for initial feasibility assessment. The surgeries (~1 hr) were considerably shorter than chronic implant (~3-4 hrs), and the recording began immediately while the animals were under anesthesia. Spontaneous activities were recorded as soon as the probe tip entered the CA1 pyramidal layer. The frequent ripples were identified as "signature" of CA1 neural activities when the animals are immobile. In these early experiments, both 60 Hz and higher frequency (~2 kHz) interference were significant in recording even without stimulation; during stimulation, the injected current caused additional interference to the recording channels, making observation of neural activities in real time impossible. Fortunately, it was still possible to extract the neural signals from the noisy background with offline processing.

During chronic experiments, the probes were implanted and the animals were allowed to recover for a full week before recording began. The cables and headstage were carefully shielded this time, which completely abolished the ambient noise (60 Hz, etc.). The recording ground and the LED ground were also shorted together with a configuration to avoid large ground loops. This significantly minimized the stimulation interference (although still observable), so that spikes, ripples and HFOs can be easily identified during live recording in real time. Once the probes were inserted into the optimal depth, as all shanks could record spontaneous ripples and spikes from the CA1

pyramidal layer, the optical stimulation experiments began. In these studies, a 5 Hz sinusoidal waveform was used to drive the μLEDs, and the amplitude varied from 0V to a set of values. The minimum light outputs to induce spikes or HFOs from a nearby PYR were determined to be only 37nW (0.25mW/mm^2) and 350nW (2.3mW/mm^2), respectively. When driving the μLEDs near the threshold, sub-layer circuit stimulation was resolvable. This was clearly demonstrated by the selective stimulation of two nearby PYRs (approximately 50μm apart), using two adjacent μLEDs (exactly 60μm in vertical pitch). In addition to direct PYR stimulation by light, INT can also be activated via PYR-INT circuit with very short time lag[30] (note that light cannot directly activate INT in CaMKII::ChR2 animals). Also, distant PYR can also be activated indirectly, via PYR-INT-INT-PYR circuit, in which the first PYR was illuminated and the second PYR responded after long delay during signal propagation[142]. All of the above mentioned circuit effects are shown in **Figure 4.24** using low power stimulation. With higher power stimulation, induced activity was only localized at interlayer resolution. Here an interesting phenomenon was observed for the first time: stimulation of the CA1-orien generated robust spiking and ripples in distant PYRs inside the CA1 pyramidal layer with phase locking to the trough of the sine input (during absence of light) as shown by **Figure 4.26**, and more specifically by the activities of the "red cell" shown in **Figure 4.27**. The underlying signal transduction method is still unknown, but can be speculated. Illumination via the bottom/middle μLED activated the PYR ("red cell" in **Figure 4.27**) directly via somatic or dendritic illumination). In contrast, since light cannot reach the "red cell" from the top LED, one possible mechanism of action is as follows: illumination via the top μLED activated another ("hidden") subset of PYR (via their

basal dendrites), which synaptically activated INT. Those INT can, in turn, generate rebound spiking in PYR[142]. One of the latter PYR can be the same “red cell” that was also directly activated via the bottom/middle μLEDs. Thus, the same cell can spike in-phase or anti-phase, depending on the relative location of the soma vs. input. Equivalently, distinct PYR can either fire in-phase or anti-phase, depending on the source of their respective input.

In conclusion, the μLED integrated neural probe developed in this work enabled high spatial resolution in stimulation of targeted neural circuits. Because the μLEDs can be positioned extremely close to neurons, the amount of light needed to induce robust spiking is minimal. Therefore, confined stimulation of sub-layer neural circuit can be achieved, with power consumption well under the limit to cause thermal damage to the tissue. A few experiments in chronic behaving mice already shed light on some new interesting circuit effects that could not have been observed using the previous devices reported up to date, which could only illuminate a large volume of tissue.

CHAPTER 5

SUMMARY AND FUTURE WORK

5.1. Summary:

The Michigan probe has been leading in multi-site, high-density recording and stimulation for neuroscience applications among other neurotechnologies. The MEMS-based, planar platform enables design freedom for scaling and integration of functions such as microfluidic channels and electrochemical detection. The innovations pursued in this thesis are in line with evolvement towards the next generation Michigan probes.

The work described in Chapter 2 aims to utilize a biodegradable silk shuttle to support the insertion of probes that can be made out of any materials and shape, so that the probes themselves can be structurally optimized to minimize tissue reaction. The techniques for patterning the biodegradable coating have been optimized to facilitate reliable insertion of multi-shank, flexible probes. However, due to the complexity of the foreign body response, the current animal experimental data cannot conclusively support the hypothesis that the silk-coated probes have better recording performance compared to existing probe technologies in the long term. Yet, the coating technology allows tremendous design freedom in forming the structures of future implantable devices, which will be tested and applied in a chronic setting.

The rest of the thesis reports the development of neural probes with the capability to simultaneously record neural signals (extracellular potentials) and stimulate neurons with light. Two approaches have been demonstrated, integrating either optical waveguides or μLEDs onto the conventional Michigan probe. In both cases, the designs revolve around the central idea of leveraging advanced microfabrication techniques to monolithically integrate the optical and electrical components onto the probe shanks. This key design feature enables precise spatial definition of all components with lithographic resolution, which offers optogenetic studies with the ability to accurately map the input and output processes within a neural network. These probes were tested at the Prof. Buzsaki's lab at New York University using rodents. The waveguide integrated probe was tested in an acute rat, from which spiking activities were phase-locked to the optical stimuli. Because the μLED integrated probes were scaled significantly (in terms of confined illumination, increased number of light sources per shank, increased number of recording electrodes, and reduced weight of tethered cables), they were chronically implanted into mice for practical neuroscience studies. These μLEDs are the smallest implantable light sources ever reported for optogenetic applications. In the experiments, selective activations of individual cells that are only 50 μm apart were demonstrated, and that the activations of a particular cell via different input pathways were also demonstrated. These results clearly marked the record in spatial precision of optogenetic manipulation of neural circuits, which will bring new insights to brain mapping at the cellular or even sub-cellular level.

The detailed achievements and contributions of this thesis can be summarized as follows:

Flexible polymer probe:

- A novel silk coating method enabled implantable devices to be made out of any material (including polymer), size and geometry as the coating provides the mechanical stiffness to penetrate the brain.
- The probes were made from flexible parylene substrates to reduce shear stress caused by micro-motion. The probe tips were designed with unique geometries aimed to minimize tissue reactions near the recording electrodes. The probe structure could be optimally designed to enhance its recording reliability.
- Silk fibroin was patterned for the first time by soft-lithography, creating arbitrary shapes in uniform thickness with high precision.
- The 64-site, 8-shanked probes were successfully inserted into the layer-V motor cortex in rats without significant deviation from their intended track.
- The implanted probes recorded from 6 behaving rats for 6 weeks without signal quality degradation.

Optical stimulation probe (waveguide approach):

- The Michigan probe was monolithically integrated with optical waveguides for the first time for optogenetic applications.
- Different waveguide geometries such as optical mixer and optical splitter can be easily patterned with lithographic resolution for different light guiding configurations.
- The total transmission efficiency of 9% was achieved in the dielectric waveguide, which was improved from SU-8 waveguides by nearly an order of magnitude.

- A single-shanked probe (shank dimensions: 5-mm-long, 70-μm-wide, 15-μm-thick) with 1 waveguide and 8 recording electrodes could successfully induce the robust spiking corresponding to light stimuli in an acute CAG::ChR2 animal.

Optical stimulation probe (μLED approach):

- The Michigan probe was monolithically integrated with μLEDs directly on the probe shanks for the first time by utilizing recently developed GaN-on-Si technologies.
- The 4-shank, 32-recording-site, and 12-μLED probes were designed, fabricated and fully characterized (shank dimensions: 5-mm-long, 70-μm-wide, 30-μm-thick, 250-μm-pitch; recording site area: 143μm^2; μLED emission area: 150μm^2).
- The fabricated μLEDs performed close to their theoretical efficiency of 0.9% from the optimized fabrication processes and operating conditions.
- Thermal modeling in COMSOL showed that both DC and AC driving conditions of the μLEDs were possible to produce enough light (conservatively greater than 1mW/mm^2) to activate the ChR2 while keeping the ambient tissue heating by less than 1°C.
- The entire assembled package was fiberless and low-weight (~4g), allowing animals to move freely during behaving experiments.
- The minimum power to robustly activate ChR2 expressing neurons using the μLEDs was only 36nW, corresponding to 0.24mW/mm^2 light intensity.

- Low power stimulation has achieved sub-layer resolution, as demonstrated by the selective stimulation of two cells that are only 50 μm apart using adjacent μLEDs that are separated by 60 μm in pitch.
- It was demonstrated that a particular cell could be activated via different mechanisms, and can be either in-phase or anti-phase relative to the timing of the light input.
- It was shown for the first time that illumination of the CA1-orien layer (absent of PYR) could trigger distant PYR in the CA1-pyramidal layer to spike and oscillate via indirect circuit effect.
- Having 480 million possible stimulation sequences with 12 integrated μLEDs that can illuminate the neural network with sub-layer resolution, this technology can be the key to unlock many of the unknown mechanisms underlying signal transduction in the brain.

5.2. Suggested future work

In order to advance MEMS implantable probe technology for chronic applications in rodents and eventually towards primate research or human clinical use, the protocol to test the long-term biocompatibility should have implantation time of at least 6 months. Because the silk-coating technology developed in this work can support the insertion of probes of any structure, it is important to simplify the geometry of the probe shanks and study a single parameter (e.g., shank width or surface area) that could be quantitatively correlated to tissue reaction. In addition, it would be beneficial to test other materials for the probe shanks with a property that could minimize foreign body

response. The electrophysiology recording quality should be coupled with immunohistology data and compared with existing probe technologies.

To support the recent advance in optogenetics, two probe designs have been described in this thesis. The integrated waveguide optical probe offers flexibility in terms of light source selection. In the future, optical fibers should be substituted by LEDs or laser diodes to eliminate the bulky assembly. The coupling between these large light-emitting sources to a miniature waveguide should be very challenging. Once coupling is optimized, the waveguide approach can deliver light from multiple sources having different wavelength for activation and silencing of targeted neuronal population. The μLED probe can meet the "dream" specifications for stimulation of any densely-populated neural circuits, with high spatial resolution to selectively activate adjacent cells of the same type. A challenging future direction for this work is to develop methods to generate multi-wavelength emission from LEDs fabricated from the same wafer. Wireless control of the μLEDs is another feasible advance since power consumption is in the microwatt range. Lastly, the interference between the stimulation and recording channels should be further reduced. One possible solution could involve modifications of the fabrication process to add a shielding layer between the recording channels and the stimulation channels.

REFERENCES:

[1] F. A. C. Azevedo, L. R. B. Carvalho, L. T. Grinberg, J. M. Farfel, R. E. L. Ferretti, R. E. P. Leite, W. J. Filho, R. Lent, and S. Herculano-Houzel, "Equal numbers of neuronal and nonneuronal cells make the human brain an isometrically scaled-up primate brain," *J. Comp. Neurol.*, vol. 513, pp. 532–541, 2009.

[2] D. Krioukov, M. Kitsak, R. S. Sinkovits, D. Rideout, D. Meyer, and M. Boguñá, "Network cosmology.," *Sci. Rep.*, vol. 2, p. 793, 2012.

[3] R. S. J. Frackowiak, J. T. Ashburner, W. D. Penny, and S. Zeki, *Human Brain Function, Second Edition*. 2004, p. 1144.

[4] L. Lin, G. Chen, K. Xie, K. A. Zaia, S. Zhang, and J. Z. Tsien, "Large-scale neural ensemble recording in the brains of freely behaving mice," *J. Neurosci. Methods*, vol. 155, pp. 28–38, 2006.

[5] G. Buzsáki, "Large-scale recording of neuronal ensembles.," *Nat. Neurosci.*, vol. 7, pp. 446–451, 2004.

[6] R. Goebel, "Localization of brain activity using functional magnetic resonance imaging," in *Clinical Functional MRI*, 2007, pp. 9–51.

[7] T. Pradhan, H. S. Jung, J. H. Jang, T. W. Kim, C. Kang, and J. S. Kim, "Chemical sensing of neurotransmitters.," *Chem. Soc. Rev.*, vol. 43, pp. 4684–713, 2014.

[8] S. R. Sinha and P. Saggau, "Simultaneous optical recording of membrane potential and intracellular calcium from brain slices.," *Methods*, vol. 18, pp. 204–214, 175, 1999.

[9] A. Perron, W. Akemann, H. Mutoh, and T. Knöpfel, "Genetically encoded probes for optical imaging of brain electrical activity," *Prog. Brain Res.*, vol. 196, pp. 63–77, 2012.

[10] S. M. Montgomery, "Extracellular Electrophysiology," *Internet*, pp. 1–6, 2002.

[11] A. C. Hoogerwerf and K. D. Wise, "A three-dimensional neural recording array," *TRANSDUCERS '91 1991 Int. Conf. Solid-State Sensors Actuators. Dig. Tech. Pap.*, 1991.

[12] S. Kim, R. Bhandari, M. Klein, S. Negi, L. Rieth, P. Tathireddy, M. Toepper, H. Oppermann, and F. Solzbacher, “Integrated wireless neural interface based on the Utah electrode array,” *Biomed. Microdevices*, vol. 11, pp. 453–466, 2009.

[13] N. K. Logothetis, M. Augath, Y. Murayama, A. Rauch, F. Sultan, J. Goense, A. Oeltermann, and H. Merkle, “The effects of electrical microstimulation on cortical signal propagation.,” *Nat. Neurosci.*, vol. 13, pp. 1283–1291, 2010.

[14] D. Huber, L. Petreanu, N. Ghitani, S. Ranade, T. Hromádka, Z. Mainen, and K. Svoboda, “Sparse optical microstimulation in barrel cortex drives learned behaviour in freely moving mice.,” *Nature*, vol. 451, pp. 61–64, 2008.

[15] J. G. Bernstein and E. S. Boyden, “Optogenetic tools for analyzing the neural circuits of behavior,” *Trends in Cognitive Sciences*, vol. 15. pp. 592–600, 2011.

[16] S. Butovas and C. Schwarz, “Spatiotemporal effects of microstimulation in rat neocortex: a parametric study using multielectrode recordings.,” *J. Neurophysiol.*, vol. 90, pp. 3024–3039, 2003.

[17] O. Yizhar, L. E. Fenno, T. J. Davidson, M. Mogri, and K. Deisseroth, “Optogenetics in Neural Systems,” *Neuron*, vol. 71. pp. 9–34, 2011.

[18] L. Buchen, “Neuroscience: Illuminating the brain.,” *Nature*, vol. 465. pp. 26–28, 2010.

[19] E. S. Boyden, F. Zhang, E. Bamberg, G. Nagel, and K. Deisseroth, “Millisecond-timescale, genetically targeted optical control of neural activity.,” *Nat. Neurosci.*, vol. 8, pp. 1263–1268, 2005.

[20] T. Ishizuka, M. Kakuda, R. Araki, and H. Yawo, “Kinetic evaluation of photosensitivity in genetically engineered neurons expressing green algae light-gated channels,” *Neurosci. Res.*, vol. 54, pp. 85–94, 2006.

[21] X. Li, D. V Gutierrez, M. G. Hanson, J. Han, M. D. Mark, H. Chiel, P. Hegemann, L. T. Landmesser, and S. Herlitze, “Fast noninvasive activation and inhibition of neural and network activity by vertebrate rhodopsin and green algae channelrhodopsin.,” *Proc. Natl. Acad. Sci. U. S. A.*, vol. 102, pp. 17816–17821, 2005.

[22] G. Nagel, M. Brauner, J. F. Liewald, N. Adeishvili, E. Bamberg, and A. Gottschalk, “Light activation of Channelrhodopsin-2 in excitable cells of caenorhabditis elegans triggers rapid behavioral responses,” *Curr. Biol.*, vol. 15, pp. 2279–2284, 2005.

[23] F. Zhang, L.-P. Wang, M. Brauner, J. F. Liewald, K. Kay, N. Watzke, P. G. Wood, E. Bamberg, G. Nagel, A. Gottschalk, and K. Deisseroth, “Multimodal fast optical interrogation of neural circuitry.,” *Nature*, vol. 446, pp. 633–639, 2007.

[24] V. Gradinaru, F. Zhang, C. Ramakrishnan, J. Mattis, R. Prakash, I. Diester, I. Goshen, K. R. Thompson, and K. Deisseroth, “Molecular and Cellular Approaches for Diversifying and Extending Optogenetics,” *Cell*, vol. 141, pp. 154–165, 2010.

[25] B. Y. Chow, X. Han, A. S. Dobry, X. Qian, A. S. Chuong, M. Li, M. A. Henninger, G. M. Belfort, Y. Lin, P. E. Monahan, and E. S. Boyden, “High-performance genetically targetable optical neural silencing by light-driven proton pumps.,” *Nature*, vol. 463, pp. 98–102, 2010.

[26] X. Han, B. Y. Chow, H. Zhou, N. C. Klapoetke, A. Chuong, R. Rajimehr, A. Yang, M. V Baratta, J. Winkle, R. Desimone, and E. S. Boyden, “A high-light sensitivity optical neural silencer: development and application to optogenetic control of non-human primate cortex.,” *Front. Syst. Neurosci.*, vol. 5, p. 18, 2011.

[27] S. Royer, B. V Zemelman, A. Losonczy, J. Kim, F. Chance, J. C. Magee, and G. Buzsáki, “Control of timing, rate and bursts of hippocampal place cells by dendritic and somatic inhibition,” *Nature Neuroscience*, vol. 15. pp. 769–775, 2012.

[28] F. Zhang, M. Prigge, F. Beyrière, S. P. Tsunoda, J. Mattis, O. Yizhar, P. Hegemann, and K. Deisseroth, “Red-shifted optogenetic excitation: a tool for fast neural control derived from Volvox carteri.,” *Nat. Neurosci.*, vol. 11, pp. 631–633, 2008.

[29] V. S. Sohal, F. Zhang, O. Yizhar, and K. Deisseroth, “Parvalbumin neurons and gamma rhythms enhance cortical circuit performance.,” *Nature*, vol. 459, pp. 698–702, 2009.

[30] E. Stark, L. Roux, R. Eichler, Y. Senzai, S. Royer, and G. Buzsáki, “Pyramidal cell-interneuron interactions underlie hippocampal ripple oscillations,” *Neuron*, vol. 83, pp. 467–480, 2014.

[31] G. Buzsaki, L. W. S. Leung, and C. H. Vanderwolf, “Cellular bases of hippocampal EEG in the behaving rat,” *Brain Research Reviews*, vol. 6. pp. 139–171, 1983.

[32] R. D. Traub, D. Schmitz, N. Maier, M. A. Whittington, and A. Draguhn, “Axonal properties determine somatic firing in a model of in vitro CA1 hippocampal sharp wave/ripples and persistent gamma oscillations,” *Eur. J. Neurosci.*, vol. 36, pp. 2650–2660, 2012.

[33] J. Taxidis, S. Coombes, R. Mason, and M. R. Owen, “Modeling sharp wave-ripple complexes through a CA3-CA1 network model with chemical synapses,” *Hippocampus*, vol. 22, pp. 995–1017, 2012.

[34] N. Maier, V. Nimmrich, and A. Draguhn, “Cellular and network mechanisms underlying spontaneous sharp wave-ripple complexes in mouse hippocampal slices.,” *J. Physiol.*, vol. 550, pp. 873–887, 2003.

[35] R.-M. Memmesheimer, “Quantitative prediction of intermittent high-frequency oscillations in neural networks with supralinear dendritic interactions.,” *Proc. Natl. Acad. Sci. U. S. A.*, vol. 107, pp. 11092–11097, 2010.

[36] P. Olejniczak, “Neurophysiologic basis of EEG.,” *J. Clin. Neurophysiol.*, vol. 23, pp. 186–189, 2006.

[37] G. Buzsáki, C. A. Anastassiou, and C. Koch, “The origin of extracellular fields and currents — EEG, ECoG, LFP and spikes,” *Nature Reviews Neuroscience*, vol. 13. pp. 407–420, 2012.

[38] S. B. Kodandaramaiah, G. T. Franzesi, B. Y. Chow, E. S. Boyden, and C. R. Forest, “Automated whole-cell patch-clamp electrophysiology of neurons in vivo,” *Nature Methods*, vol. 9. pp. 585–587, 2012.

[39] F. Strumwasser, “Long-term recording’ from single neurons in brain of unrestrained mammals.,” *Science*, vol. 127, pp. 469–470, 1958.

[40] C. M. Gray, P. E. Maldonado, M. Wilson, and B. McNaughton, “Tetrodes markedly improve the reliability and yield of multiple single-unit isolation from multi-unit recordings in cat striate cortex,” *J. Neurosci. Methods*, vol. 63, pp. 43–54, 1995.

[41] K. D. Harris, D. A. Henze, J. Csicsvari, H. Hirase, and G. Buzsáki, “Accuracy of tetrode spike separation as determined by simultaneous intracellular and extracellular measurements.,” *J. Neurophysiol.*, vol. 84, pp. 401–414, 2000.

[42] T. J. Blanche, M. A. Spacek, J. F. Hetke, and N. V Swindale, “Polytrodes: high-density silicon electrode arrays for large-scale multiunit recording.,” *J. Neurophysiol.*, vol. 93, pp. 2987–3000, 2005.

[43] P. K. Campbell, K. E. Jones, R. J. Huber, K. W. Horch, and R. A. Normann, “A silicon-based, three-dimensional neural interface: Manufacturing processes for an intracortical electrode array,” *IEEE Trans. Biomed. Eng.*, vol. 38, pp. 758–768, 1991.

[44] R. R. Harrison, P. T. Watkins, R. J. Kier, R. O. Lovejoy, D. J. Black, B. Greger, and F. Solzbacher, “A low-power integrated circuit for a wireless 100-electrode

neural recording system," *IEEE J. Solid-State Circuits*, vol. 42, pp. 123–133, 2007.

[45] L. R. Hochberg, M. D. Serruya, G. M. Friehs, J. A. Mukand, M. Saleh, A. H. Caplan, A. Branner, D. Chen, R. D. Penn, and J. P. Donoghue, "Neuronal ensemble control of prosthetic devices by a human with tetraplegia.," *Nature*, vol. 442, pp. 164–171, 2006.

[46] K. D. Wise, J. B. Angell, and A. Starr, "An integrated-circuit approach to extracellular microelectrodes.," *IEEE Trans. Biomed. Eng.*, vol. 17, pp. 238–247, 1970.

[47] Y. Yao, M. N. Gulari, J. A. Wiler, and K. D. Wise, "A microassembled low-profile three-dimensional microelectrode array for neural prosthesis applications," *J. Microelectromechanical Syst.*, vol. 16, pp. 977–988, 2007.

[48] K. D. Wise, A. M. Sodagar, Y. Yao, M. N. Gulari, G. E. Perlin, and K. Najafi, "Microelectrodes, microelectronics, and implantable neural microsystems," *Proc. IEEE*, vol. 96, pp. 1184–1202, 2008.

[49] C. Kim and K. D. Wise, "A 64-site multishank CMOS low-profile neural stimulating probe," *IEEE J. Solid-State Circuits*, vol. 31, pp. 1230–1238, 1996.

[50] K. D. Wise, D. J. Anderson, J. F. Hetke, D. R. Kipke, and K. Najafi, "Wireless implantable microsystems: High-density electronic interfaces to the nervous system," in *Proceedings of the IEEE*, 2004, vol. 92, pp. 76–97.

[51] I. H. Stevenson and K. P. Kording, "How advances in neural recording affect data analysis.," *Nat. Neurosci.*, vol. 14, pp. 139–142, 2011.

[52] J. Du, T. J. Blanche, R. R. Harrison, H. A. Lester, and S. C. Masmanidis, "Multiplexed, high density electrophysiology with nanofabricated neural probes," *PLoS One*, vol. 6, 2011.

[53] P. Ruther, S. Herwik, S. Kisban, K. Seidl, and O. Paul, "Recent progress in neural probes using silicon MEMS technology," *IEEJ Trans. Electr. Electron. Eng.*, vol. 5, pp. 505–515, 2010.

[54] M. E. Merriam, S. Dehmel, O. Srivannavit, S. E. Shore, and K. D. Wise, "A 3-D 160-site microelectrode array for cochlear nucleus mapping," *IEEE Trans. Biomed. Eng.*, vol. 58, pp. 397–403, 2011.

[55] P. Moshayedi, G. Ng, J. C. F. Kwok, G. S. H. Yeo, C. E. Bryant, J. W. Fawcett, K. Franze, and J. Guck, "The relationship between glial cell mechanosensitivity and foreign body reactions in the central nervous system," *Biomaterials*, vol. 35, pp. 3919–3925, 2014.

[56] P. Thevenot, W. Hu, and L. Tang, “Surface chemistry influences implant biocompatibility.,” *Curr. Top. Med. Chem.*, vol. 8, pp. 270–280, 2008.

[57] J. P. Seymour and D. R. Kipke, “Neural probe design for reduced tissue encapsulation in CNS,” *Biomaterials*, vol. 28, pp. 3594–3607, 2007.

[58] G. E. Perlin, “A Fully-Implantable Integrated Front-End for Neural Recording Microsystems,” 2008.

[59] E. Merriam, “A Three-dimensional bidirectional interface for neural mapping studies,” 2010.

[60] J. P. Seymour, “Advanced polymer-based microfabricated neural probes using biologically driven designs by,” 2009.

[61] J. P. Donoghue, “Bridging the Brain to the World: A Perspective on Neural Interface Systems,” *Neuron*, vol. 60. pp. 511–521, 2008.

[62] M. A. L. Nicolelis, “Brain-machine interfaces to restore motor function and probe neural circuits.,” *Nat. Rev. Neurosci.*, vol. 4, pp. 417–422, 2003.

[63] J. C. Williams, R. L. Rennaker, and D. R. Kipke, “Long-term neural recording characteristics of wire microelectrode arrays implanted in cerebral cortex,” *Brain Res. Protoc.*, vol. 4, pp. 303–313, 1999.

[64] S. Myllymaa, K. Myllymaa, H. Korhonen, J. Töyräs, J. E. Jääskeläinen, K. Djupsund, H. Tanila, and R. Lappalainen, “Fabrication and testing of polyimide-based microelectrode arrays for cortical mapping of evoked potentials,” *Biosens. Bioelectron.*, vol. 24, pp. 3067–3072, 2009.

[65] H.-Y. Lai, L.-D. Liao, C.-T. Lin, J.-H. Hsu, X. He, Y.-Y. Chen, J.-Y. Chang, H.-F. Chen, S. Tsang, and Y.-Y. I. Shih, “Design, simulation and experimental validation of a novel flexible neural probe for deep brain stimulation and multichannel recording,” *Journal of Neural Engineering*, vol. 9. p. 036001, 2012.

[66] V. S. Polikov, P. A. Tresco, and W. M. Reichert, “Response of brain tissue to chronically implanted neural electrodes,” *Journal of Neuroscience Methods*, vol. 148. pp. 1–18, 2005.

[67] A. J. Sawyer and T. R. Kyriakides, “Nanoparticle-based evaluation of blood-brain barrier leakage during the foreign body response.,” *J. Neural Eng.*, vol. 10, p. 016013, 2013.

[68] K. A. Potter, A. C. Buck, W. K. Self, and J. R. Capadona, “Stab injury and device implantation within the brain results in inversely multiphasic neuroinflammatory

and neurodegenerative responses," *Journal of Neural Engineering*, vol. 9. p. 046020, 2012.

[69] Y. T. Kim, R. W. Hitchcock, M. J. Bridge, and P. A. Tresco, "Chronic response of adult rat brain tissue to implants anchored to the skull," *Biomaterials*, vol. 25, pp. 2229–2237, 2004.

[70] K. C. Cheung, P. Renaud, H. Tanila, and K. Djupsund, "Flexible polyimide microelectrode array for in vivo recordings and current source density analysis," *Biosens. Bioelectron.*, vol. 22, pp. 1783–1790, 2007.

[71] T. D. Y. Kozai, N. B. Langhals, P. R. Patel, X. Deng, H. Zhang, K. L. Smith, J. Lahann, N. a Kotov, and D. R. Kipke, "Ultrasmall implantable composite microelectrodes with bioactive surfaces for chronic neural interfaces.," *Nat. Mater.*, vol. 11, pp. 1065–73, 2012.

[72] K. Najafi, J. Ji, and K. D. Wise, "Scaling limitations of silicon multichannel recording probes," *IEEE Trans. Biomed. Eng.*, vol. 37, pp. 1–11, 1990.

[73] K.-K. Lee, J. He, A. Singh, S. Massia, G. Ehteshami, B. Kim, and G. Raupp, "Polyimide-based intracortical neural implant with improved structural stiffness," *Journal of Micromechanics and Microengineering*, vol. 14. pp. 32–37, 2003.

[74] D. Egert, R. L. Peterson, and K. Najafi, "Parylene microprobes with engineered stiffness and shape for improved insertion," in *2011 16th International Solid-State Sensors, Actuators and Microsystems Conference, TRANSDUCERS'11*, 2011, pp. 198–201.

[75] S. H. Felix, K. G. Shah, V. M. Tolosa, H. J. Sheth, A. C. Tooker, T. L. Delima, S. P. Jadhav, L. M. Frank, and S. S. Pannu, "Insertion of flexible neural probes using rigid stiffeners attached with biodissolvable adhesive.," *J. Vis. Exp.*, p. e50609, 2013.

[76] F. Wu, M. Im, and E. Yoon, "A flexible fish-bone-shaped neural probe strengthened by biodegradable silk coating for enhanced biocompatibility," in *2011 16th International Solid-State Sensors, Actuators and Microsystems Conference, TRANSDUCERS'11*, 2011, pp. 966–969.

[77] H. J. Jin, J. Park, V. Karageorgiou, U. J. Kim, R. Valluzzi, P. Cebe, and D. L. Kaplan, "Water-stable silk films with reduced beta-sheet content," *Adv. Funct. Mater.*, vol. 15, pp. 1241–1247, 2005.

[78] T. Arai, G. Freddi, R. Innocenti, and M. Tsukada, "Biodegradation of bombyx mori silk fibroin fibers and films," *J. Appl. Polym. Sci.*, vol. 91, pp. 2383–2390, 2004.

[79] X. M. Chen, Y. M. Yang, J. Wu, Y. H. Zhao, F. Ding, and X. S. Gu, "Biocompatibility studies of silk fibroin-based artificial nerve grafts in vitro and in vivo," *Prog. Nat. Sci.*, vol. 17, pp. 1029–1034, 2007.

[80] L. W. Tien, F. Wu, M. D. Tang-Schomer, E. Yoon, F. G. Omenetto, and D. L. Kaplan, "Silk as a multifunctional biomaterial substrate for reduced glial scarring around brain-penetrating electrodes," *Adv. Funct. Mater.*, vol. 23, pp. 3185–3193, 2013.

[81] M. Im, I.-J. Cho, K.-S. Yun, and E. Yoon, "An electromagnetically-actuated polymer micro-pen for picoliter biological assay patterning," *13th Int. Conf. Solid-State Sensors, Actuators Microsystems, 2005. Dig. Tech. Pap. TRANSDUCERS '05.*, vol. 2, 2005.

[82] S. M. Ramkumar, H. Venugopalan, and K. Khanna, "Novel anisotropic conductive adhesive for 3D stacking and lead-free PCB packaging - A review," in *Proceedings - Electronic Components and Technology Conference*, 2011, pp. 246–254.

[83] J. N. Turner, W. Shain, D. H. Szarowski, M. Andersen, S. Martins, M. Isaacson, and H. Craighead, "Cerebral astrocyte response to micromachined silicon implants.," *Exp. Neurol.*, vol. 156, pp. 33–49, 1999.

[84] R. D. Airan, K. R. Thompson, L. E. Fenno, H. Bernstein, and K. Deisseroth, "Temporally precise in vivo control of intracellular signaling.," *Nature*, vol. 458, pp. 1025–1029, 2009.

[85] P. Anikeeva, A. S. Andalman, I. Witten, M. Warden, I. Goshen, L. Grosenick, L. A. Gunaydin, L. M. Frank, and K. Deisseroth, "Optetrode: a multichannel readout for optogenetic control in freely moving mice," *Nature Neuroscience*, vol. 15. pp. 163–170, 2011.

[86] J. A. Cardin, M. Carlén, K. Meletis, U. Knoblich, F. Zhang, K. Deisseroth, L.-H. Tsai, and C. I. Moore, "Targeted optogenetic stimulation and recording of neurons in vivo using cell-type-specific expression of Channelrhodopsin-2.," *Nat. Protoc.*, vol. 5, pp. 247–254, 2010.

[87] D. F. English, O. Ibanez-Sandoval, E. Stark, F. Tecuapetla, G. Buzsáki, K. Deisseroth, J. M. Tepper, and T. Koos, "GABAergic circuits mediate the reinforcement-related signals of striatal cholinergic interneurons," *Nature Neuroscience*, vol. 15. pp. 123–130, 2011.

[88] M. M. Halassa, J. H. Siegle, J. T. Ritt, J. T. Ting, G. Feng, and C. I. Moore, "Selective optical drive of thalamic reticular nucleus generates thalamic bursts and cortical spindles.," *Nat. Neurosci.*, vol. 14, pp. 1118–1120, 2011.

[89] X. Han, X. Qian, J. G. Bernstein, H.-H. Zhou, G. T. Franzesi, P. Stern, R. T. Bronson, A. M. Graybiel, R. Desimone, and E. S. Boyden, “Millisecond-timescale optical control of neural dynamics in the nonhuman primate brain.,” *Neuron*, vol. 62, pp. 191–198, 2009.

[90] A. V. Kravitz, B. S. Freeze, P. R. L. Parker, K. Kay, M. T. Thwin, K. Deisseroth, and A. C. Kreitzer, “Regulation of parkinsonian motor behaviours by opt... [Nature. 2010] - PubMed result,” *Nature*, vol. 466, pp. 622–6, 2010.

[91] S. Royer, B. V. Zemelman, M. Barbic, A. Losonczy, G. Buzsáki, and J. C. Magee, “Multi-array silicon probes with integrated optical fibers: Light-assisted perturbation and recording of local neural circuits in the behaving animal,” *Eur. J. Neurosci.*, vol. 31, pp. 2279–2291, 2010.

[92] E. Stark, T. Koos, and G. Buzsaki, “Diode probes for spatiotemporal optical control of multiple neurons in freely moving animals,” *Journal of Neurophysiology*, vol. 108. pp. 349–363, 2012.

[93] A. N. Zorzos, E. S. Boyden, and C. G. Fonstad, “Multiwaveguide implantable probe for light delivery to sets of distributed brain targets.,” *Opt. Lett.*, vol. 35, pp. 4133–4135, 2010.

[94] B. Rubehn, S. B. E. Wolff, P. Tovote, M. Schuettler, A. Luthi, and T. Stieglitz, “Polymer-based shaft microelectrodes with optical and fluidic capabilities as a tool for optogenetics,” in *Proceedings of the Annual International Conference of the IEEE Engineering in Medicine and Biology Society, EMBS*, 2011, pp. 2969–2972.

[95] M. Schwaerzle, K. Seidl, U. T. Schwarz, O. Paul, and P. Ruther, “Ultracompact optrode with integrated laser diode chips and SU-8 waveguides for optogenetic applications,” in *Proceedings of the IEEE International Conference on Micro Electro Mechanical Systems (MEMS)*, 2013, pp. 1029–1032.

[96] M. Im, I. J. Cho, F. Wu, K. D. Wise, and E. Yoon, “Neural probes integrated with optical mixer/splitter waveguides and multiple stimulation sites,” in *Proceedings of the IEEE International Conference on Micro Electro Mechanical Systems (MEMS)*, 2011, pp. 1051–1054.

[97] M. Im, I. J. Cho, F. Wu, K. D. Wise, and E. Yoon, “A dual-shank neural probe integrated with double waveguides on each shank for optogenetic applications,” in *Proceedings of the Annual International Conference of the IEEE Engineering in Medicine and Biology Society, EMBS*, 2011, pp. 5480–5483.

[98] C. Liu, Y. Liu, M. Sokuler, D. Fell, S. Keller, A. Boisen, H.-J. Butt, G. K. Auernhammer, and E. Bonaccurso, “Diffusion of water into SU-8 microcantilevers.,” *Phys. Chem. Chem. Phys.*, vol. 12, pp. 10577–10583, 2010.

[99] A. M. Aravanis, L.-P. Wang, F. Zhang, L. A. Meltzer, M. Z. Mogri, M. B. Schneider, and K. Deisseroth, “An optical neural interface: in vivo control of rodent motor cortex with integrated fiberoptic and optogenetic technology.,” *J. Neural Eng.*, vol. 4, pp. S143–S156, 2007.

[100] J. Csicsvari, D. A. Henze, B. Jamieson, K. D. Harris, A. Sirota, P. Barthó, K. D. Wise, and G. Buzsáki, “Massively parallel recording of unit and local field potentials with silicon-based electrodes.,” *J. Neurophysiol.*, vol. 90, pp. 1314–1323, 2003.

[101] M. Kindlundh, P. Norlin, and U. G. Hofmann, “A neural probe process enabling variable electrode configurations,” *Sensors Actuators, B Chem.*, vol. 102, pp. 51–58, 2004.

[102] I. J. Cho, H. W. Baac, and E. Yoon, “A 16-site neural probe integrated with a waveguide for optical stimulation,” in *Proceedings of the IEEE International Conference on Micro Electro Mechanical Systems (MEMS)*, 2010, pp. 995–998.

[103] L. Eldada and L. W. Shacklette, “Advances in polymer integrated optics,” *IEEE J. Sel. Top. Quantum Electron.*, vol. 6, pp. 54–68, 2000.

[104] F. Wu, E. Stark, M. Im, I.-J. Cho, E.-S. Yoon, G. Buzsáki, K. D. Wise, and E. Yoon, “An implantable neural probe with monolithically integrated dielectric waveguide and recording electrodes for optogenetics applications.,” *J. Neural Eng.*, vol. 10, p. 056012, 2013.

[105] A. Wilm, “Requirements on LEDs in etendue limited light engines,” *Proc. SPIE, Photonics Multimed. II*, vol. 7001, p. 70010F–70010F–10, 2008.

[106] T.-I. T. Kim, J. G. McCall, Y. H. Jung, X. Huang, E. R. Siuda, Y. Li, J. Song, Y. M. Song, H. A. Pao, R.-H. R.-H. Kim, C. Lu, S. D. Lee, I.-S. Song, G. Shin, R. Al-Hasani, S. Kim, M. P. Tan, Y. Huang, F. G. Omenetto, J. a. Rogers, and M. R. Bruchas, “Injectable, Cellular-Scale Optoelectronics with Applications for Wireless Optogenetics,” *Science*, vol. 340, no. 6129, pp. 211–216, Apr. 2013.

[107] J. G. McCall, T. Kim, G. Shin, X. Huang, Y. H. Jung, R. Al-Hasani, F. G. Omenetto, M. R. Bruchas, and J. a Rogers, “Fabrication and application of flexible, multimodal light-emitting devices for wireless optogenetics.,” *Nat. Protoc.*, vol. 8, no. 12, pp. 2413–28, Dec. 2013.

[108] H. Yasuda, Q. S. Yu, and M. Chen, “Interfacial factors in corrosion protection: An EIS study of model systems,” *Prog. Org. Coatings*, vol. 41, pp. 273–279, 2001.

[109] M. S. Weaver, L. A. Michalski, K. Rajan, M. A. Rothman, J. A. Silvernail, J. J. Brown, P. E. Burrows, G. L. Graff, M. E. Gross, P. M. Martin, M. Hall, E. Mast,

C. Bonham, W. Bennett, and M. Zumhoff, “Organic light-emitting devices with extended operating lifetimes on plastic substrates,” *Appl. Phys. Lett.*, vol. 81, pp. 2929–2931, 2002.

[110] J. S. Lewis and M. S. Weaver, “Thin-film permeation-barrier technology for flexible organic light-emitting devices,” *IEEE J. Sel. Top. Quantum Electron.*, vol. 10, pp. 45–57, 2004.

[111] H. Chatham, “Oxygen diffusion barrier properties of transparent oxide coatings on polymeric substrates,” *Surf. Coatings Technol.*, vol. 78, pp. 1–9, 1996.

[112] N. Mcalinden, D. Massoubre, E. Richardson, E. Gu, and S. Sakata, “Thermal and Optical Characterization of MicroLED Probes for in vivo Optogenetic Neural Stimulation,” *Opt. Lett.*, vol. 38, pp. 992–994, 2013.

[113] G. Neves, S. F. Cooke, and T. V. P. Bliss, “Synaptic plasticity, memory and the hippocampus: a neural network approach to causality.,” *Nat. Rev. Neurosci.*, vol. 9, pp. 65–75, 2008.

[114] T. V Bliss and G. L. Collingridge, “A synaptic model of memory: long-term potentiation in the hippocampus.,” *Nature*, vol. 361, pp. 31–39, 1993.

[115] A. J. Shields, E. Limited, and C. S. Park, “Semiconductor quantum light sources,” *Nat. Photonics*, vol. 1, pp. 215–223, 2007.

[116] J. Robertson, *Comprehensive Semiconductor Science and Technology*. 2011, pp. 132–176.

[117] S. Nakamura, M. Senoh, N. Iwasa, and S. ichi Nagahama, “High-brightness in InGaN blue, green and yellow light-emitting diodes with quantum well structures,” *Japanese J. Appl. Physics, Part 2 Lett.*, vol. 34, 1995.

[118] D. M. Graham, P. Dawson, G. R. Chabrol, N. P. Hylton, D. Zhu, M. J. Kappers, C. McAleese, and C. J. Humphreys, “High photoluminescence quantum efficiency InGaN multiple quantum well structures emitting at 380 nm,” *J. Appl. Phys.*, vol. 101, 2007.

[119] E. J. Thrush, M. J. Kappers, P. Dawson, D. Graham, J. S. Barnard, M. E. Vickers, L. Considine, J. T. Mullins, and C. J. Humphreys, “GaN-InGaN quantum well and LED structures grown in a close coupled showerhead (CCS) MOCVD reactor,” in *Physica Status Solidi (A) Applied Research*, 2002, vol. 192, pp. 354–359.

[120] K.-M. Song and J. Park, “Effects of the growth pressure of a -plane InGaN/GaN multi-quantum wells on the optical performance of light-emitting diodes,” *Semicond. Sci. Technol.*, vol. 28, no. 1, p. 015010, Jan. 2013.

[121] G. Y. Zhang, Z. J. Yang, Y. Z. Tong, Z. X. Qin, X. D. Hu, Z. Z. Chen, X. M. Ding, M. Lu, Z. H. Li, T. J. Yu, L. Zhang, Z. Z. Gan, Y. Zhao, and C. F. Yang, "InGaN/GaN MQW high brightness LED grown by MOCVD," in *Optical Materials*, 2003, vol. 23, pp. 183–186.

[122] M. A. Khan, J. W. Yang, G. Simin, R. Gaska, M. S. Shur, H.-C. zur Loye, G. Tamulaitis, a. Zukauskas, D. J. Smith, D. Chandrasekhar, and R. Bicknell-Tassius, "Lattice and energy band engineering in AlInGaN/GaN heterostructures," *Appl. Phys. Lett.*, vol. 76, p. 1161, 2000.

[123] A. T. Cheng, Y. K. Su, and W. C. Lai, "Improved light output of nitride-based light-emitting diodes by lattice-matched AlInN cladding structure," *IEEE Photonics Technol. Lett.*, vol. 20, pp. 970–972, 2008.

[124] V. Avrutin, D. J. Silversmith, Y. Mori, F. Kawamura, Y. Kitaoka, and H. Morkoc, "Growth of Bulk GaN and AlN: Progress and Challenges," *Proc. IEEE*, vol. 98, pp. 1302–1315, 2010.

[125] J. H. Lee, D. Y. Lee, B. W. Oh, and J. H. Lee, "Comparison of InGaN-based LEDs grown on conventional sapphire and cone-shape-patterned sapphire substrate," *IEEE Trans. Electron Devices*, vol. 57, pp. 157–163, 2010.

[126] D. Zhu, C. McAleese, K. K. McLaughlin, M. Häberlen, C. O. Salcianu, E. J. Thrush, M. J. Kappers, W. A. Phillips, P. Lane, D. J. Wallis, T. Martin, M. Astles, S. Thomas, A. Pakes, M. Heuken, and C. J. Humphreys, "GaN-based LEDs grown on 6-inch diameter Si (111) substrates by MOVPE," *Proc. SPIE*, vol. 7231. pp. 723111–723118, 2009.

[127] M. Häberlen, D. Zhu, C. McAleese, T. Zhu, M. J. Kappers, and C. J. Humphreys, "Dislocation reduction in GaN grown on Si(111) using a strain-driven 3D GaN interlayer," *Phys. Status Solidi Basic Res.*, vol. 247, pp. 1753–1756, 2010.

[128] X. L. Fang, Y. Q. Wang, H. Meidia, and S. Mahajan, "Reduction of threading dislocations in GaN layers using in situ deposited silicon nitride masks on AlN and GaN nucleation layers," *Appl. Phys. Lett.*, vol. 84, pp. 484–486, 2004.

[129] A. Dadgar, F. Schulze, M. Wienecke, A. Gadanecz, J. Bläsing, P. Veit, T. Hempel, A. Diez, J. Christen, and A. Krost, "Epitaxy of GaN on silicon—impact of symmetry and surface reconstruction," *New Journal of Physics*, vol. 9. pp. 389–389, 2007.

[130] A. Krost and A. Dadgar, "GaN-based optoelectronics on silicon substrates," in *Materials Science and Engineering B: Solid-State Materials for Advanced Technology*, 2002, vol. 93, pp. 77–84.

[131] P. Norlin, M. Kindlundh, A. Mouroux, K. Yoshida, and U. G. Hofmann, “A 32-site neural recording probe fabricated by DRIE of SOI substrates,” *Journal of Micromechanics and Microengineering*, vol. 12. pp. 414–419, 2002.

[132] C. Mion, Y. C. Chang, J. F. Muth, P. Rajagopal, and J. D. Brown, “Thermal conductivity of GaN grown on silicon substrates,” *Gan Relat. Alloy. - 2003*, vol. 798, pp. 381–386, 2003.

[133] J. O. Song, J.-S. Ha, and T.-Y. Seong, “Ohmic-Contact Technology for GaN-Based Light-Emitting Diodes: Role of P-Type Contact,” *IEEE Trans. Electron Devices*, vol. 57, no. 1, pp. 42–59, Jan. 2010.

[134] X. Xie, L. Rieth, L. Williams, S. Negi, R. Bhandari, R. Caldwell, R. Sharma, P. Tathireddy, and F. Solzbacher, “Long-term reliability of Al2O3 and Parylene C bilayer encapsulated Utah electrode array based neural interfaces for chronic implantation.,” *J. Neural Eng.*, vol. 11, p. 026016, 2014.

[135] I. H. Lee, Y. S. Choi, K. K. Youn, S. J. Yu, J. K. Rhee, and S. G. Kim, “Reactive ion etching of GaN using Cl/sub 2//BCl/sub 3,” *Compd. Semicond. 1998. Proc. Twenty-Fifth Int. Symp. Compd. Semicond. Semicond. 1998. Proc. Twenty-Fifth Int. Symp. Compd. Semicond.*, pp. 769–74|xxvi+892, 1999.

[136] D. Zhu, C. McAleese, M. Häberlen, C. Salcianu, T. Thrush, M. Kappers, A. Phillips, P. Lane, M. Kane, D. Wallis, T. Martin, M. Astles, N. Hylton, P. Dawson, and C. Humphreys, “Efficiency measurement of GaN-based quantum well and light-emitting diode structures grown on silicon substrates,” *J. Appl. Phys.*, vol. 109, no. 1, p. 014502, 2011.

[137] T. Fujii, Y. Gao, R. Sharma, E. L. Hu, S. P. DenBaars, and S. Nakamura, “Increase in the extraction efficiency of GaN-based light-emitting diodes via surface roughening,” *Appl. Phys. Lett.*, vol. 84, pp. 855–857, 2004.

[138] T. H. Kim, J. H. Boo, M. H. Joo, J. W. Lee, K. H. Park, J. S. Ha, J. H. Jang, J. S. Lee, and H. J. Shin, “Investigation of the p-GaN Ohmic Contact Property by Using a Synchrotron Radiation Analysis,” *J. Korean Phys. Soc.*, vol. 50, no. 6, p. 1894, Jun. 2007.

[139] G. Verzellesi, D. Saguatti, M. Meneghini, F. Bertazzi, M. Goano, G. Meneghesso, and E. Zanoni, “Efficiency droop in InGaN/GaN blue light-emitting diodes: Physical mechanisms and remedies,” *J. Appl. Phys.*, vol. 114, no. 7, p. 071101, 2013.

[140] P. Andersen and E. I. Moser, “Brain temperature and hippocampal function.,” *Hippocampus*, vol. 5, pp. 491–8, 1995.

[141] M. M. Elwassif, Q. Kong, M. Vazquez, and M. Bikson, “Bio-heat transfer model of deep brain stimulation-induced temperature changes.,” *J. Neural Eng.*, vol. 3, no. 4, pp. 306–15, Dec. 2006.

[142] E. Stark, R. Eichler, L. Roux, S. Fujisawa, H. G. Rotstein, and G. Buzsáki, “Inhibition-Induced theta resonance in cortical circuits,” *Neuron*, vol. 80, pp. 1263–1276, 2013.

[143] N. Spruston, “Pyramidal neurons: dendritic structure and synaptic integration.,” *Nat. Rev. Neurosci.*, vol. 9, pp. 206–221, 2008.

[144] N. Burgess and J. O'Keefe, “Models of place and grid cell firing and theta rhythmicity,” *Current Opinion in Neurobiology*, vol. 21. pp. 734–744, 2011.

[145] G. Dragoi and S. Tonegawa, “Preplay of future place cell sequences by hippocampal cellular assemblies.,” *Nature*, vol. 469, pp. 397–401, 2011.

[146] F. Pisanello, L. Sileo, I. a Oldenburg, M. Pisanello, L. Martiradonna, J. a Assad, B. L. Sabatini, and M. De Vittorio, “Multipoint-emitting optical fibers for spatially addressable in vivo optogenetics.,” *Neuron*, vol. 82, no. 6, pp. 1245–54, Jun. 2014.

[147] Z. Gong, S. Jin, Y. Chen, J. McKendry, D. Massoubre, I. M. Watson, E. Gu, and M. D. Dawson, “Size-dependent light output, spectral shift, and self-heating of 400 nm InGaN light-emitting diodes,” *J. Appl. Phys.*, vol. 107, 2010.

[148] Y. R. Wu, C. Chiu, C. Y. Chang, P. Yu, and H. C. Kuo, “Size-dependent strain relaxation and optical characteristics of InGaN/GaN nanorod LEDs,” *IEEE J. Sel. Top. Quantum Electron.*, vol. 15, pp. 1226–1233, 2009.